

ESD ACCESSION LIST

DRI Call No. 84802

Copy No. 1 of 2 cys.

4

Solid State Research

1975

Prepared for the Department of the Air Force
under Electronic Systems Division Contract F19628-76-C-0002 by

Lincoln Laboratory

MASSACHUSETTS INSTITUTE OF TECHNOLOGY

LEXINGTON, MASSACHUSETTS



Approved for public release; distribution unlimited.

ADA025489

FILE COPY

The work reported in this document was performed at Lincoln Laboratory, a center for research operated by Massachusetts Institute of Technology, with the support of the Department of the Air Force under Contract F19628-76-C-0002.

This report may be reproduced to satisfy needs of U.S. Government agencies.

This technical report has been reviewed and is approved for publication.

FOR THE COMMANDER



Eugene C. Raabe, Lt. Col., USAF
Chief, ESD Lincoln Laboratory Project Office

Non-Lincoln Recipients

PLEASE DO NOT RETURN

Permission is given to destroy this document
when it is no longer needed.

MASSACHUSETTS INSTITUTE OF TECHNOLOGY
LINCOLN LABORATORY

SOLID STATE RESEARCH

QUARTERLY TECHNICAL SUMMARY REPORT
TO THE
AIR FORCE SYSTEMS COMMAND

1 AUGUST - 31 OCTOBER 1975

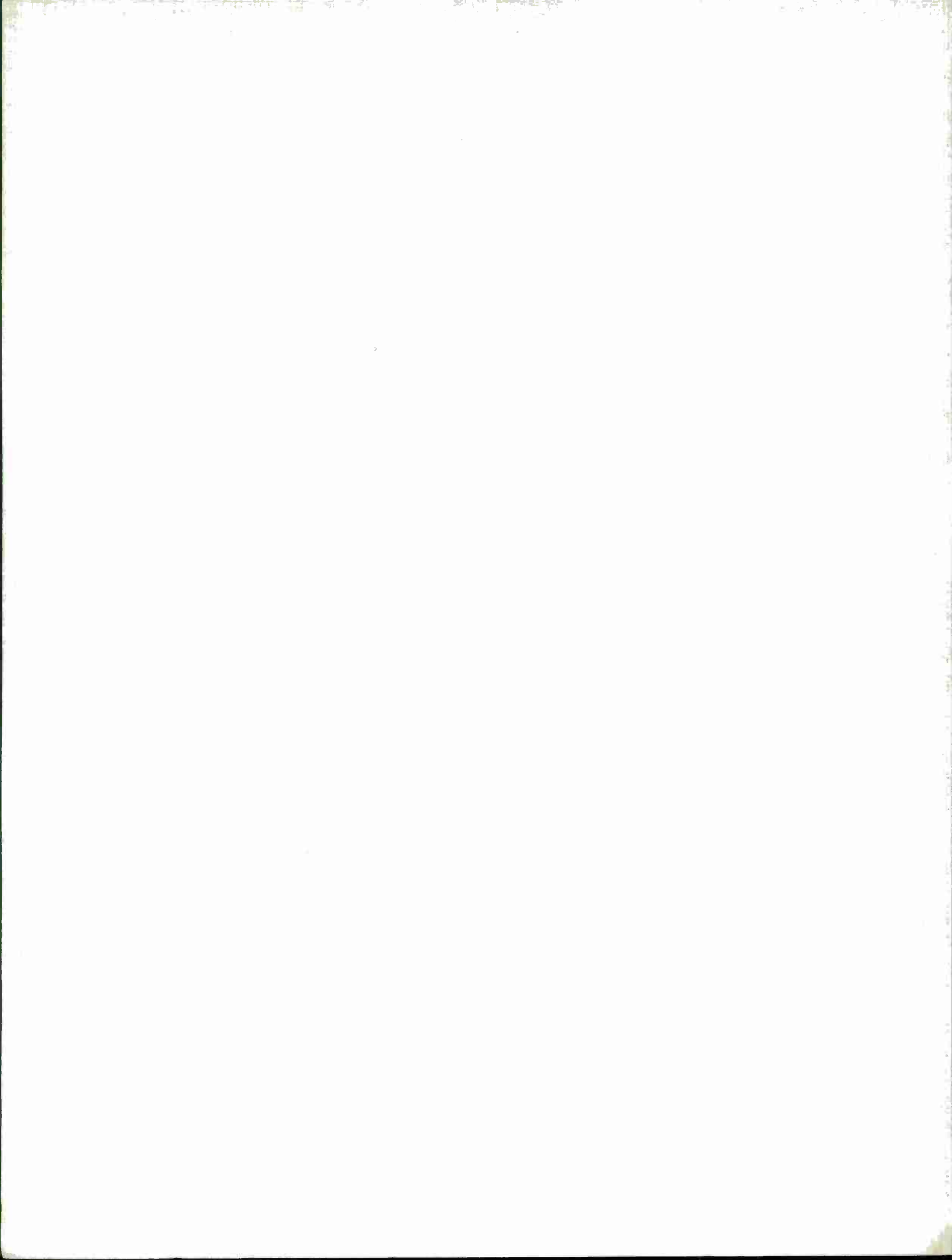
ISSUED 2 MARCH 1976

Approved for public release; distribution unlimited.

LEXINGTON

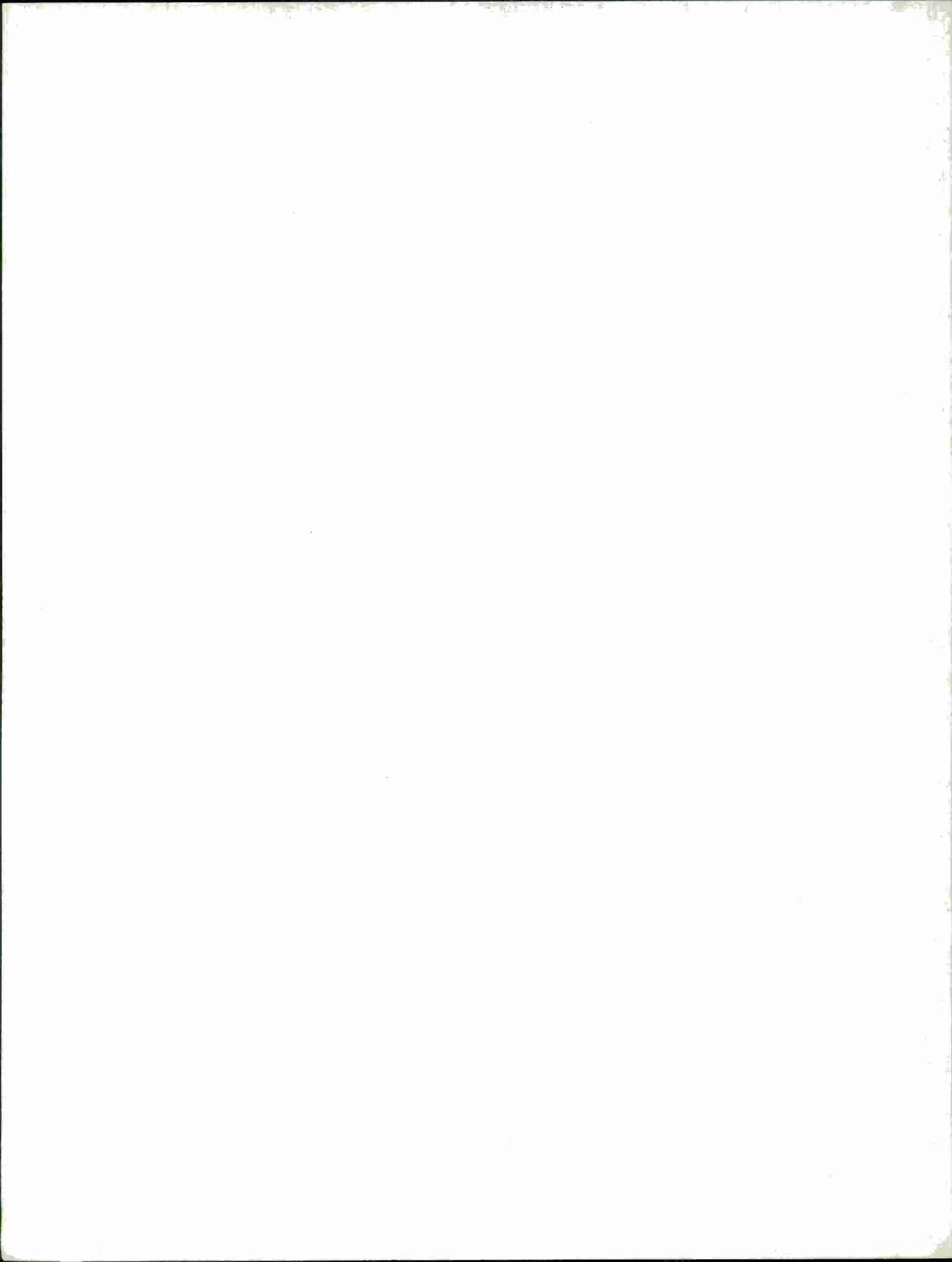
MASSACHUSETTS

AIR FORCE (1) MARCH 19, 1976--570



ABSTRACT

This report covers in detail the solid state research work of the Solid State Division at Lincoln Laboratory for the period 1 August through 31 October 1975. The topics covered are Solid State Device Research, Quantum Electronics, Materials Research, Microelectronics, and Surface-Wave Technology. Funding is primarily provided by the Air Force, with additional support provided by the Army (BMDATC), ARPA (MSO, IPTO), NSF, and ERDA.



CONTENTS

Abstract	iii
Introduction	vi
Reports on Solid State Research	x
Organization	xiv
I. SOLID STATE DEVICE RESEARCH	1
A. Low-Loss GaAs $p^+n^-n^+$ Optical Striplines Fabricated Using Be^+ -Ion Implantation	1
B. Electrical Properties of Tin Ion-Implanted GaAs	3
C. Molecular-Beam Epitaxial $Pb_{1-x}Sn_x$ Te Double-Heterostructure Lasers with CW Operation at 77 K	4
D. Preparation of Low Carrier Concentration PbS Crystals	6
II. QUANTUM ELECTRONICS	11
A. CW Laser Action in Acentric $NdAl_3(BO_3)_4$ and $KNdP_4O_{12}$	11
B. Photoluminescence of Bound Excitons in Tellurium-Doped Cadmium Sulfide	17
C. CW Second-Harmonic Generation in $CdGeAs_2$	18
D. Third-Harmonic Generation in Molecular Gases	19
E. Energy Relaxation Rates in Liquid Nitrogen	22
F. High-Resolution Submillimeter-Wave Spectroscopy Using Non-collinear, Difference-Frequency Mixing of CO_2 Laser Radiation	24
III. MATERIALS RESEARCH	29
A. Double-Heterostructure GaInAsP/InP Diode Lasers	29
B. Photoelectrolysis of Water	32
C. Stark-Split Excitonic Surface States on MgO	35
D. Thin-Film Conducting Microgrids as Transparent Heat Mirrors	39
IV. MICROELECTRONICS	45
A. Charge-Coupled Imaging Arrays	45
B. Packaging for the CCD Sensor Assembly for the GEODSS Program	46
C. PIN Diode Attenuator	49
D. Computerized Graphic Design	51
V. SURFACE-WAVE TECHNOLOGY	55
A. Reflection Coefficient of a Groove for Right-Angle Reflection on Y-Cut $LiNbO_3$	55
B. Burst Matched Filter	57
C. Bismuth Germanium Oxide Reflective-Array Compressor with 125 μ sec of Dispersion	60
D. Stable CW Operation of Gap-Coupled Si-on- Al_2O_3 to $LiNbO_3$ Acoustoelectric Amplifiers	63

INTRODUCTION

I. SOLID STATE DEVICE RESEARCH

Single-mode GaAs $p^+n^-n^+$ optical striplines have been fabricated with a loss coefficient of 1.2 cm^{-1} at $1.06 \text{ }\mu\text{m}$. The p^+n^- junctions have shown sharp reverse-bias breakdown characteristics at average electric fields in the n^- guiding layer of $1.5 \times 10^5 \text{ V/cm}$. These results suggest the feasibility of developing GaAs modulators, directional couplers, and optical switches having lower loss than those reported previously.

Sheet carrier concentration and mobility for various implant temperatures have been determined for GaAs samples implanted with 1×10^{13} and 1×10^{14} Sn ions cm^{-2} . For 1×10^{14} Sn ions cm^{-2} and implant temperatures in the range 100° to 500°C , the sheet carrier concentration and mobility were $1.8 \times 10^{13} \text{ cm}^{-2}$ and $2400 \text{ cm}^2/\text{V-sec}$, respectively.

CW operation of a tunable PbSnTe double-heterostructure (DH) laser grown by molecular-beam epitaxy has been obtained for heat-sink temperatures just above 77 K . The emission wavelength of this DH diode laser varies from $10.1 \text{ }\mu\text{m}$ at liquid helium temperature to $8.29 \text{ }\mu\text{m}$ at 77 K , giving a temperature tuning range of $1.81 \text{ }\mu\text{m}$ over the region of CW operation.

Large bulk single crystals of PbS with carrier concentrations as low as $2.8 \times 10^{16} \text{ cm}^{-3}$ have been prepared by using a two-temperature zone annealing technique. Evidence for a relatively high degree of carrier concentration homogeneity was obtained from CO_2 laser transmission scans.

II. QUANTUM ELECTRONICS

Room-temperature operation has been obtained in two new stoichiometric neodymium materials: $\text{NdAl}_3(\text{BO}_3)_4$ and $\text{KNdP}_4\text{O}_{12}$. As with neodymium pentaphosphate ($\text{NdP}_5\text{O}_{14}$), the high Nd concentration allows miniature laser operation. In addition the lack of inversion symmetry makes possible harmonic generation and electro-optic modulation in the laser crystal.

Photoluminescence due to recombination of excitons bound to Te impurities in CdS was studied. Spectra and time decays were observed for excitons bound to single Te impurities as well as for excitons bound to nearest-neighbor pairs of Te impurities.

Nearly 75 mW of CW second-harmonic power has been obtained on doubling CO_2 radiation in CdGeAs_2 . The crystals were antireflection coated with ZnS on the entrance and exit faces. Most samples withstood CW power densities in excess of $2 \times 10^5 \text{ W/cm}^2$.

Tripling of CO₂ laser radiation has been observed in SF₆, BCl₃, and CO. In the case of SF₆ and BCl₃, a vibration fundamental was resonant with the first harmonic of CO₂, while for CO the fundamental was resonant with the second harmonic. Frequency, pressure, and pump dependences were studied.

The vibrational relaxation time of liquid nitrogen has been measured to be ~70 sec and is limited mainly by radiative processes. The collisionally induced N₂ absorption band was pumped by an HBr laser, and the fluorescence decay time of CO added to the N₂ was measured as a function of CO concentration.

The technique for generating step-tunable CW far-infrared radiation from non-collinear difference-frequency mixing of radiation from two CO₂ lasers in a GaAs crystal has been used to make high-resolution transmission measurements as a function of pressure of the rotational spectrum of water vapor in the 55- to 56-cm⁻¹ and 62- to 63-cm⁻¹ regions.

III. MATERIALS RESEARCH

Room-temperature operation, with pulsed thresholds as low as 2.8 kA/cm² for broad-area devices, has been achieved for Ga_{1-x}In_xAs_{1-y}P_y/InP double-heterostructure diode lasers emitting at 1.1 μm, where optical fibers have their minimum transmission loss. With thresholds in this range, it should be possible to produce stripe-geometry lasers capable of continuous operation at room temperature, which would be of particular interest for optical communication systems.

Detailed measurements on the photoelectrolysis of water in cells with single-crystal n-type SrTiO₃ anodes have shown that the photoelectrolytic quantum efficiencies obtained in the absence of a bias voltage are about an order-of-magnitude higher for SrTiO₃ than for TiO₂. In addition to confirming that TiO₂ is not unique in its ability to catalyze the photodecomposition of water, these results show that both electron affinity and energy gap must be considered in the search for practical electrode materials to be used in the conversion of solar energy by means of photoelectrolysis.

By determining the angle-of-incidence and primary-electron-energy dependences of the reflection electron energy loss spectra of MgO, it has been possible to distinguish two types of electronic transitions: from Mg core levels to bulk excitonic states like the excited states of the free Mg²⁺ ion, and from the core levels to excitonic states of the surface Mg²⁺ ions that are Stark-split by the intense Madelung electric fields at the surface. Application of this improved technique to TiO₂ and SrTiO₃ should contribute to an increased understanding of the surface electronic states of these compounds that are involved in catalyzing the photoelectrolysis of water.

A new type of transparent heat mirror has been produced by etching a microgrid of square holes 2.5 μm on a side, separated by lines 0.6 μm wide, in a thin film of Sn-doped In₂O₃. The solar transmission is significantly higher for the microgrid than

for the original continuous film; but the infrared reflectivity becomes significantly lower, indicating that films with higher conductivity will probably be required in order for the microgrid technique to result in improved heat-mirror performance for solar energy applications.

IV. MICROELECTRONICS

A prototype, 30- × 30-element, CCD imaging array has been fabricated and tested as part of the development effort aimed at realizing a 100- × 400-element CCD array for the GEODSS (Ground Electro-Optical Deep Space Surveillance) Program. Tests on this prototype have revealed difficulties in transferring charge for test purposes through the channels between the input (test) and output registers and the CCD array, and problems with the level of the output signal caused by a large capacitance in the diode-MOSFET preamplifier structure. Somewhat imprecise optical measurements have indicated that these devices have transfer inefficiencies of less than 10^{-3} . Two redesigned 30 × 30 prototypes are being fabricated which will incorporate changes in structure and processing to reduce the charge transfer problem between the registers and the CCD array, and to increase the output signal by reducing the capacitance in the output circuitry.

The detector being built for use at the prime focus of a 31-inch telescope in the GEODSS Program will be a hybrid integrated circuit consisting of sixteen 100- × 400-element, CCD imaging arrays mounted on an alumina interconnect substrate. The individual arrays must be aligned on the substrate to within 0.0005 in. and be parallel to within 0.03°. The hybrid will be fabricated on a multilevel interconnect substrate. The individual arrays will be located and placed using a modified x-y coordinator with 0.0002-in. accuracy, and die attachment will be accomplished with an anerobic, fast-setting adhesive.

An electronically variable attenuator has been built as a chip-and-wire hybrid for use in the UHF receiver of the proposed LES-10 satellite. The circuit is a bridged-T attenuator whose basic components are two PIN diodes which function as current-controlled, variable resistors, and two Ta₂N, thin-film resistors. This circuit in hybrid form has at least 25 dB of attenuation between 30 and 400 MHz, as opposed to the discrete version of the same circuit which had a maximum of 18 dB of attenuation at 400 MHz.

The mask-making facility of the Microelectronics Group requires software to be used in conjunction with the IBM 370/168 and the Calma interactive graphic design system to provide input to a D. W. Mann Model 1600 pattern generator. Two important programs, CALMASRT and MANNPLOT, have been written and updated, respectively, to improve the operation of the facility. CALMASRT takes the data from the Calma system and sorts the data to minimize the running time of the pattern generator. MANNPLOT is a user-oriented program that allows patterns to be designed on the 370/168 system, and then creates the file or files needed to generate the mask on the pattern generator.

V. SURFACE-WAVE TECHNOLOGY

The Rayleigh-wave reflection coefficient of shallow grooves has been measured on Y-cut LiNbO_3 for waves reflected from the Z- to the X-direction. This 90° reflection geometry is used in surface-acoustic-wave (SAW) devices such as the reflective-array compressor (RAC) and the burst matched filter. The reflection coefficient of each edge of a groove has a real and an imaginary part. The real part is proportional to groove depth and contributes mainly to the amplitude of reflections, while the imaginary part is proportional to the square of the groove depth and leads to phase shifts on transmission.

A burst matched filter has been designed and fabricated using the reflective-array technology. The device is a 15-cm-long LiNbO_3 crystal with an input and an output transducer and 16 pairs of shallow gratings in its surface. The gratings selectively reflect SAWs whose wavelength satisfies a Bragg condition. The impulse response of the device is a train of 16 linear-FM subpulses. The filter compresses a Doppler-sensitive radar waveform to which the filter is matched. It can resolve a Doppler shift of 20 kHz.

Linear-FM pulse expanders and compressors in the reflective-array configuration have been fabricated on bismuth-germanium-oxide substrates. The low surface-wave velocity on this material and the folded RAC configuration allow 125 μsec of dispersion over the 2.5-MHz bandwidth to be obtained in a compact device. Controlled spatial variations in reflectivity achieved by etching gratings to varying depths were employed to provide spectral weighting in the frequency response of the devices. Special procedures for ion-beam etching, metalization, and bonding were developed for use on bismuth-germanium-oxide.

Acoustoelectric amplifiers have been developed to provide distributed on-substrate loss compensation of very long SAW delay lines as a means of maintaining wide bandwidth and large dynamic range. The gap-coupled silicon-on-sapphire (SOS) to LiNbO_3 configuration is the first SAW amplifier which exhibits stable DC operation with gain and noise performance that matches theoretical predictions. Optimum performance results because traps within the SOS film prevent intense fringing fields from distorting the homogeneity of the electron sheet.

REPORTS ON SOLID STATE RESEARCH

15 August through 15 November 1975

PUBLISHED REPORTS

Journal Articles

JA No.

4339	Many-Body Treatment of Pressure Shifts Associated with Collisional Broadening	R. W. Davies	Phys. Rev. A <u>12</u> , 927 (1975), DDC AD-A017353
4453	Etude des Proprietes Magnetiques, Electriques et Optiques des Phases de Structure Perovskite $\text{SrVO}_{2.90}$ et SrVO_3	P. Dougier* J. C. C. Fan J. B. Goodenough	J. Solid State Chem. <u>14</u> , 247 (1975)
4469	Low-Threshold, Transversely Excited $\text{NdP}_5\text{O}_{14}$ Laser	S. R. Chinn J. W. Pierce H. Heckscher	IEEE J. Quantum Electron. <u>QE-11</u> , 747 (1975), DDC AD-A017355
4503	Integrated GaAs-AlGaAs Double-Heterostructure Lasers	C. E. Hurwitz J. A. Rossi J. J. Hsieh C. M. Wolfe	Appl. Phys. Lett. <u>27</u> , 241 (1975), DDC AD-A016699
4511	Crystallization of Amorphous Silicon Films by Nd:YAG Laser Heating	J. C. C. Fan H. J. Zeiger	Appl. Phys. Lett. <u>27</u> , 224 (1975), DDC AD-A016696
4524	Coherent Integration and Correlation in a Modified Acoustoelectric Memory Correlator	K. A. Ingebrigtsen E. Stern	Appl. Phys. Lett. <u>27</u> , 170 (1975), DDC AD-A016688
4531	Optically Pumped Infrared V-V Transfer Lasers	H. Kildal T. F. Deutsch	Appl. Phys. Lett. <u>27</u> , 500 (1975)
4537	Photoelectrolysis of Water in Cells with TiO_2 Anodes	J. G. Mavroides D. I. Tchernev J. A. Kafalas D. F. Kolesar	Mater. Res. Bull. <u>10</u> , 1023 (1975), DDC AD-A017419
4543	Crystal Structure of Potassium Neodymium Metaphosphate, $\text{KNdP}_4\text{O}_{12}$, A New Acentric Laser Material	H. Y-P. Hong	Mater. Res. Bull. <u>10</u> , 1105 (1975), DDC AD-A017268

*Author not at Lincoln Laboratory.

Meeting Speeches

MS No.

- | | | | |
|------|---|--|---|
| 3720 | GaAs Schottky Barrier Avalanche Diodes for Integrated Waveguide Photodetectors at 0.905 μm | G. E. Stillman
C. M. Wolfe
J. A. Rossi
J. L. Ryan | In <u>Optical and Acoustical Microelectronics</u> , J. Fox, Ed. (Polytechnic Press, Brooklyn, New York, 1975), p. 543 |
| 3979 | Surface-Wave Resonators Using Grooved Reflectors | R. C. M. Li
J. A. Alusow
R. C. Williamson | Proc. 29th Annual Symposium on Frequency Control, Atlantic City, 28-30 May 1975, pp. 167-176, DDC AD-A017356 |

* * * * *

UNPUBLISHED REPORTS

Journal Articles

JA No.

- | | | | |
|-------|--|---|---|
| 4443 | Frequency Stabilization and Absolute Frequency Measurements of a cw HF/DF Laser | R. S. Eng
D. L. Spears | Accepted by Appl. Phys. Lett. |
| 4461 | External Cavity CO ₂ Pumped InSb Spin-Flip Laser | S. R. J. Brueck
A. Mooradian | Accepted by IEEE J. Quantum Electron. |
| 4465 | The Molecular Contribution to the Infrared Laser Transmittance of the Natural Atmosphere | P. L. Kelley
R. A. McClatchey*
R. K. Long*
A. Snelson* | Accepted by Optical and Quantum Electronics |
| 4469A | Low-Threshold, Transversely-Excited NdP ₅ O ₁₄ Laser | S. R. Chinn
J. W. Pierce
H. Heckscher | Accepted by Appl. Opt. |
| 4487 | Properties of Sn-Doped In ₂ O ₃ Films Prepared by RF Sputtering | J. C. C. Fan
F. J. Bachner | Accepted by J. Electrochem. Soc. |
| 4488 | Optically Pumped 15.90 μm SF ₆ Laser | H. R. Fetterman
H. R. Schlossberg*
W. E. Barch | Accepted by Opt. Commun. |
| 4496 | Applications of Infrared Lasers to Spectroscopy | A. H. M. Ross*
P. L. Kelley
K. W. Nill | Accepted in <u>Applications of Lasers to Atomic and Molecular Physics</u> (North-Holland Publishing Company, Amsterdam) |
| 4528 | The Application of Moiré Techniques in Scanning Electron Beam Lithography and Microscopy | H. I. Smith
S. R. Chinn
P. D. DeGraff | Accepted by J. Vac. Sci. Technol. |

* Author not at Lincoln Laboratory.

JA No.

4532	Prospects for X-Ray Fabrication of Silicon IC Devices	H. I. Smith S. E. Bernacki	Accepted by J. Vac. Sci. Technol.
4541	CW Laser Action in Acentric NdAl ₃ (BO ₃) ₄ and KNdP ₄ O ₁₂	S. R. Chinn H. Y-P. Hong	Accepted by Opt. Commun.
4545	Spiking Oscillations in Diode-Pumped NdP ₅ O ₁₄ and NdAl ₃ (BO ₃) ₄ Lasers	S. R. Chinn H. Y-P. Hong J. W. Pierce	Accepted by IEEE J. Quantum Electron.
4547	Isotope Separation Involving Photoinduced Changes in the Electric and Magnetic Properties of Molecules and Atoms	P. L. Kelley N. M. Kroll* C. K. Rhodes*	Accepted by Opt. Commun.
MS-4067	Recent Advances in Tunable Infrared Lasers	A. Mooradian	Accepted by Soviet J. Quantum Electron.

Meeting Speeches†

MS No.

3467A	Electron Delocalization in the Solid State	J. B. Goodenough	Symposium on Delocalized Electrons in Solids, Brown University, 21 August 1975
4059A	Photoelectrolysis of Water on Semiconducting Surfaces	D. I. Tchernev	Seminar, I.B.M., Yorktown Heights, N.Y., 1 October 1975; Brown University, 6 November 1975
4062	Nucleation and Surface Morphology of LPE GaAs and GaAlAs Grown from Supercooled Solutions	J. J. Hsieh	148th Meeting of the Electrochemical Society, Dallas, Texas, 5-10 October 1975
4088	Experimental Exploration of the Limits of Achievable Q of Grooved Surface-Wave Resonators	R. C. M. Li J. A. Alusow R. C. Williamson	1975 IEEE Ultrasonics Symposium, Los Angeles, 22-24 September 1975
4090	BGO Reflective-Array Compressor (RAC) with 125 μsec of Dispersion	V. S. Dolat R. C. Williamson	
4091	Measurement of Impedance Mismatch and Stored Energy for Right-Angle Reflection of Rayleigh Waves from Grooves on Y-Cut LiNbO ₃	J. Melngailis R. C. M. Li	
4093	Stable CW Operation of Gap-Coupled Silicon-on-Sapphire to LiNbO ₃ Acoustoelectric Amplifiers	R. W. Ralston	

* Author not at Lincoln Laboratory.

† Titles of Meeting Speeches are listed for information only. No copies are available for distribution.

MS No.

4098	Programmable Matched Filtering with Acoustoelectric Convolver in Spread-Spectrum Systems	J. H. Cafarella J. A. Alusow W. M. Brown E. Stern	} 1975 IEEE Ultrasonics Symposium, Los Angeles, 22-24 September 1975
4100	Holographic Storage of Acoustic Surface Waves with Schottky Diode Arrays	K. A. Ingebrigtsen E. Stern	
4101	Acoustic Memories	E. Stern	
4104	Reflective-Array Matched Filter for a 16-Pulse Radar Burst	R. C. Williamson V. S. Dolat J. Melngailis	
4094	GaAs-Based Integrated Optical Circuits	I. Melngailis	Electro-Optics '75 Anaheim, California, 11-13 November 1975
4128, 4128A	GaAs-Based Integrated Optical Circuits	C. E. Hurwitz	Seminar, American Vacuum Society, Lexington, Massachusetts, 1 October 1975; Optics Seminar, M.I.T., 16 October 1975
4137	Measurement of Vibrational-Vibration Exchange Rates for Excited Vibrational Levels in Hydrogen Fluoride Gas	R. M. Osgood, Jr.	Army Symposium on High Energy Lasers, Redstone Arsenal, Alabama, 3-4 November 1975

ORGANIZATION

SOLID STATE DIVISION

A. L. McWhorter, *Head*
I. Melngailis, *Associate Head*
C. R. Grant, *Assistant*

P. E. Tannenwald
H. J. Zeiger

QUANTUM ELECTRONICS

A. Mooradian, *Leader*
P. L. Kelley, *Associate Leader*

Barch, W. E.	Kildal, H.
Brueck, S. R. J.	Larsen, D. M.
Burke, J. W.	Mandel, P.*
Chinn, S. R.	Menyuk, N.
DeFeo, W. E.	Moulton, P. F.*
Deutsch, T. F.	Osgood, R. M.
Fetterman, H. R.	Parker, C. D.
Hancock, R. C.	Pine, A. S.
Heckscher, H.	

APPLIED PHYSICS

A. G. Foyt, *Leader*
T. C. Harman, *Assistant Leader*
C. E. Hurwitz, *Assistant Leader*

Belanger, L. J.	McBride, W. F.
Calawa, A. R.	Orphanos, W. G.
Carter, F. B.	Paladino, A. E.
DeMeo, N. L., Jr.	Reeder, R. E.
Donnelly, J. P.	Rossi, J. A.
Ferrante, G. A.	Spears, D. L.
Groves, S. H.	Tsang, D.*
Leonberger, F. J.	Walpole, J. N.
Lind, T. A.	

ELECTRONIC MATERIALS

J. B. Goodenough, *Leader*
A. J. Strauss, *Associate Leader*

Anderson, C. H., Jr.	Krohn, L., Jr.
Animalu, A. O. E.	LaFleur, W. J.
Button, M. J.	Mastromattei, E. I.
Delaney, E. J.	Mavroides, J. G.
Dresselhaus, G.	Mroczkowski, I. H.
Dwight, K., Jr.	Oli, B.*
Fahey, R. E.	Owens, E. B.
Fan, J. C. C.	Palm, B. J.
Feldman, B.	Pantano, J. V.
Finn, M. C.	Pierce, J. W.
Henrich, V. E.	Plonko, M. C.
Hong, H. Y-P.	Reed, T. B.
Ilsieh, J. J.	Tchernev, D. I.
Iseler, G. W.	Tracy, D. M.
Kafalas, J. A.	Vohl, P.
Kolesar, D. F.	Zavracky, P. M.

SURFACE WAVE TECHNOLOGY

E. Stern, *Leader*
R. C. Williamson, *Assistant Leader*

Alusow, J. A.	Kernan, W. C.
Brogan, W. T.	Li, R. C. M.
Cafarella, J. H.	Melngailis, J.
DeGraff, P. D.	Ralston, R. W.
Dolat, V. S.	Reible, S. A.
Efremow, N., Jr.	Smith, H. I.
Flanders, D. C.*	Vlannes, N.*

MICROELECTRONICS

W. T. Lindley, *Leader*
F. J. Bachner, *Assistant Leader*

Beatrice, P. A.	Gray, R. V.
Bozler, C. O.	Lincoln, G. A., Jr.
Burke, B. E.	McGonagle, W. H.
Clough, T. F.	Mountain, R. W.
Cohen, R. A.	Murphy, R. A.
Durant, G. L.	Pichler, H. H.
Foley, G. H.	Smythe, D. L., Jr.
Grant, L. L.	Wilde, R. E.

* Research assistant

I. SOLID STATE DEVICE RESEARCH

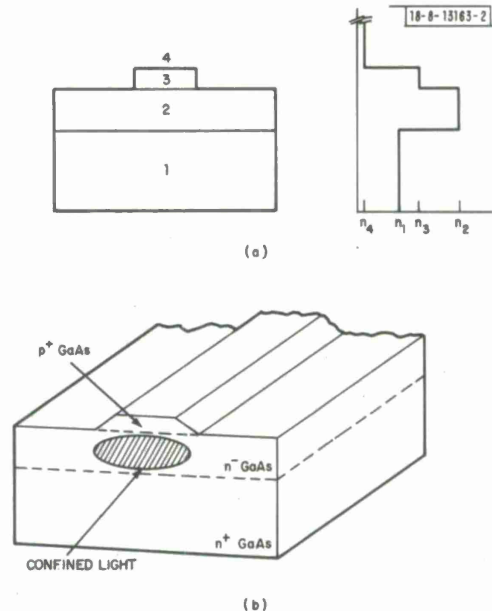
A. LOW-LOSS GaAs $p^+n^-n^+$ OPTICAL STRIPLINES FABRICATED USING Be^+ -ION IMPLANTATION

The development of GaAs-based integrated optical circuits (IOCs) requires low-loss three-dimensional waveguides to transmit and confine the optical signal to specific locations on a chip, and also to fabricate various optical components. In this report, we will describe the successful fabrication of single-mode $p^+n^-n^+$ optical striplines. These striplines have exhibited low loss ($\alpha \approx 1.2 \text{ cm}^{-1}$ at $1.06 \mu\text{m}$), and the p^+n^- junctions have shown sharp breakdown voltages corresponding to average electric fields in the n^- guiding layer of $1.5 \times 10^5 \text{ V/cm}$. This suggests the feasibility of developing low-loss GaAs modulators, directional couplers, and optical switches based on the electroabsorption or electro-optic effects.

A cross-section sketch of the optical stripline structure¹ is shown in Fig. I-1(a), along with a sketch of the variation of refractive index in this structure. The device consists of a lower-index rib over a higher-index slab on a low-index substrate. Light propagating in the device is confined under the rib, since the effective refractive index is largest there. Because the light propagates in the higher-index slab rather than in the rib, this device should have lower loss than some other rib structures,² since scattering losses due to rib edge roughness are minimized.

The guide structure reported here, shown schematically in Fig. I-1(b), was fabricated entirely in GaAs and consists of a p^+ rib on an undoped n^- epilayer grown on an n^+ substrate. It offers several advantages over other three-dimensional GaAs guides previously reported. In comparison to striplines with n^+ ribs,³ this junction device has been found to have a similarly low loss, but allows for the application of high electric fields with low leakage currents (by

Fig. I-1. Schematic diagrams of (a) optical stripline showing cross section of structure to left and refractive index profile to right - region 4 is usually air, and (b) GaAs $p^+n^-n^+$ optical stripline showing propagating light confined in undoped slab under rib. Sloped sides of rib result from rib etching procedure.



reverse-biasing the p^+-n^- junction). This should facilitate the fabrication of modulators and switches using electroabsorption and/or electro-optic effects. Schottky-barrier devices,^{4,5} which do permit electro-optic effects, and proton-bombarded embedded stripes⁶ have higher losses than these $p^+-n^-n^+$ guides.

The striplines were fabricated by growing an undoped layer by vapor-phase epitaxy on a (100)-oriented $1.2 \times 10^{18} \text{ cm}^{-3}$ n-type substrate. The layer was n-type, with a concentration of $1 \times 10^{14} \text{ cm}^{-3}$, a mobility at 77 K of $108,000 \text{ cm}^2/\text{V-sec}$, and a thickness of $10 \mu\text{m}$. The p^+ layer was formed by implanting the epilayer with Be ions (Ref. 7) with doses of $1.5 \times 10^{14} \text{ cm}^{-2}$ at 400 keV, $1.2 \times 10^{14} \text{ cm}^{-2}$ at 220 keV, and $1.2 \times 10^{14} \text{ cm}^{-2}$ at 100 keV. Beryllium was chosen because it is the p-type dopant having the maximum penetration depth in GaAs; the three doses were chosen to create a uniformly doped layer. Following the implantation, the wafer was annealed at 900°C for 15 min. using a pyrolytic- Si_3N_4 encapsulation technique.⁸

Evaluation of this implantation technique by a series of etching steps and Hall measurements on high-resistivity Cr-doped GaAs samples indicated that the implanted layers had a relatively constant p-type carrier concentration of $2 \times 10^{18} \text{ cm}^{-3}$ to a depth of about $1.5 \mu\text{m}$. To our knowledge, this is the first report of uniform high doping of GaAs by ion implantation. In the actual stripline, the junction depth in the n^- epilayer was found to be about $2 \mu\text{m}$.

The ribs were formed by first defining stripes of several widths in an $\sim 300\text{-\AA}$ sputtered-Ti layer using standard photolithographic and etching techniques. The stripes were oriented along a (011) direction. The GaAs was etched down through the p^+ layer, using Ti as a mask, in a cooled free-etch solution at a rate of $\sim 2 \mu\text{m}/\text{min}$. For the orientation chosen, the sides of the ribs etched at a 45° angle as indicated in Fig. I-1(b). The time required to etch through the p^+ -implanted layer was determined by etching for short times and monitoring the current-voltage characteristic between two adjacent test areas on a curve tracer. After etching through the p^+ layer, these isolated junctions had low leakage and sharp breakdowns at voltages corresponding to average fields in the undoped layer of $1.5 \times 10^5 \text{ V/cm}$. The finished devices had a rib height of $2 \mu\text{m}$, an n^- -layer thickness of $8 \mu\text{m}$, and rib widths that varied from ~ 7 to $27 \mu\text{m}$ across the chip. After the ends were cleaved, samples were mounted on a high-precision translation-rotation stage for optical evaluation.

Transmission measurements were made using an end-fire coupling scheme. Radiation from a Nd:YAG laser at $1.06 \mu\text{m}$ was passed through a polarizer and a beam expander, and focused on the waveguide input face using a microscope objective. Measurements were made with the electric field vector of the light polarized parallel to the plane of the slab (i.e., TE polarization). For devices reported here, a single intensity maximum was observed under the p^+ rib as expected, since the stripline geometry was designed for single-mode propagation using Marcatili's analytical expressions.⁹ Transmission measurements through several lengths of the same sample yielded an attenuation coefficient of 1.2 cm^{-1} for a stripline having an $\sim 17\text{-}\mu\text{m}$ -wide rib. As mentioned previously, this value is comparable to the lowest value reported for three-dimensional GaAs guides and suggests that GaAs modulators, directional couplers, and optical switches having lower losses than any previously reported could be fabricated using p^+-n^- striplines.

F. J. Leonberger
J. P. Donnelly
C. O. Bozler

B. ELECTRICAL PROPERTIES OF TIN ION-IMPLANTED GaAs

We have previously reported the electrical characteristics of Se (Refs. 8 and 10 to 13) and Si (Ref. 8 and p. 2 in Ref. 12) ion-implanted GaAs. For the column VI n-type dopant Se, ion implantation into heated GaAs substrates was required to achieve high doping efficiency. The necessity of heated substrates has also been reported for the other column VI n-type dopants Te (Refs. 14 and 15) and S (Ref. 16). Unlike Se, we reported that the electrical activity of implanted Si (Refs. 8 and 13), a column IV element, did not increase significantly as the temperature of the GaAs substrate during implantation was increased above room temperature. In this section, we will present some preliminary results on the implantation of tin, another column IV element, in GaAs. Some results on the electrical activity of implanted Sn have been reported previously,¹⁷ but those results were restricted to implant doses $\geq 10^{14}$ cm⁻² and post-implantation anneal temperatures of 700°C.

The GaAs substrates used in these experiments were Cr-doped semi-insulating GaAs. After polishing and etching, a 700-Å layer of Si₃N₄ was pyrolytically deposited at 720°C on each sample. Details of this pyrolytic Si₃N₄ process can be found in previous reports.^{8,13}

The 400-keV Sn⁺ ions were implanted through the Si₃N₄ overcoating at substrate temperatures ranging from room temperature to 500°C. The projected range and standard deviation^{18,19} of 400-kV Sn⁺ ions in GaAs are 0.0958 and 0.0207 μm, respectively. In Si₃N₄, the respective numbers are 0.0971 and 0.0117 μm. The peaks of the implanted Sn concentration in these experiments will therefore lie close to the GaAs surface. After implantation, a 2000-Å pyrolytic SiO₂ layer was deposited at 400°C over the Si₃N₄. Anneals then were carried out in a flowing N₂ atmosphere at 900°C for 15 min. The SiO₂ and Si₃N₄ layers then were removed in HF. To minimize contact effects while carrying out Hall measurements of the van der Pauw type,²⁰ electrically isolated cloverleaf-shaped mesas were defined in the implanted layer using 6000 Å of pyrolytic SiO₂ as an etch mask. Good linear contacts were obtained with alloyed Au-Sn. More complete details of the sample processing steps can be found in Ref. 8 and p. 2 of Ref. 12.

All the Sn implants performed have resulted in n-type conductivity. Figures I-2 and I-3 show the measured sheet carrier concentration and sheet mobility, respectively, as a function of implant temperature for doses of 1×10^{13} and 1×10^{14} cm⁻². For doses of 1×10^{14} cm⁻², the sheet carrier concentration increased an order of magnitude, from about 1.8×10^{12} cm⁻² to 1.8×10^{13} cm⁻², when the temperature during implantation was increased from room temperature to 100°C. For implant temperatures between 100° and 500°C, the sheet carrier concentration was relatively independent of implant temperature, varying somewhat arbitrarily between 1.5×10^{13} and 2.1×10^{13} cm⁻². These variations could be due to slight differences in the thickness of the Si₃N₄ overcoating and/or differences in the amount of compensation in the Cr-doped semi-insulating substrates. As shown in Fig. I-3, the sheet mobility was also relatively constant (≈ 2400 cm²/V-sec) for implant temperatures between 100° and 500°C. The mobility of the 1×10^{14} cm⁻² room-temperature implant was higher, 3680 cm²/V-sec, than that of the heated implants. This is most likely due to the probability that for the room-temperature implant only the tail of the implant distribution is electrically active.^{8,12}

For doses of 1×10^{13} cm⁻², the sheet carrier concentration of a 300°C implant was 3.1×10^{12} cm⁻², which was only about 20-percent higher than that measured for a room-temperature implant (2.6×10^{12} cm⁻²). The sheet mobilities of the room-temperature and 300°C implants were 3695 and 3455 cm²/V-sec, respectively.

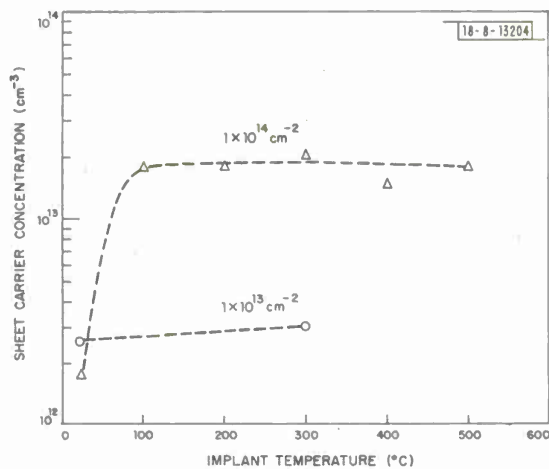


Fig. I-2. Sheet carrier concentration vs temperature of implant for 400-keV Sn^+ ion-implanted GaAs annealed at 900°C . Implants were made through 700 \AA of pyrolytic Si_3N_4 .

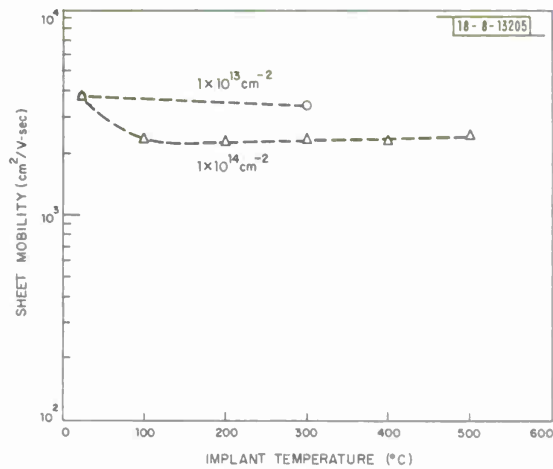


Fig. I-3. Sheet mobility vs temperature of implant for 400-keV Sn^+ ion-implanted GaAs annealed at 900°C .

Additional measurements are planned which will determine the electron concentration profiles and the maximum peak carrier concentrations obtainable for both room-temperature and heated Sn implantations.

J. P. Donnelly
G. A. Ferrante

C. MOLECULAR-BEAM EPITAXIAL $\text{Pb}_{1-x}\text{Sn}_x\text{Te}$ DOUBLE-HETEROSTRUCTURE LASERS WITH CW OPERATION AT 77 K

We have obtained CW operation of a $\text{Pb}_{1-x}\text{Sn}_x\text{Te}$ double-heterostructure (DH) laser grown by molecular-beam epitaxy (MBE) for heat-sink temperatures up to just above 77 K. Previously, CW laser operation at this temperature and in this alloy system was reported for devices grown by liquid-phase epitaxy (LPE).²¹ The MBE device is quite similar both in structure and performance to the LPE device.

The substrate used was grown by seeded, vertical, vapor growth²² in a closed tube and was doped with Tl to assure p-type conductivity^{21,23} ($\sim 5 \times 10^{18} \text{ cm}^{-3}$). A stripe geometry was employed using an insulating layer of MgF_2 patterned with $50\text{-}\mu\text{m}$ -wide stripes. Two epitaxial layers were then grown in the stripes. A polycrystalline, discontinuous film also grew over the MgF_2 . Using the MBE technique discussed previously,²⁴ we grew the layers at a rate of $2 \mu\text{m/hr}$ with the substrate at 425°C . The active layer was grown $1.5 \mu\text{m}$ thick from a source of composition $(\text{Pb}_{0.88}\text{Sn}_{0.12})_{0.4991}\text{Te}_{0.5009}$ doped with Bi ($\sim 1 \times 10^{18} \text{ cm}^{-3}$) to obtain n-type conductivity.²² The last layer was grown $0.75 \mu\text{m}$ thick using a $\text{Pb}_{0.4998}\text{Te}_{0.5002}$ source doped with $\sim 3 \times 10^{18} \text{ cm}^{-3}$ of Bi.

Devices $500 \mu\text{m}$ in length were fabricated using a standard technique,²⁵ with the significant exception that the devices were cut both on the sides and at the laser end-mirrors using a high-speed diamond-blade saw. We found this superior to the usual technique of cleaving for these DH lasers in side-by-side comparisons. Further study of the mirror smoothness and damage introduced using the saw-cutting technique vs cleaving is under way.

TABLE I-1 DH-LASER THRESHOLDS AND WAVELENGTH OF OPERATION		
Heat-Sink Temperature (K)	J_{th} (kA/cm ²)	Wavelength (μm)
Pulsed		
4.2	0.89	10.4
77	2.13	8.74
CW		
4.2	1.36	10.1
77	5.16	8.29
Device area = 2.58×10^{-4} cm ²		

A summary of threshold current densities measured at 4.2 and 77 K is given in Table I-1 for CW operation and for 1-μsec pulses at 6-kHz repetition rate. The approximate wavelength of operation also is indicated. From the difference in wavelength for pulsed vs CW operation, we can estimate that the junction temperature reaches 90 to 100 K for a 77-K heat-sink temperature.

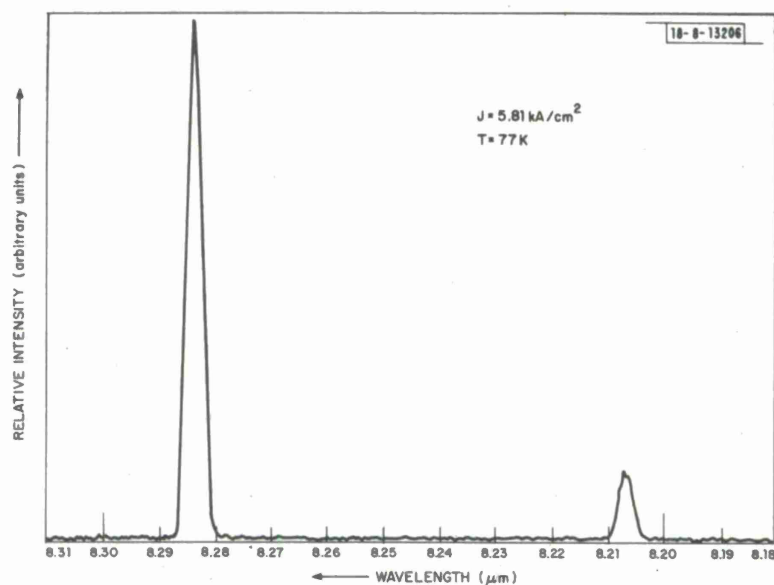


Fig. I-4. Emission spectrum of $Pb_{1-x}Sn_xTe$ DH laser operating CW immersed in liquid nitrogen. Junction temperature is estimated to be ~ 100 K.

Figure I-4 shows the spectrum measured at 5.81 kA/cm² with the device immersed in liquid nitrogen. Similar spectra were obtained for current densities up to 8.24 kA/cm². Throughout the range of current densities from 5.16 to 8.24 kA/cm², most of the energy was in a single

longitudinal mode. Accurate output-power measurements have not been obtained nor has the maximum current density for CW operation been established. We can estimate by comparison with other laser devices, however, that at least several hundred microwatts of output power are obtained.

J. N. Walpole
A. R. Calawa
T. C. Harman

D. PREPARATION OF LOW CARRIER CONCENTRATION PbS CRYSTALS

At the present time, there is considerable interest in PbS single crystals for infrared detectors²⁶ and tunable lasers.²⁵ Further device development will depend, in part, on additional advances in single-crystal quality. By using a two-temperature zone annealing technique, carrier concentrations as low as $2.8 \times 10^{16} \text{ cm}^{-3}$ have been achieved in large bulk single crystals of PbS. Evidence for a relatively high degree of carrier concentration homogeneity was obtained by CO₂ laser transmission scans.²⁷

Single crystals of PbS were grown by both the standard Bridgman (B) and the horizontal unseeded vapor growth²⁸ (HUVG) methods. Previously, studies²⁹ on PbS showed that annealing the compound in sulfur vapor at pressures above a critical pressure results in p-type PbS, while annealing the compound at lower pressures results in n-type PbS.

Specimens ($12 \times 4 \times 0.5$ to 1.1 mm) were cut from larger crystals, etch-polished, and annealed at 600°C under various pressures of sulfur usually for 49 days. For a typical experiment, one PbS crystal along with a small quantity of sulfur powder was sealed in a quartz tube, which is back-filled with argon to a pressure of about 300 Torr. The ampoule was placed in a two-zone horizontal furnace; one zone controlled the sulfur pressure and the other provided the annealing temperature of the sample. Specimens were quenched in water from the final annealing temperature. Surface damage and thin n-type surface layers were removed by immersing the crystals in an aqueous solution of 48-weight-percent HBr for 1 min. and finally rinsing in methanol. The thickness of the samples was reduced 0.1 mm by the etching step.

Table I-2 lists the carrier concentration, type, and mobility obtained by Hall coefficient and resistivity measurements on the annealed and etched crystals at 77 K, and the thermoelectric power measured at 300 K. Table I-2 also lists the crystal growth method and the annealing parameters.

Using a CO₂ laser with a beam focused to a 125- μm diameter, we carried out transmission scans at 300 K on various specimens. These scans revealed that most samples were inhomogeneous with respect to the intensity of CO₂ radiation transmitted. Figure I-5(a) shows a typical CO₂ laser transmission profile across PbS sample B-3. The random variations in transmission correspond to substantial carrier concentration fluctuations which are observed over the entire specimen. On the other hand, Fig. I-5(b) shows a typical scan across PbS sample B-2 which indicates a relatively uniform carrier concentration. The explanation for the relatively homogeneous carrier concentration result for B-2 is believed to be associated with the second, lower-temperature annealing step. For single-ionized defects, the dependence of the hole carrier concentration p on sulfur vapor pressure can be expressed by the relationship

$$p = \frac{k n_i^{1/2} [\varphi^{1/2} - (1/\varphi)^{1/2}]}{(n_i + k \varphi^{1/2})^{1/2} [1 + (k/n_i \varphi^{1/2})^{1/2}]^{1/2}}$$

where k is the equilibrium defect constant, n_i is the intrinsic carrier concentration, and φ is

TABLE I-2
SUMMARY OF SALIENT ANNEALING AND CHARACTERIZATION DATA FOR PbS

Crystal Growth Technique	Carrier Concentration and Type at 77 K (cm ⁻³)	Carrier Mobility at 77 K (cm ² /V-sec)	Thermoelectric Power at 300 K (μV/K)	Thickness of Sample (cm)	Temperature of Sample (°C)	Temperature of Sulfur (°C)	Annealing Time (days)
B [†] -1	2.8 × 10 ¹⁶ P	17,000	+588	0.069	600 400	90 50	49 21
HUVG [†] -1	4.7 × 10 ¹⁶ P	12,000	+505	0.091	600 400	90 50	49 7
B [†] -2	7 × 10 ¹⁶ P	17,000	+482	0.093	600 400	90 50	49 7
B-3	1 × 10 ¹⁷ P	10,000	+482	0.100	600	95	49
B-4	1.8 × 10 ¹⁷ P	15,000	+410	0.100	600	98	49
B-5	5.8 × 10 ¹⁷ P	11,000	+356	0.037	600	110	49
B-6	4 × 10 ¹⁷ P	16,000	+384	0.105	600	110	49
B-7	9.2 × 10 ¹⁷ P	15,000	+361	0.103	600	129	58
B-8	1.1 × 10 ¹⁸ P	18,000	+352	0.100	600	141	58
HUVG-2	2.2 × 10 ¹⁸ P	13,000	+275	0.077	600	190	49
HUVG-3	3.1 × 10 ¹⁸ P	13,000	+257	0.070	600	220	49
HUVG-4	3.5 × 10 ¹⁸ P	15,000	+241	0.083	600	250	49
HUVG-5	3.5 × 10 ¹⁸ P	13,000	+239	0.070	600	260	49
HUVG-6	4.8 × 10 ¹⁸ P	12,000	+237	0.069	600	270	49
HUVG-7	4 × 10 ¹⁷ N	14,000	-393	0.087	600	80	49
HUVG-8	5.4 × 10 ¹⁷ N	15,000	-379	0.053	600	84	49

† For these three crystals, the ampoule was furnace-cooled between 600° and 400°C, and finally water-quenched from 400°C.

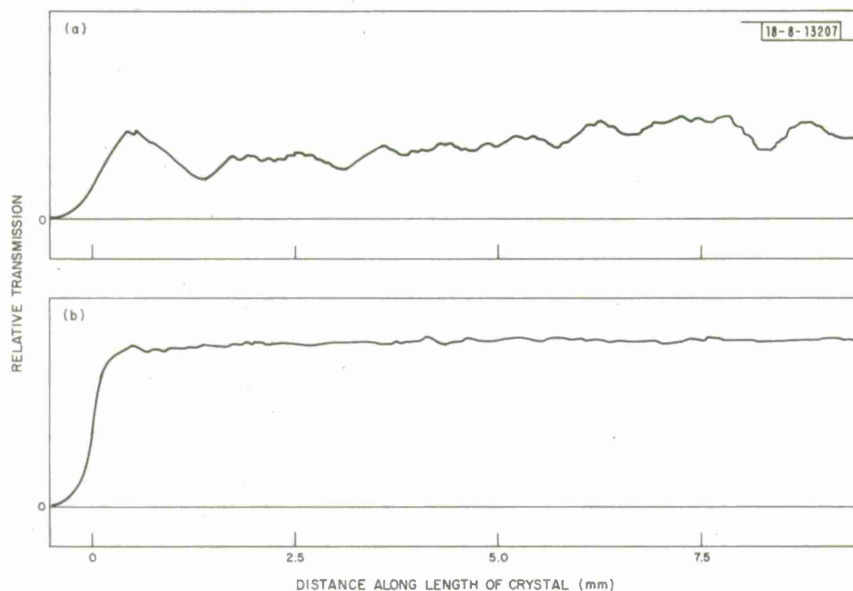


Fig. I-5. Typical CO₂ laser transmission profiles across two PbS crystals. Profile in (a) is for crystal B-3, whereas profile in (b) is for crystal B-2 of Table I-2.

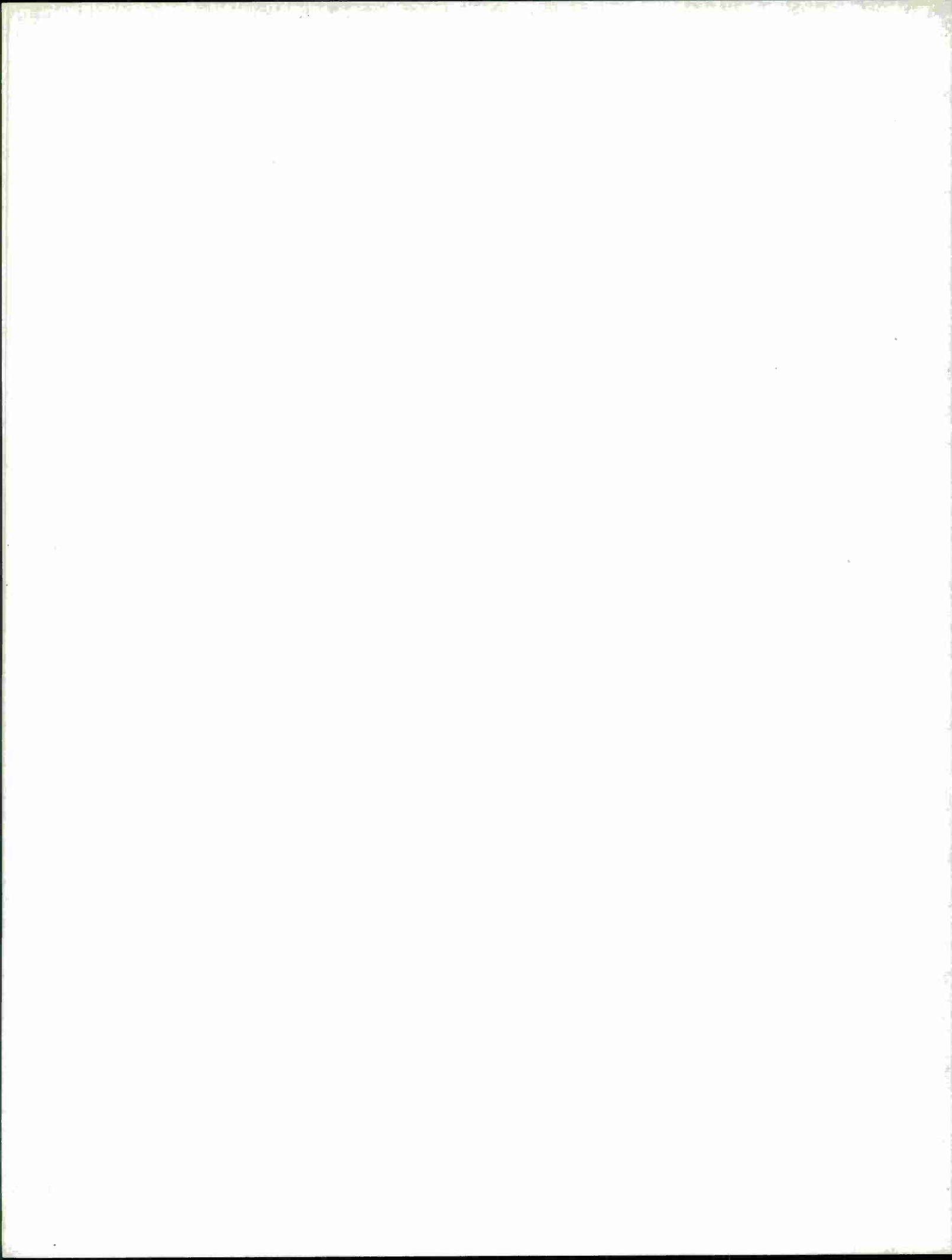
the ratio of the vapor pressure of S₂ to the vapor pressure of S₂ at the p-n crossover. Upon application of the above expression to the data of Table I-2, the equilibrium lattice point defect concentration for PbS at 600°C was calculated to be $5 \times 10^{17} \text{ cm}^{-3}$ defects. However, it is estimated that the equilibrium defect density at 400°C is reduced to approximately $1 \times 10^{16} \text{ cm}^{-3}$ defects. Thus, for homogeneous low carrier concentration PbS, a second lower-temperature anneal is required in order to take advantage of the low equilibrium defect density. The higher-temperature anneal is needed in order to take advantage of the higher diffusion coefficients of the compound constituents. Further details of this investigation will be published in the Journal of Electronic Materials.

T. C. Harman
A. E. Paladino

REFERENCES

1. H. Furuta, H. Noda, and A. Ithaya, *Appl. Opt.* **13**, 322 (1974).
2. For a review, see H. Kogelnik, *IEEE Trans. Microwave Theory Tech.* **MTT-23**, 2 (1975).
3. F. A. Blum, D. W. Shaw, and W. C. Holton, *Appl. Phys. Lett.* **25**, 116 (1974).
4. J. C. Campbell, F. A. Blum, and D. W. Shaw, *Appl. Phys. Lett.* **26**, 640 (1975).
5. J. C. Campbell, F. A. Blum, D. W. Shaw, and K. L. Lamley, *Appl. Phys. Lett.* **27**, 202 (1975).
6. S. Somekh, E. Garmire, A. Yariv, H. C. Garvin, and R. G. Hunsperger, *Appl. Phys. Lett.* **22**, 46 (1973).
7. R. G. Hunsperger, R. G. Wilson, and D. M. Jamba, *J. Appl. Phys.* **43**, 1318 (1972).
8. J. P. Donnelly, W. T. Lindley, and C. E. Hurwitz, *Appl. Phys. Lett.* **27**, 41 (1975).

9. E. A. J. Marcatili, *Bell Syst. Tech. J.* 53, 645 (1974).
10. Solid State Research Report, Lincoln Laboratory, M.I.T. (1969:1), p. 3, DDC AD-687100.
11. A. G. Foyt, J. P. Donnelly, and W. T. Lindley, *Appl. Phys. Lett.* 14, 372 (1969), DDC AD-699465.
12. Solid State Research Report, Lincoln Laboratory, M.I.T. (1975:1), p. 8, DDC AD-A009848/3.
13. *Ibid.* (1975:2), p. 4, DDC AD-A013103/7.
14. J. S. Harris, F. H. Eisen, B. Welch, J. D. Haskell, R. D. Pashly, and J. W. Mayer, *Appl. Phys. Lett.* 21, 601 (1972).
15. F. H. Eisen, J. S. Harris, B. Welch, R. D. Pashly, D. Sigurd, and J. W. Mayer, Proceedings of the Conference on Ion Implantation in Semiconductors and Other Materials, Yorktown Heights, 1973 (Plenum Press, New York, 1973), p. 631.
16. D. E. Davies, S. Roosild, and L. Lowe, *Solid-State Electron.* 18, 733 (1975).
17. J. M. Woodcock, J. M. Shannon, and D. J. Clark, *Solid-State Electron.* 18, 267 (1975).
18. J. Lindhard, M. Scharff, and H. Schiott, *Kgl. Danske Videnskab. Selskab, Mat. Fys. Medd.* 33, 1 (1963).
19. W. J. Johnson and J. F. Gibbons, Projected Range Statistics in Semiconductors, distributed by Stanford University Bookstore (1970).
20. L. J. van der Pauw, *Philips Res. Rep.* 13, 1 (1958).
21. S. H. Groves, K. W. Nill, and A. J. Strauss, *Appl. Phys. Lett.* 25, 331 (1974), DDC AD-A002773/0.
22. S. G. Parker, J. E. Pinnell, and R. E. Johnson, *J. Electron. Mater.* 3, 731 (1974).
23. A. J. Strauss, *J. Electron. Mater.* 2, 553 (1973), DDC AD-772220/0.
24. J. N. Walpole, A. R. Calawa, R. W. Ralston, T. C. Harman, and J. P. McVittie, *Appl. Phys. Lett.* 23, 620 (1973), DDC AD-774003/8.
25. R. W. Ralston, J. N. Walpole, A. R. Calawa, T. C. Harman, and J. P. McVittie, *J. Appl. Phys.* 45, 1323 (1974), DDC AD-A000503/3.
26. F. J. Leonberger, A. L. McWhorter, and T. C. Harman, *Appl. Phys. Lett.* 26, 704 (1975).
27. Solid State Research Report, Lincoln Laboratory, M.I.T. (1974:3), p. 9, DDC AD-A001595/8.
28. T. C. Harman and J. P. McVittie, *J. Electron. Mater.* 3, 843 (1974), DDC AD-A006315/6.
29. See, for example, J. Bloem, *Philips Res. Rep.* 11, 273 (1956).



II. QUANTUM ELECTRONICS

A. CW LASER ACTION IN ACENTRIC $\text{NdAl}_3(\text{BO}_3)_4$ AND $\text{KNdP}_4\text{O}_{12}$

We have obtained low-threshold, room-temperature, CW lasing in two new materials: $\text{NdAl}_3(\text{BO}_3)_4$ and $\text{KNdP}_4\text{O}_{12}$ (abbreviated as NAB and KNP). These compounds are the first high-Nd-concentration laser materials with acentric space groups. This lack of inversion symmetry may allow second-order nonlinear optical processes (e.g., second-harmonic generation) as well as linear electro-optical modulation to be carried out directly in the laser crystal. As in the case of $\text{NdP}_5\text{O}_{14}$ (NPP) (Refs. 1 to 3) and $\text{LiNdP}_4\text{O}_{12}$ (LNP) (Refs. 4 to 6), their high Nd concentrations allow operation of very small lasers, since efficient absorption of pump radiation occurs in short distances (50 to 100 μm) and the resulting optical gains can be quite large. In all these materials the Nd^{3+} ions are isolated from each other, so that there is far less concentration quenching of the fluorescence lifetime than in conventional hosts such as Nd:YAG. In addition, NAB and $\text{Nd}_x\text{Gd}_{1-x}\text{Al}_3(\text{BO}_3)_4$ have comparatively short radiative lifetimes, even at low Nd concentrations (as reported⁷ in an earlier study), as a result of the high degree of odd-parity admixture of the $4f^3$ and $4f^25d$ configurations by the local crystal field around the Nd^{3+} ion. In this investigation we have studied the room-temperature, CW lasing behavior in NAB and KNP, and we have also obtained data on spontaneous fluorescence in the $\text{Nd}_x\text{Gd}_{1-x}\text{Al}_3(\text{BO}_3)_4$ and $\text{KNd}_x\text{Gd}_{1-x}\text{P}_4\text{O}_{12}$ systems for values of x down to 0.01.

Crystals of NAB were grown from a flux by slow cooling. The best crystals were obtained from a $\text{BaO}-\text{B}_2\text{O}_3$ or $\text{BaCO}_3-\text{B}_2\text{O}_3$ flux. In a typical run 15 g of BaO, 30 g of B_2O_3 , 16 g of Nd_2O_3 , and 15 g of Al_2O_3 were mixed in a 100- cm^3 Pt crucible. The mixture was fired at 1200°C for 4 hr to form a clear pink solution, cooled at 1°C/hr to 900°C, and then quenched. The crystals prepared by this technique are generally hexagonal rods about 1.5 mm long and 0.3 mm in diameter, with smooth faceted sides. They are higher in optical quality than those obtained previously by growth from a $\text{PbF}_2-\text{B}_2\text{O}_3$ flux.⁷ The NAB structure⁷ is rhombohedral with space group R32 and cell parameters $a = 9.3416(6)$ Å, $c = 7.3066(8)$ Å. The Nd site is in a trigonal prism of six O near-neighbors, with point symmetry group 32. The Nd concentration in NAB is 5.43×10^{21} cm^{-3} , 40 percent higher than in NPP.

Crystals of KNP were grown by a similar method, using Nd_2O_3 with a large excess of K_2CO_3 and $\text{NH}_4\text{H}_2\text{PO}_4$ as a flux. Typically, a mixture of these materials in a molar ratio of 1:3:12 (6.7, 8.3, and 27.6 g, respectively) was placed in a 100- cm^3 Au crucible, preheated at 200°C for 4 hr, and fired at 900°C overnight. The temperature was then reduced at 2°C/hr to 700°C, and the furnace power was turned off. The crystals obtained by this procedure are typically rectangular- or hexagonal-faced platelets 0.05 to 0.3 mm thick and 0.5×0.5 mm^2 in area. The crystal structure, determined by x-ray diffraction, is monoclinic with space group $\text{P}2_1$ and cell parameters $a = 7.266(1)$ Å, $b = 8.436(1)$ Å, $c = 8.007(1)$ Å, and $\beta = 91.97(1)^\circ$. The Nd^{3+} ions are located in distorted dodecahedra of the eight nearest O neighbors, slightly deviated from point symmetry group 2. The KNP lattice resembles that of NPP (Refs. 8 and 9) in that both are pseudo-orthorhombic and have staggered chain-like structures of the PO_4 groups. The deviation from orthorhombic symmetry is larger in KNP, consistent with its higher monoclinic-orthorhombic transition temperature of 167°C (determined by differential thermal analysis), compared with 146°C for NPP (Ref. 10). The Nd concentration in KNP is 4.08×10^{21} cm^{-3} . Yamada, Otsuka, and Nakano¹¹ have mentioned preparation of sintered ceramic KNP, but did not report its structure or details of its fluorescence properties.

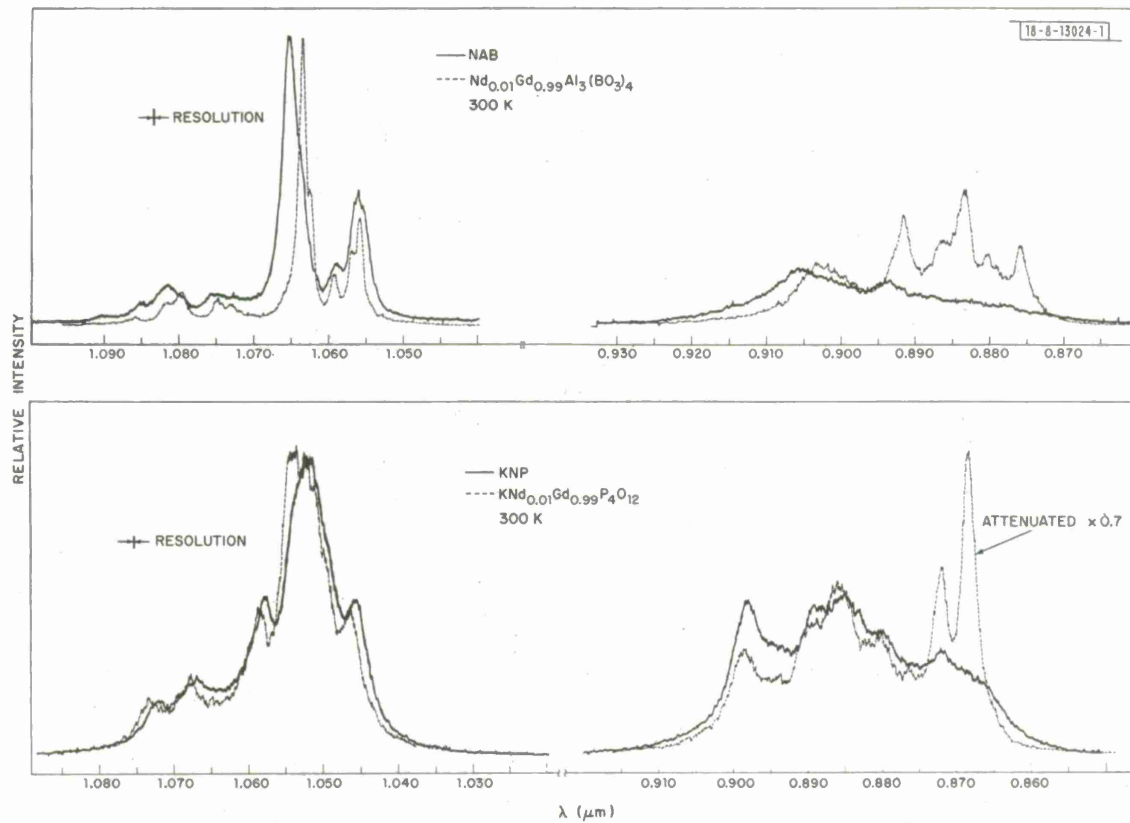


Fig. II-1. Room-temperature fluorescence spectra of ${}^4\text{F}_{3/2} - {}^4\text{I}_{11/2}$ and ${}^4\text{F}_{3/2} - {}^4\text{I}_{9/2}$ transitions in NAB, $\text{Nd}_{0.01}\text{Gd}_{0.99}\text{Al}_3(\text{BO}_3)_4$, KNP, and $\text{KNd}_{0.01}\text{Gd}_{0.99}\text{P}_4\text{O}_{12}$ (uncorrected for system response).

Fluorescence from $\text{Nd}_x\text{Gd}_{1-x}\text{Al}_3(\text{BO}_3)_4$ and $\text{KNd}_x\text{Gd}_{1-x}\text{P}_4\text{O}_{12}$ was excited by a pulsed optical parametric oscillator tuned to the $0.8\text{-}\mu\text{m}$ Nd^{+3} absorption band. The fluorescence spectra were analyzed by a double-grating monochromator and detected by a $\text{Ga}_{1-x}\text{In}_x\text{As}$ -cathode photomultiplier tube. The photomultiplier signal was amplified and then fed into one of the two boxcar amplifiers in a ratiometer system, with a portion of the pump pulse providing a reference signal to the other boxcar. This same system was also used to measure fluorescence lifetimes, by scanning the gate of the signal boxcar. The lifetime measurements were made with as weak excitation as possible, since strong excitation ($\sim 10^6 \text{ W/cm}^2$) gave very nonexponential decay, as previously reported for NPP (Ref. 12).

Room-temperature fluorescence spectra of the ${}^4\text{F}_{3/2}\text{-}{}^4\text{I}_{11/2}$ and ${}^4\text{F}_{3/2}\text{-}{}^4\text{I}_{9/2}$ transitions in NAB, $\text{Nd}_{0.01}\text{Gd}_{0.99}\text{Al}_3(\text{BO}_3)_4$, KNP, and $\text{KNd}_{0.01}\text{Gd}_{0.99}\text{P}_4\text{O}_{12}$ are shown in Fig. II-1. The ${}^4\text{I}_{11/2}$ and ${}^4\text{I}_{9/2}$ spectra for each sample were both taken under the same conditions, without being corrected for the difference in measuring system response between 1.05 and $0.9 \mu\text{m}$. In concentrated Nd materials, reabsorption from the ground-state levels of the ${}^4\text{I}_{9/2}$ manifold distorts and reduces the apparent emission cross sections. In order to clarify the energy levels, spectra were also taken at low temperature. These spectra show much narrower, well-resolved transitions. Except for reduced ${}^4\text{I}_{9/2}$ reabsorption, the room-temperature spectrum of the much less concentrated $\text{KNd}_{0.01}\text{Gd}_{0.99}\text{P}_4\text{O}_{12}$ is essentially the same as the KNP spectrum. As also observed by Weber,¹³ the room-temperature spectrum of $\text{Nd}_{0.01}\text{Gd}_{0.99}\text{Al}_3(\text{BO}_3)_4$ exhibits some narrowing and shifting relative to the NAB spectrum, but the borate system may be complicated by strains or distortions arising from a slightly different crystallographic phase.

The room-temperature ${}^4\text{F}_{3/2}\text{-}{}^4\text{I}_{11/2}$ fluorescence of NAB is dominated by a line at $1.065 \mu\text{m}$ that is 25 to 30 \AA wide. The low-temperature spectra show that this line has only one major component. In contrast, the KNP spectrum at room temperature has a dominant line at $1.051 \mu\text{m}$, over 50 \AA wide, that is made up of four components. From preliminary analysis of low-temperature spectra, the ${}^4\text{F}_{3/2}$ splitting is 70 cm^{-1} in NAB (Ref. 14) and 54 cm^{-1} in KNP.

The room-temperature fluorescence lifetimes for the ${}^4\text{F}_{3/2}$ transitions in $\text{Nd}_x\text{Gd}_{1-x}\text{Al}_3(\text{BO}_3)_4$ and $\text{KNd}_x\text{Gd}_{1-x}\text{P}_4\text{O}_{12}$ are plotted as a function of x in Fig. II-2. (Also included are earlier data⁷ for powdered samples in the borate system.) From these and other data of this type reported for $\text{Nd}_x\text{La}_{1-x}\text{P}_5\text{O}_{14}$ (Refs. 15-17), $\text{Na}_5\text{Nd}_x\text{Gd}_{1-x}(\text{WO}_4)_4$ (Ref. 15), and $\text{LiNd}_x(\text{Y, La, Gd})_{1-x}\text{P}_4\text{O}_{12}$ (Refs. 6, 18), the limiting lifetime (τ_0) observed at low Nd concentrations appears to have a close relationship to the symmetry of the Nd site. The least symmetric structure is that of NAB, in which the inverse position of any near-neighbor O atom is far removed from any other O near-neighbor. This lack of site inversion symmetry enables the odd-parity crystal field components to mix the opposite parity $4f^3$ and $4f^25d$ electronic configurations of Nd^{3+} , making the ${}^4\text{F}_{3/2}\text{-}{}^4\text{I}_{11/2}$ electric dipole transitions within the predominantly $4f^3$ configuration much more allowed.¹⁹ Thus, the comparatively short $\tau_0 = 50 \mu\text{sec}$ measured for $\text{Nd}_{0.01}\text{Gd}_{0.99}\text{Al}_3(\text{BO}_3)_4$ probably does not result from poor crystal quality or intrinsic nonradiative competitive processes, but instead indicates a high radiative transition probability and emission cross section. An example at the opposite extreme is given by the centro-symmetric $\text{Cs}_2\text{NaNdCl}_6$, which has a lifetime of 1.23 msec (Ref. 20) because the pure electric dipole ${}^4\text{F}_{3/2}\text{-}{}^4\text{I}_{11/2}$ transitions are completely forbidden and must be phonon assisted. For the Nd site in KNP, which is considerably less acentric than that in NAB, $\tau_0 = 275 \mu\text{sec}$. This value is comparable to those for the NPP and LNP structures, which have similar Nd coordinations.

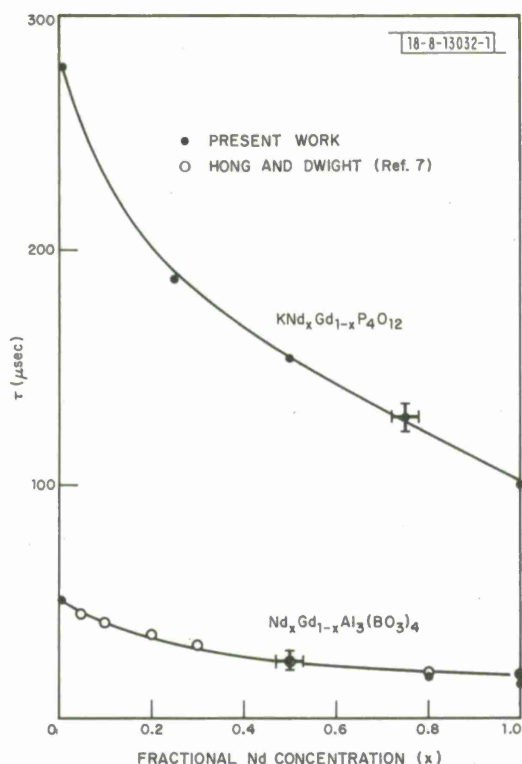


Fig. II-2. Fluorescence lifetime of the ${}^4F_{3/2}$ level in $\text{Nd}_x\text{Gd}_{1-x}\text{Al}_3(\text{BO}_3)_4$ and $\text{KNd}_x\text{Gd}_{1-x}\text{P}_4\text{O}_{12}$ as a function of x .

It is remarkable that in the series of concentrated-Nd materials [$\text{NdP}_5\text{O}_{14}$ (Ref. 16), $\text{LiNdP}_4\text{O}_{12}$ (Ref. 18), KNP, NAB, and $\text{NdNa}_5(\text{WO}_4)_4$ (Ref. 15)] in which the Nd^{3+} ions are separated by complexes such as PO_4 , BO_3 , or WO_4 , the degree of concentration quenching is similar. Specifically, the values of the quenching ratio τ_0/τ_1 (where τ_1 is the lifetime for $x = 1$) are all between 2.5 and 3.3. Thus, if the total fluorescence decay rate (the inverse of the measured lifetime) can be characterized as the sum of radiative and nonradiative (quenching) rates, then the quenching rate at $x = 1$ [$(1/\tau_1) - (1/\tau_0)$] is proportional to the predominantly radiative decay rate $1/\tau_0$. The dominant quenching process is probably cross-relaxation of excited and ground-state Nd^{3+} ions via the ${}^4I_{13/2}$ and ${}^4I_{15/2}$ levels.¹⁶ Energy migration followed by impurity quenching is less likely in these concentrated-Nd materials, which are probably purer than doped materials like Nd:YAG (Ref. 12). A third process, Auger cross-relaxation¹² of nearby excited ions is observed only at high excitation levels, not the low-excitation regime presently considered. In addition, the observed dependence of τ on x shows that the quenching rate is roughly proportional to concentration (for $x \gtrsim 0.1$), rather than to the square of the concentration, as expected for dipole-dipole interactions.^{16,21-23} Other higher-order multipolar interaction mechanisms which could cause cross-relaxation would vary as still larger powers of the concentration.

The proportionality of the quenching rate to both $1/\tau_0$ and concentration is consistent with the hypothesis of quenching via superexchange interactions. Superexchange of 4f electrons would be weak, but would increase with admixture of the $4f^25d$ configuration with $4f^3$, which also shortens τ_0 . The average quenching rate would also be proportional to the superexchange-connected near-neighbor Nd occupation probability, which varies linearly with concentration.

Superexchange has been reported to be significant in EPR measurements of energy transport between rare-earth ions in various halides.²⁴

To achieve room-temperature, CW lasing, pump radiation from a CW dye laser, tuned to strong Nd³⁺ absorptions near 0.58 μm , was used to excite a crystal of NAB or KNP placed in the center of a nearly concentric optical cavity having 5-cm-radius mirrors spaced approximately 10 cm apart. The pump beam was focused through one mirror (with high reflectivity at 1.06 μm) onto the sample, so as to be collinear with the laser mode. Although completely continuous lasing was achieved with all samples, in order to minimize heating effects the data reported here were taken with the pump radiation chopped at 150 Hz with a 10- to 20-percent duty cycle. All power measurements were made with calibrated Si photodiodes. Further details of the experimental apparatus and sample mounting are given in Refs. 3 and 5.

The laser samples of NAB were as-grown hexagonal rods whose side faces were the lasing facets, with the c-axis perpendicular to the lasing mode. The laser radiation was linearly polarized perpendicular to the c-axis. The samples ranged from 136 to 340 μm in length (i.e., the distance between the lasing facets, not the length of the rod), with threshold powers ranging from 0.55 to 1.9 mW when a 0.3-percent transmission output mirror was used. (Throughout this discussion, the measured threshold values refer to the power absorbed by the sample.) The threshold generally increased with sample length (l), consistent with the theoretical variation in the resonant (self-absorption) contribution to the threshold power:

$$P_R = \frac{h\nu_p N_0 e^{-\Delta E/kT}}{b\tau} \frac{\pi}{2} (w_o^2 + w_p^2) l \quad (\text{II-1})$$

where

$$h\nu_p = \text{pump photon energy} = 3.39 \times 10^{-19} \text{ J}$$

$$N_0 = \text{Nd concentration} = 5.43 \times 10^{21} \text{ cm}^{-3}$$

$$\Delta E = \text{lower laser level energy} \approx 1950 \text{ cm}^{-1}$$

$$w_o = \text{laser mode waist radius} \approx 9 \mu\text{m}$$

$$w_p = \text{pump mode waist radius} \approx 9 \mu\text{m}$$

$$b = \text{fractional population of upper laser level} \approx 0.59$$

$$\tau = \text{fluorescence lifetime} \approx 15 \mu\text{sec.}$$

This expression predicts a resonant threshold contribution of 0.005 mW per micrometer of sample length, in good agreement with the averaged measured value, $0.006 \pm 0.002 \text{ mW}/\mu\text{m}$, for a 0.3-percent output mirror.

The nonresonant contribution to the threshold is due to internal losses and output coupling:

$$P_{NR} = \frac{h\nu_p}{b\tau} \frac{L + \ln(1/R)}{4\sigma} \pi(w_o^2 + w_p^2) \quad (\text{II-2})$$

where L is the internal loss, R is the output mirror reflectivity, and σ is the fluorescence emission cross section. This contribution becomes more significant as R is decreased. From the relaxation oscillations of the laser output and the results obtained with low-output-transmission mirrors, we estimate that $L \leq 0.003$. From the threshold power of 4.3 mW measured for a sample 206 μm long with a 5.2-percent output mirror, and the value of $P_R = 1.0 \text{ mW}$ calculated for

this sample length, Eq. (II-2) gives $\sigma \sim 8 \times 10^{-19} \text{ cm}^2$. This value is considerably larger than that for NPP, $\sim 2 \times 10^{-19} \text{ cm}^2$ (Refs. 16, 17, and 25), consistent with the lower Nd symmetry and larger odd-parity admixture in NAB. Lasing has also been observed in crystals of $\text{Nd}_x\text{Gd}_{1-x}\text{Al}_3(\text{BO}_3)_4$ with x down to 0.5, giving estimated values of σ similar to those for NAB.

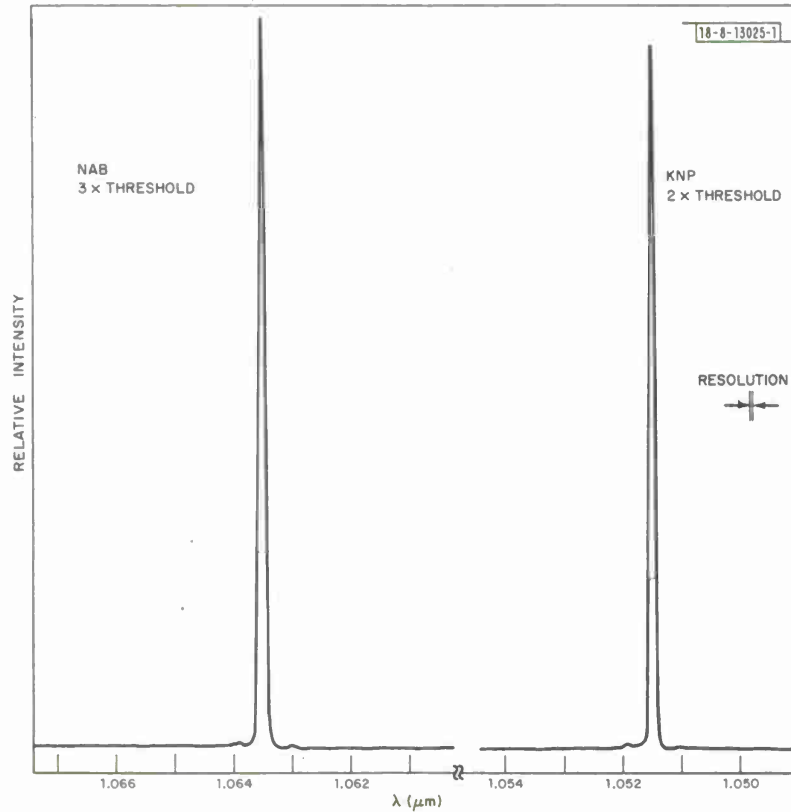


Fig. II-3. Room-temperature, quasi-CW lasing spectra of NAB and KNP.

The average measured slope efficiency (derivative of output power with respect to power absorbed) for the 206- μm sample was 22 percent, with up to 7-mW quasi-CW output power. There was only a slight variation in efficiency with output coupling, which is surprising in view of the low internal loss and the large variation in threshold with output coupling. A typical lasing spectrum, at three times threshold of ~ 1.2 mW (with 1.1-percent output transmission) is shown in Fig. II-3 for an NAB sample 136 μm long.

The laser samples of KNP were as-grown platelets whose broad faces were the lasing facets. Platelets with rectangular faces had their long axes parallel to the [010], b-axis, with [101] normal to the faces. Platelets with hexagonal faces, which were somewhat thicker, also had the [010] axis in the plane of the faces, but had $[\bar{1}01]$ normals. In both cases, the lasing polarization depended on the cavity alignment, although linear polarization roughly along [010] was generally easiest to obtain. Measurements of the indices and indicatrix have not yet been made. The lowest laser threshold was 0.45 mW, which was obtained for a sample 52 μm thick with 0.3-percent output mirror transmission. Even this thin sample absorbed 45 percent of the incident pump radiation.

The lasing cross section was estimated from data for a sample with $l = 187 \mu\text{m}$ by using Eqs. (II-1) and (II-2) with the parameters given above, except for the following: $N_0 = 4.08 \times 10^{21} \text{ cm}^{-3}$, $b = 0.56$, $\tau = 100 \mu\text{sec}$, $R = 0.011$, and $L \approx 0.004$. The value of L was determined from the slope efficiency of 25 percent obtained with the 0.3-percent output mirror. The threshold power was 0.932 mW, giving $\sigma \approx 1.5 \times 10^{-19} \text{ cm}^2$. This value of σ is only semiquantitative, since several transitions contribute to the lasing gain, with only the two dominant ones originating from the lower ${}^4F_{3/2}$ level. Also, no polarization dependence has been included. A lasing spectrum for this sample, at two times threshold, is shown in Fig. II-3. With a 1.1-percent output mirror, the slope efficiency was 35 percent, with 6.6-mW quasi-CW output.

S. R. Chinn
H. Y-P. Hong

B. PHOTOLUMINESCENCE OF BOUND EXCITONS IN TELLURIUM-DOPED CADMIUM SULFIDE†

Photoluminescence from crystals of cadmium sulfide doped with tellurium (CdS:Te) was examined. The luminescence observed was from the recombination of bound excitons captured at isoelectronic traps formed by Te impurities. Two types of traps were studied: One, with an associated broad emission band peaked at 600 nm (2.1 eV), was created by a single Te atom at an isolated impurity site (s-site); the other, with associated emission peaked at 730 nm (1.7 eV), was formed from a nearest-neighbor pair of Te impurities (p-site).

Platelet crystals were studied and had Te concentrations ranging from 10^{19} cm^{-3} to greater than 10^{20} cm^{-3} . Optical absorption coefficients for a number of samples were measured as a function of wavelength at temperatures of 20, 77, 187, and 300 K. Excitation spectra for both s- and p-site luminescence were determined for the same samples at the same temperatures cited above. Pulsed and CW lasers, including a flashlamp-pumped dye laser and a frequency-doubled Nd:YALO laser, were used to examine s- and p-site decay and emission spectra, including measurements at high excitation densities.

In analyzing data, the results found from measurements of both absorption coefficients and excitation spectra were used to characterize the processes by which luminescence was excited. For samples with a Te concentration of around 10^{19} cm^{-3} it is difficult to distinguish between various excitation processes. Analysis of low-temperature excitation spectra for samples with a Te concentration greater than 10^{20} cm^{-3} indicates the lineshape for absorption associated with the direct creation of s-site bound excitons. In addition, these spectra show that the cross section for capture of holes by the p-sites is about two orders of magnitude higher than that for hole capture by s-sites, and that the radiative quantum efficiency for p-site bound exciton recombination is roughly half that for recombination at s-sites. Absorption at long wavelengths in the most heavily doped samples is shown to be connected with the process which directly creates p-site bound excitons, and the lineshape for this process is extracted from absorption measurements. Possible theories for the observed bandedge absorption in CdS:Te are discussed.

Pulsed laser excitation of s-site luminescence at low levels indicates results comparable with previously published data. Effects on this luminescence of both bound-exciton ionization and excitation transfer to p-sites are discussed. Decay of luminescence from p-sites is

† This section is the abstract of a thesis carried out at Lincoln Laboratory and submitted to the Department of Electrical Engineering and Computer Sciences, M.I.T. in partial fulfillment of the requirements for the Degree of Doctor of Philosophy.

examined, and in the linear region appears to involve two distinct lifetimes of about 100 and 1000 nsec. The behavior of both s- and p-site luminescence at high excitation levels indicates the existence of an Auger type of interaction between bound excitons, in which the energy of one bound exciton is lost in dissociating or ionizing another bound exciton. Interactions become significant for s-site bound-exciton densities of 10^{17} cm^{-3} and for somewhat lower p-site densities, a fact which strongly reduces the possibility of achieving stimulated emission from either bound-exciton state.

P. F. Moulton

C. CW SECOND-HARMONIC GENERATION IN CdGeAs₂

A study is being made of the second-harmonic generation in CdGeAs₂ crystals when subjected to a CW beam of intense focused CO₂ laser radiation. The samples investigated to date were obtained from two boules (Nos. 74-32 and 76-5) which were found to have relatively low absorption at the doubled frequency. These samples, oriented for Type I phase matching, were placed in a liquid nitrogen Dewar to further reduce absorption. The samples varied in length from 4 to 13 mm, with varying cross-sectional areas, down to $1.5 \times 3 \text{ mm}$. The radius of the focused beam waist, as determined by calibrated aperture measurements, was approximately 90 μm .

The second-harmonic power generated in the initial experiments carried out using uncoated samples showed the expected $P(2\omega) \propto P(\omega)^2$ dependence, with no indication of saturation at the highest output levels available from the CO₂ laser. It was possible, however, to increase the effective power level available by overcoming the large reflective losses at the vacuum-CdGeAs₂ interfaces. This was done by evaporating a zinc sulfide coating on the front and rear surfaces of the samples to optimize transmission at wavelengths of 10.6 and 5.3 μm , respectively. By this means, the transmission at each face could be increased from 69 to 97 percent. The effect of antireflection (AR) coating upon second-harmonic generation is shown in Fig. II-4 where the

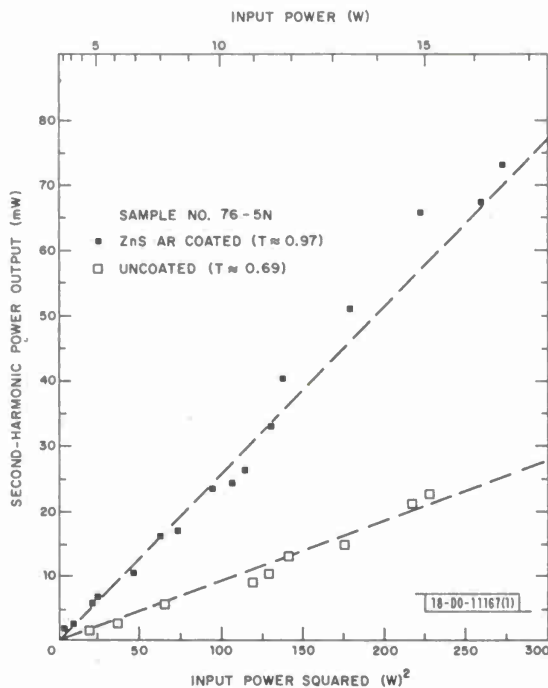


Fig. II-4. Second-harmonic power output of CdGeAs₂ at 5.3 μm as a function of incident 10.6- μm beam power before and after AR coating. Two dashed lines are related by ratio $(0.97/0.69)^3$.

second-harmonic power emerging from a CdGeAs₂ sample is given as a function of the CO₂ power incident upon the front surface. The two curves were taken with the same sample, before and after AR coating. The two dashed lines are related by the ratio (0.97/0.69)³. The figure shows no indication of saturation at the highest input levels, which correspond to intensities of the order of 2×10^5 W/cm². No signal degradation was observed while maintaining this level for several minutes. The results obtained indicate that CdGeAs₂, used in conjunction with a CO₂ laser, can achieve output levels at the doubled frequency which will permit long-range heterodyning experiments for air-pollution monitoring.

While most samples investigated withstood the input levels discussed above, the damage threshold of one sample was reached at 10^5 W/cm², and in another sample at about 1.5×10^5 W/cm². The damage was manifested by a sudden and total disappearance of second-harmonic generation, with no apparent signal degradation before the occurrence. After reaching the damage threshold, a fine ash deposit is observed on the Dewar window, and a hole of ~ 150 μ m diameter and ~ 1 mm depth is formed on the front face of the sample, with indications of surface melting. The back surface of the sample remains undamaged. These results are in contrast with the pit and plasma formation observed in CdGeAs₂ when subjected to high-energy pulsed input.²⁶ The CW damage appears to be consistent with the "thermal-runaway" mechanism which has been proposed to explain the damage in semiconductors used as high-power window materials.²⁷

N. Menyuk
G. W. Iseler

D. THIRD-HARMONIC GENERATION IN MOLECULAR GASES

Recent reports of CO₂ laser isotope separation in a number of molecular gases such as SF₆ and BCl₃ have indicated that these molecules can be excited to high vibrational states without collisions, which suggested to us that third-harmonic generation (THG) might be observed under similar conditions.^{28,29} Figures II-5(a) and (b) illustrate two different approaches to THG, each of which we have demonstrated experimentally. In process a, the molecule is chosen to have a fundamental vibrational transition near the pump frequency, and only vibrational intermediate states, each of which is near resonance, are involved.³⁰ In process b, a two-photon vibrational

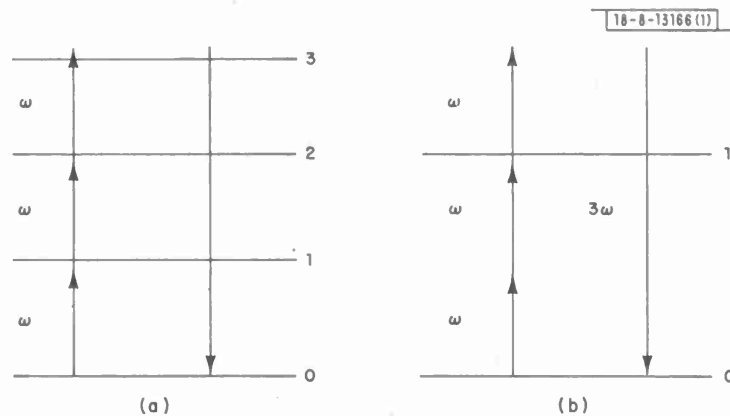


Fig. II-5. Schematic diagram of (a) triply resonant third-harmonic generation process, and (b) two-photon resonance THG process.

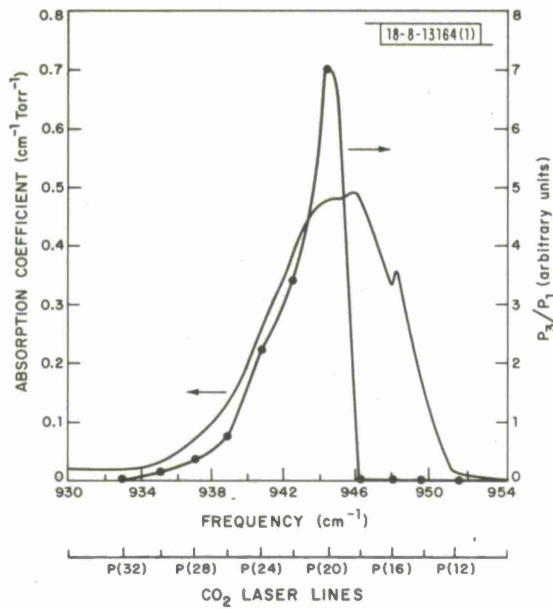


Fig. II-6. Frequency dependence of third-harmonic signal intensity along with measured absorption coefficient for SF₆. THG curve is for 5 Torr SF₆ with beam focused in center of cell.

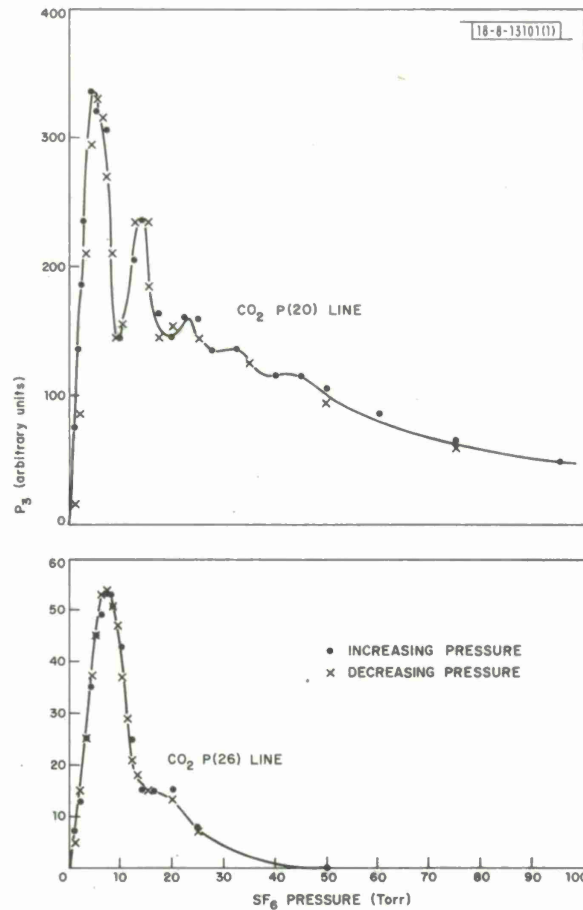


Fig. II-7. Pressure dependence of third-harmonic signal from SF₆ for excitation with P(20) and P(26) lines of 10.6- μ m CO₂ laser band.

resonance along with two electronic intermediate states is involved.³¹ THG by the triply resonant process (process a) was demonstrated in SF₆ and BCl₃, while the two-photon resonance (process b) was realized using CO.

A grating-controlled, single-line, multimode CO₂ TEA laser producing 0.75-J pulses with a width of 175 nsec (FWHM) was used in the experiments. The energy was measured using a Gen-Tec ED-200 Joule meter, and the intensity was monitored by a photon drag detector. The CO₂ laser beam was passed through an 8- μ m-long wavelength pass filter to block the 4.3- μ m fluorescence from the CO₂ laser as well as the third-harmonic signal generated in the CO₂ laser germanium output coupler, before being focused into a 10-cm-long, 1.8-cm-i.d. Teflon cell equipped with KCl windows. Except where indicated, the beam was focused by an $f/3$ off-axis paraboloid mirror to a spot size of 400 μ m, corresponding to a confocal parameter of 11 cm, at either 2.5 or 5 cm from the front of the cell. The CO₂ laser radiation emerging from the exit window of the cell was blocked by a LiF absorption filter, while the third-harmonic radiation was focused onto a 0.125-m focal length, $f/3.7$ monochromator equipped with a grating blazed at 4 μ m and then detected by an InSb photovoltaic detector. The detector had a time constant of 0.3 μ sec, which did not allow temporal resolution of the third-harmonic signal. The overall sensitivity of the detection system was calibrated using a 3.39- μ m He-Ne laser. The third-harmonic signal intensities and conversion efficiencies given below are based on this calibration, with no correction for the fact that the detector time constant was slower than third-harmonic risetime. The limited detector speed also prevented us from observing saturation phenomena which might occur in SF₆. The most extensive studies were performed on SF₆; frequent refillings of the cell were used to minimize depletion of the initial SF₆ fill due to dissociation of the gas by the focused CO₂ laser beam. Figure II-6 shows the normalized third-harmonic output as a function of frequency together with the absorption curve for SF₆. Note that the third-harmonic signal falls to zero on the high-frequency side of the CO₂ P(20) line. The pressure dependence of the THG was examined for each of the CO₂ P lines; Fig. II-7 shows the behavior for P(20) and P(26) with the focus 2.5 cm from the front of the cell. The oscillations in the third-harmonic signal that occur using the P(20) line become weaker and less pronounced as the laser frequency decreases. The oscillations also depend on the location of the focal plane within the cell; with the focus in the middle of the cell, only two maxima are observed in the output vs pressure curve for P(20).

The dependence of the TH signal P_3 on the pump power P_1 was measured for the P(20) line. At low intensities this dependence was close to P_1^3 , with a transition to P_1^2 behavior at higher intensities. Such deviations from a simple P_1^3 dependence have been observed with metal vapors and attributed to saturation of the two-photon transitions.^{32,33} In our case the deviations are probably due to saturations of the SF₆ absorption, with attendant changes in the third-order susceptibility and the wave vector mismatch. The third-harmonic power from an optimized SF₆ system pumped with 4.0 MW of CO₂ P(20) line power was approximately 2.2×10^{-5} W, corresponding to a conversion efficiency of 5×10^{-12} . THG in BCl₃ had a more complex frequency dependence; the existence of the ¹⁰B Cl₃ and ¹¹B Cl₃ isotopes resulted in two distinct spectral regions, near 940 and 980 cm⁻¹, in which THG was observed. In addition, multiple peaks were observed in each of these regions. In contrast to SF₆, no oscillations were found in the third-harmonic signal vs pressure curve for BCl₃.

THG according to process \underline{b} was obtained by using a two-photon resonance with the CO Q branch near 2143 cm^{-1} . Twice the CO_2 R(8) line frequency lies within 0.04 cm^{-1} of the CO Q(11) line. THG was observed using R(8) as well as R(10); no THG was found with R(12). In these experiments a 65-cm, $f/1$, ZnSe lens was used to focus the beam, which had an intensity of 2.5 MW for R(10), to a spot size of 1.8 mm in the center of a 1-m-long cell. THG was detectable ($\sim 2 \times 10^{-7}$ W) at pressures as low as 300 Torr. The third-harmonic signal for R(10) increases as pressure squared, while that for R(8) deviates from the square-law behavior at pressures above 500 Torr. At a CO pressure of 1 atm, the third-harmonic signal using the R(10) line was 1.1×10^{-6} W, corresponding to a conversion efficiency of 0.4×10^{-12} .

Calculations of the third-order susceptibility for both processes have been made. In the case of THG in CO, there is reasonable agreement between the observed and calculated conversion efficiencies. For SF_6 , saturation effects complicate the situation and the agreement is less satisfactory. A detailed discussion of the theory, as well as more experimental data, is being prepared for publication.

T. F. Deutsch
H. Kildal

E. ENERGY RELAXATION RATES IN LIQUID NITROGEN

Liquid systems offer an interesting potential as hosts for laser active molecules in the infrared. Higher densities and qualitatively different spectral distributions can be achieved in the liquid phase than in the gas phase. Molecular vibrational spectra tend to lose the rotational fine structure that is evident in the gas phase and appear as relatively broad (1 to 100 cm^{-1}) spectral features. This suggests the possibility of achieving tunability over a broader continuous wavelength range than would be available in the gas phase. (High-pressure CO_2 gas lasers are another approach toward this end.) Since the liquid phase infrared laser media possess a high density of molecules coupled with an extremely rapid rotational relaxation time, they are potentially useful for applications requiring high specific energy and short extraction times. These advantages will be discussed below in relation to the specific example of CO-doped liquid nitrogen.

Typical energy relaxation times for complex molecules in the liquid state are of the order of 10^{-12} sec (Ref. 34). These liquids are then very undesirable as laser hosts. However, Calaway and Ewing^{35,36} have recently measured the energy relaxation time in liquid nitrogen and find a time of ≥ 1 sec. We have remeasured this time using a different technique and find that the energy relaxation time in liquid nitrogen is ~ 70 sec and is limited mainly by radiative processes.

At high pressures and in its condensed phases there is an absorption band³⁷ of nitrogen around the vibration frequency of 2350 cm^{-1} due to collision-induced absorption. Figure II-8 shows the absorption spectra of a 5-cm path length of liquid nitrogen which has been doped with a CO density of $6.6 \times 10^{17} \text{ cm}^{-3}$ (this corresponds to approximately 40 parts per million of CO). We have made use of this induced absorption to optically pump the nitrogen vibrational band with an HBr laser, which has a number of lines within the broad N_2 band. The N_2 lifetime is then monitored by detecting the fluorescent decay from the CO molecules. After excitation, the vibrational manifolds of the N_2 and the CO equilibrate rapidly compared with the energy relaxation time (we have not yet measured this V-V time, but extrapolation from gas phase data³⁸ suggests a microsecond time scale for the V-V relaxation while the V-T time scale is 10^7 longer).

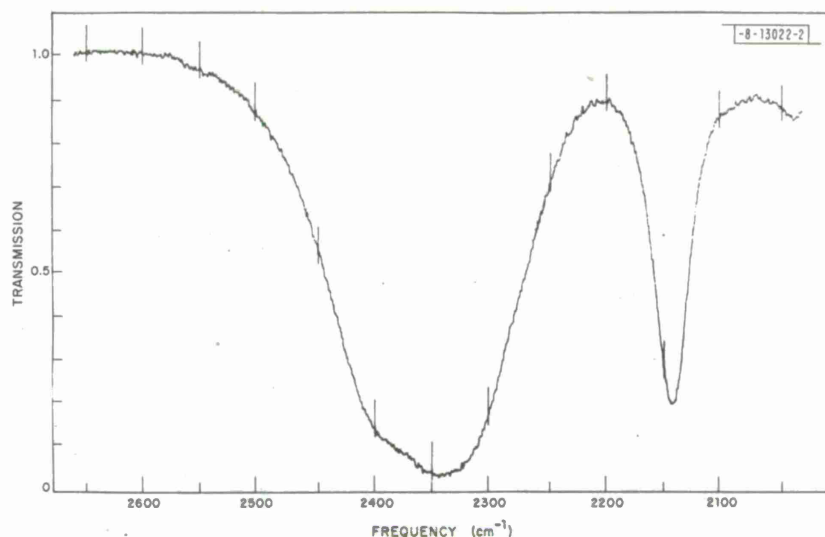


Fig. II-8. Infrared transmission of liquid nitrogen-CO mixture (CO concentration $6.6 \times 10^{17} \text{ cm}^{-3}$, path length 5 cm).

The energy then decays through both the N_2 and the CO. For the small signal regime, this decay is exponential and is characterized by a decay rate given by

$$\Gamma = \frac{\Gamma_{\text{N}_2} + \Gamma_{\text{CO}} \left(\frac{n_{\text{CO}}}{n_{\text{N}_2}} \right) e^{\beta \Delta \epsilon}}{1 + \left(\frac{n_{\text{CO}}}{n_{\text{N}_2}} \right) e^{\beta \Delta \epsilon}} \quad (\text{II-3})$$

where Γ_{N_2} and Γ_{CO} are the decay rates for N_2 and CO molecules, n_{CO} and n_{N_2} are the respective densities, $\beta = (1/kT) \approx (1/50) \text{ cm}$, and $\Delta \epsilon (185 \text{ cm}^{-1})$ is the energy difference between vibrational modes of the N_2 and CO molecules. This exponential factor appears because of the tendency of the molecular excitation to "fall downhill" into the lower-energy vibration. Figure II-9 shows the measured decay rates as a function of CO concentration. The intercept at zero CO concentration of $0.015 \pm 0.005 \text{ sec}^{-1}$ gives the intrinsic N_2 decay rate which agrees with the radiative decay rate calculated from the absorption band of Fig. II-8. Also shown in Fig. II-9 is the limiting decay rate determined by radiative decay of the CO [the radiative lifetime of CO in the liquid phase is 22 msec (Ref. 39)]. The experimental points are in reasonable agreement with this calculated decay rate, indicating that the decay processes are primarily radiative. At the highest CO concentration measured, the decay rate is below the calculated radiative limit due to the effects of radiation trapping in the (optically dense) CO fundamental.

This system of CO in liquid nitrogen is very promising as an infrared laser medium. There are excellent energy storage capabilities in the nitrogen at a density of $1.7 \times 10^{22} \text{ cm}^{-3}$ and an energy relaxation time of approximately 70 sec. Further, the V-V transfer time into the CO is fast, and thus, if the system is pumped above the threshold for laser oscillation, a short high-energy pulse ($\sim 100 \text{ nsec}$) is feasible. The CO band in the liquid nitrogen is 28 cm^{-1} wide, a

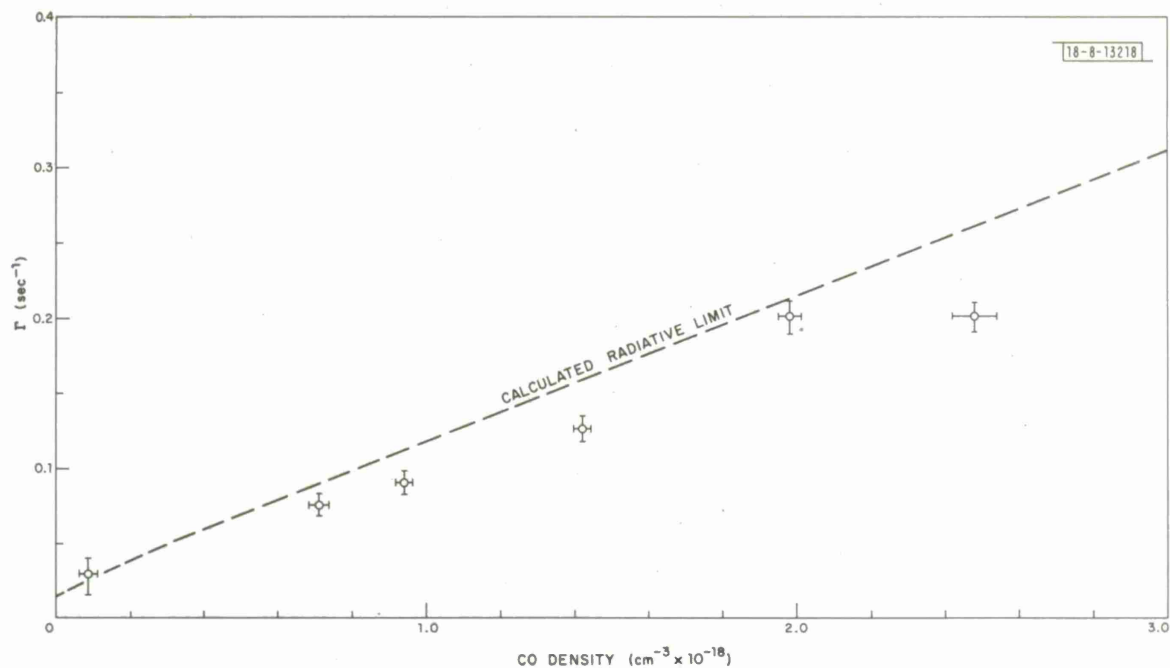


Fig. II-9. Measured decay rates of liquid N_2 -CO mixtures.

value comparable to the CO anharmonicity; thus, transitions between higher-lying levels will add to the frequency coverage.

S. R. J. Brueck
R. M. Osgood, Jr.

F. HIGH-RESOLUTION SUBMILLIMETER-WAVE SPECTROSCOPY USING NON-COLLINEAR, DIFFERENCE-FREQUENCY MIXING OF CO_2 LASER RADIATION

Recently, a new CW submillimeter source has been demonstrated which uses non-collinear phase matching of CO_2 laser radiation in GaAs (Ref. 40). Because of the numerous combinations of CO_2 laser lines available, this source is potentially useful for high-resolution spectroscopic studies. It combines the advantages of highly monochromatic radiation, typical of laser sources, with the additional advantage of step-tunability over a wide range of frequencies. The present study evaluates the viability of the existing system, which has an average power output of 10^{-8} W and a mean separation between lines of 0.07 cm^{-1} , for the investigation of rotational molecular spectra at high resolution.

The water-vapor absorption spectrum is of particular importance since it is the dominant mechanism for submillimeter attenuation in the atmosphere. Although it has been extensively studied over the last 20 years with systems of ever-increasing resolution,⁴¹⁻⁴⁵ many of the experiments have all been rather limited in their choice of wavelengths. In the case of difference-frequency generation, considerable frequency latitude is available, permitting the selection of well-isolated, optimal lines for investigation. After evaluating the individual water lines with regard to their overlap and to their proximity to strong submillimeter lines, two frequency ranges were chosen for the present experiment.⁴⁶ The first range includes the doublet at

55.405 cm^{-1} ($2_{12}-2_{21}$ transition) and 55.702 cm^{-1} ($1_{01}-2_{12}$), while the second region of interest is at 62.301 cm^{-1} ($5_{23}-5_{32}$). In the first case, the coincidence of several source lines near and between the doublet should give a qualitative measure of resolution, while in the second case, two isolated source lines on either side of the transition should yield a more quantitative indication of resolution.

The experimental source configuration was similar to that of Ref. 40 except for the addition of motor controls to facilitate tuning the CO_2 lasers. Measurements were made through matched transmission and reference cells using a pumped helium-cooled bolometer as a detector. In order to obtain spectroscopic information from our absorption measurements, the technique of pressure broadening⁴⁷ was used. By observing the effects of increasing pressure (or the introduction of a foreign gas) on the transmission at a single frequency, the line parameters for a given model can be extracted. Figure II-10 shows the general features of a typical plot of absorption vs pressure squared for the doublet. It clearly shows that the slopes, which vary inversely as the separation from line center, are very large at 55.39235 cm^{-1} (near line center) and are getting smaller as one moves farther out onto the Lorentzian tails. For the transition at 62.3 cm^{-1} , some of the reduced data is shown in Table II-1. Even with this rather preliminary approach, the results are comparable to, or better than, the best obtainable with Fourier transform interferometers.

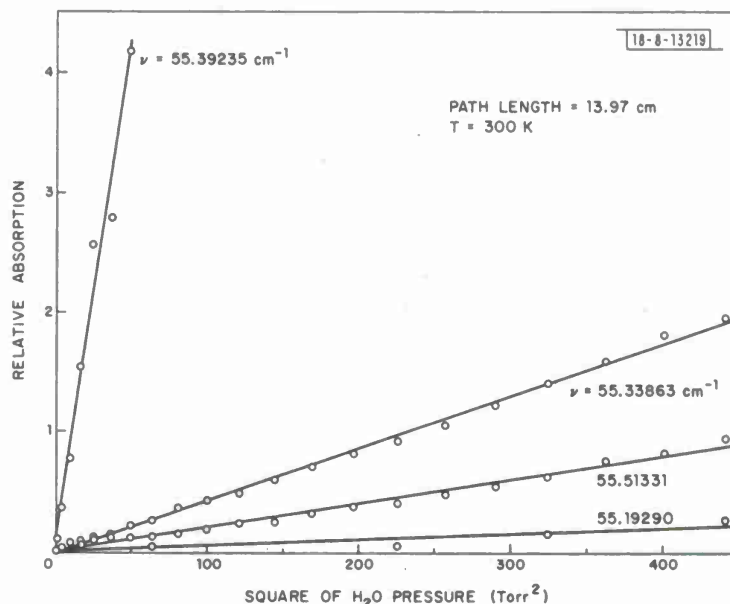


Fig. II-10. Self-broadening data and best-fit straight lines in 55- to 56- cm^{-1} wavelength region. Water-vapor absorption lines are at 55.405 and 55.702 cm^{-1} .

TABLE II-1
COMPARISON OF LINE PARAMETERS FOR THE 62.3-cm⁻¹ H₂O TRANSITION

	Source Frequency ν_0 (cm ⁻¹)	Line Intensity S (gm ⁻¹ cm)	Self-Broadened Halfwidth Parameter α_0 (cm ⁻¹ /atm)	N ₂ -Broadened Halfwidth Parameter α_{N_2} (cm ⁻¹ /atm)	Ratio α_0/α_{N_2}
Present experiment	62.302 ± 0.001	5300 ± 1900	0.413 ± 0.015	0.063 ± 0.007	6.6
Möller and Rothschild ⁴¹	62.30	—	—	—	—
Hall and Dowling ⁴²	62.301	—	—	—	—
AFCRL ⁴³	62.301	5210	—	0.088	—
Yunker and Querfeld ⁴⁴	62.29	—	—	—	—
Benedict and Kaplan ⁴⁵	—	—	0.4726	0.0909	~5.5

A number of technical improvements, especially with the design of the cells and with the spectral purity of the CO₂ lasers, will greatly increase the system's capability. Our results indicate that at least one and probably two orders of magnitude improvement in resolution can be obtained. In addition, the use of a high-pressure capillary CO₂ laser as one of the input frequencies could produce an almost continuously tunable source for submillimeter and far-IR spectroscopy.

P. D. Mandel[†]
H. R. Fetterman
R. L. Aggarwal[‡]

[†] Also Department of Physics, M.I.T.

[‡] Francis Bitter National Magnet Laboratory, M.I.T.

REFERENCES

1. H. P. Weber, T. C. Damen, H. G. Danielmeyer, and B. C. Tofield, *Appl. Phys. Lett.* **22**, 534 (1973).
2. H. G. Danielmeyer, G. Huber, W. W. Krühler, and J. P. Jeser, *Appl. Phys.* **2**, 335 (1973).
3. S. R. Chinn, J. W. Pierce, and H. Heckscher, *IEEE J. Quantum Electron.* **QE-11**, 747 (1975).
4. K. Otsuka and T. Yamada, *Appl. Phys. Lett.* **26**, 311 (1975).
5. S. R. Chinn and H. Y-P. Hong, *Appl. Phys. Lett.* **26**, 649 (1975).
6. K. Otsuka, T. Yamada, M. Saruwatari, and T. Kimura, *IEEE J. Quantum Electron.* **QE-11**, 330 (1975).
7. H. Y-P. Hong and K. Dwight, *Mater. Res. Bull.* **9**, 1661 (1974), DDC AD-A006704/1.
8. H. Y-P. Hong, *Acta Crystallogr.* **B30**, Part 2, 468 (1974), DDC AD-A000491/1.
9. K. R. Albrand, R. Attig, J. Fonner, J. P. Jeser, and D. Mootz, *Mater. Res. Bull.* **9**, 129 (1974).
10. H. P. Weber, B. C. Tofield, and P. F. Liao, *Phys. Rev. B* **11**, 1152 (1975).
11. T. Yamada, K. Otsuka, and J. Nakano, *J. Appl. Phys.* **45**, 5096 (1974).
12. M. Blätte, H. G. Danielmeyer, and R. Ulrich, *Appl. Phys.* **1**, 275 (1973).
13. H. P. Weber, *Optoelectronics* (to be published).
14. H. G. Danielmeyer, H. Y-P. Hong, and S. R. Chinn (unpublished).
15. H. Y-P. Hong and K. Dwight, *Mater. Res. Bull.* **9**, 775 (1974), DDC AD-786294/9.
16. S. Singh, D. C. Miller, J. R. Potopowicz, and L. K. Shick, *J. Appl. Phys.* **46**, 1191 (1975).
17. H. P. Weber, P. F. Liao, and B. C. Tofield, *IEEE J. Quantum Electron.* **QE-10**, 563 (1974).
18. K. Dwight, private communication.
19. See, for example, G. Dieke, *Spectra and Energy Levels of Rare Earth Ions in Crystals* (Interscience, New York, 1968), Chap. 9.
20. B. C. Tofield and H. P. Weber, *Phys. Rev. B* **10**, 4560 (1974).
21. D. L. Dexter, *J. Chem. Phys.* **21**, 836 (1953).
22. L. G. Van Uitert and L. F. Johnson, *J. Chem. Phys.* **44**, 3514 (1966).
23. H. G. Danielmeyer, M. Blätte, and P. Balmer, *Appl. Phys.* **1**, 269 (1973).
24. R. J. Birgeneau, *Appl. Phys. Lett.* **13**, 193 (1968); J. D. Riley, J. M. Baker, and R. J. Birgeneau, *Proc. Roy. Soc. London A* **320**, 369 (1970).
25. G. Huber, W. W. Krühler, W. Bludau, and H. G. Danielmeyer, *J. Appl. Phys.* (to be published).
26. Solid State Research Report, Lincoln Laboratory, M.I.T. (1975:2), pp. 25-29, DDC AD-A013103/7.
27. F. A. Horrigan, C. A. Klein, R. J. Rudke, and D. T. Wilson, "High Power Gas Laser Research," Final Technical Report on Contract No. DA-AH01-67-1589, Raytheon Research Division (September 1968), pp. 59-64.
28. R. V. Ambartzumian, Y. A. Gorokhov, V. S. Letokhov, and G. M. Markarov, *Zh. Eksp. Teor. Fiz. Pis'ma Red.* **21**, 375 (1975).
29. J. L. Lyman, R. J. Jensen, J. Rink, C. P. Robinson, and S. D. Rockwood, *Appl. Phys. Lett.* **27**, 87 (1975).

30. Y. Ueda and K. Shimoda, *J. Phys. Soc. Japan* 28, 196 (1970).
31. C. Y. She and K. W. Billman, *Appl. Phys. Lett.* 27, 76 (1975).
32. C. C. Wang and L. I. Davis, Jr., *Phys. Rev. Lett.* 35, 650 (1975).
33. J. F. Ward and A. V. Smith, *Phys. Rev. Lett.* 35, 653 (1975).
34. A. Laubereau, D. von der Linde, and W. Kaiser, *Phys. Rev. Lett.* 28, 1162 (1972).
35. W. F. Calaway and G. E. Ewing, *Chem. Phys. Lett.* 30, 485 (1975).
36. W. F. Calaway and G. E. Ewing, *J. Chem. Phys.* 63, 2842 (1975).
37. M. F. Crawford, H. L. Welsh, and J. L. Locke, *Phys. Rev.* 75, 1607 (1949).
38. D. F. Starr, J. K. Hancock, and W. H. Green, *J. Chem. Phys.* 61, 5421 (1974).
39. H. Vu, M. R. Atwood, and B. Vodur, *J. Chem. Phys.* 38, 2671 (1963).
40. R. L. Aggarwal, B. Lax, H. R. Fetterman, P. E. Tannenwald, and B. J. Clifton, *J. Appl. Phys.* 45, 3972 (1974).
41. K. D. Möller and W. G. Rothschild, *Far-Infrared Spectroscopy* (Wiley-Interscience, New York, 1971), p. 318.
42. R. T. Hall and J. M. Dowling, *J. Chem. Phys.* 47, 2454 (1967).
43. R. A. McClatchey, W. S. Benedict, S. A. Clough, D. E. Burch, R. F. Calfee, K. Fox, L. S. Rothman, and J. S. Garing, "AFCRL Atmospheric Absorption Line Parameters Compilation," Document No. AFCRL-TR-73-0096, Air Force Systems Command, USAF, L. G. Hanscom Field, Bedford, Mass. (January 1973).
44. W. Yunker and C. Querfeld, "Pure Rotational Spectrum of Water Vapor, 1. Table of Line Parameters," Document No. ERDA-2 U.S. Army Electronics Research and Development Activity, White Sands Missile Range, New Mexico (February 1963), DDC AD-298151.
45. W. S. Benedict and I. D. Kaplan, *J. Quant. Spectrosc. Radiat. Transfer* 4, 453 (1964).
46. P. D. Mandel, "High Resolution Submillimeter-Wave Spectroscopy Using Non-Collinear Mixing of Laser Radiation," M. S. Thesis, Department of Physics, M.I.T., (September 1975) (unpublished).
47. T. Shimizu, F. O. Shimizu, R. Turner, and T. Oka, *J. Chem. Phys.* 55, 2822 (1971).

III. MATERIALS RESEARCH

A. DOUBLE-HETEROSTRUCTURE GaInAsP/InP DIODE LASERS

Room-temperature operation of $\text{Ga}_{1-x}\text{In}_x\text{As}_{1-y}\text{P}_y/\text{InP}$ double-heterostructure (DH) diode lasers has been achieved. Broad-area devices emitting at $1.1\ \mu\text{m}$ have been fabricated from three-layer films grown by liquid-phase epitaxy (LPE) on InP substrates. Pulsed thresholds as low as $2.8\ \text{kA}/\text{cm}^2$ have been obtained for an active region thickness of about $0.5\ \mu\text{m}$. With thresholds in this range, it should be possible to produce stripe-geometry lasers capable of continuous operation at room temperature. Such CW lasers would be of particular interest for communication systems using optical fibers, which have their minimum transmission loss near $1.1\ \mu\text{m}$ (Ref. 1).

Three different active-layer/barrier-layer combinations have been used for DH diode lasers emitting at wavelengths near $1\ \mu\text{m}$: $\text{Ga}_{1-x}\text{In}_x\text{As}/\text{Ga}_{1-y}\text{In}_y\text{P}$ (Ref. 2), $\text{GaAs}_{1-x}\text{Sb}_x/\text{Ga}_{1-y}\text{Al}_y\text{As}_{1-x}\text{Sb}_x$ (Ref. 3), and $\text{Ga}_{1-x}\text{In}_x\text{As}_{1-y}\text{P}_y/\text{InP}$ (Ref. 4). Pulsed room-temperature operation has been reported for the first² and second³ combinations, in both of which the active layer is a ternary alloy between GaAs and a lower-bandgap III-V compound. Since GaAs differs significantly in lattice constant from both ternaries, in each case the barrier layers must be formed by another alloy whose composition can be adjusted to give the high degree of active/barrier lattice matching that is essential for efficient laser operation. Consequently, the compositions of three layers – the active region and both barriers – must be accurately controlled for optimum device performance. Furthermore, to obtain epitaxial layers of sufficiently high quality it is necessary to grow intermediate alloy layers with either continuous or step-wise composition grading on the GaAs substrates before deposition of the heterostructures. In preparing GaAsSb/GaAlAsSb lasers, for example, three GaAsSb layers of different compositions have been grown between the substrate and the first GaAlAsSb barrier.³

Operation of DH diode lasers utilizing GaInAsP alloys for emission near $1\ \mu\text{m}$ has previously been limited to 77 K (Ref. 4). However, these quaternary alloys offer several potential advantages because the presence of four components makes it possible to obtain the same lattice constant as that of InP over a range of compositions that give energy gaps corresponding to any wavelength between 0.92 and $1.7\ \mu\text{m}$ (Ref. 5). For $1.1\ \mu\text{m}$ or any other wavelength in this range, only the composition of the active region requires accurate control in order to achieve excellent (in principle, perfect) lattice matching to barrier layers of InP, whose composition is fixed because this compound has a narrow homogeneity region. The possibility of such accurate control has been demonstrated by the LPE growth of GaInAsP layers on InP for photoemissive devices⁶ as well as for diode lasers.⁴ Furthermore, the LPE growth procedure is simplified because the heterostructure layers can be grown directly on InP substrates, without the need for intermediate composition-graded alloy layers. In addition, the elimination of lattice mismatch from the entire device structure should cause a reduction in defects and strain, and therefore might result in longer operating lifetimes.

To prepare lasers emitting at $1.1\ \mu\text{m}$, successive layers of p-doped InP, undoped $\text{Ga}_{0.12}\text{In}_{0.88}\text{As}_{0.23}\text{P}_{0.77}$, and n-doped InP were grown on InP substrates in a horizontal sliding boat machined from high-purity graphite. The substrates were (111)-oriented wafers cut from a Zn-doped ingot ($p = 4 \times 10^{18}\ \text{cm}^{-3}$) grown from a stoichiometric melt by the horizontal gradient-freeze technique.⁷ The 111-B substrate surface was ground with $2\text{-}\mu\text{m}$ alumina and then

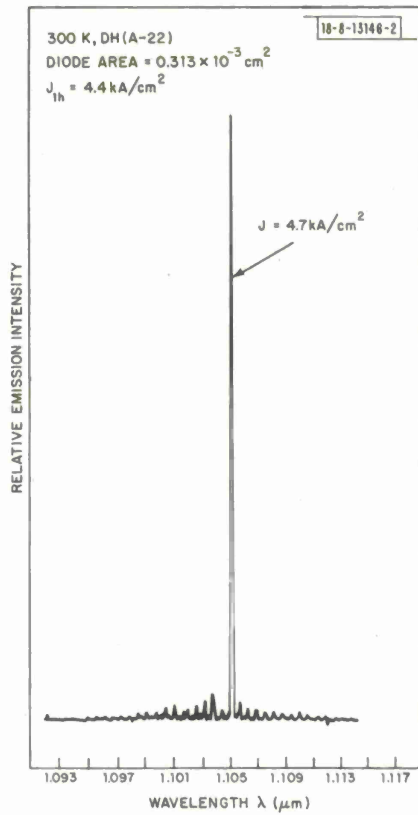


Fig. III-1. Room-temperature emission spectrum of pulsed GaInAsP/InP DH laser for drive current density about 10 percent above threshold.

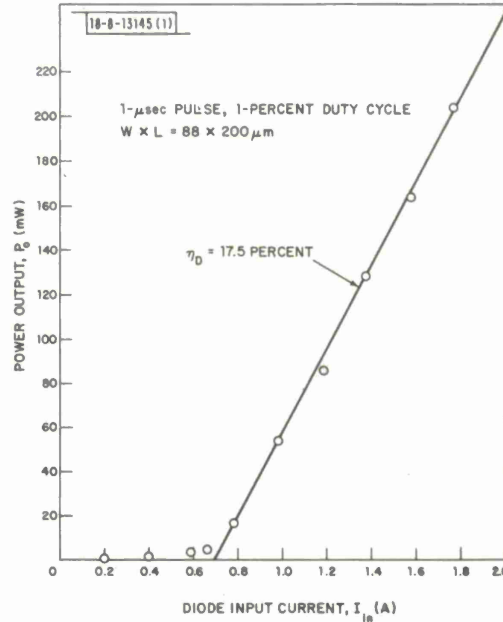


Fig. III-2. Room-temperature power output (P_o) of pulsed GaInAsP/InP DH laser vs input current (I_{in}).

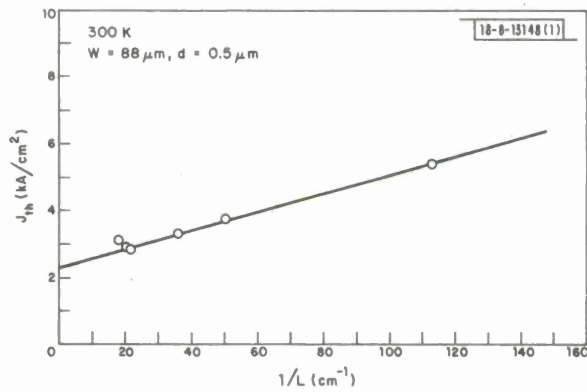


Fig. III-3. Threshold current (J_{th}) vs $1/L$, where L is cavity length, for pulsed GaInAsP/InP DH lasers.

chem-mech polished with Br-CH₃OH. All the LPE layers were grown at a cooling rate of 0.7°C/min. from In-rich solutions that were supercooled by 3° to 10°C below their saturation temperatures before placing them in contact with the substrate at temperatures near 635°C. As in the case of GaAs and GaAlAs (Ref. 8), the supercooling technique yields smooth, flat layers of uniform thickness. The growth solutions for the p- and n-type InP layers were doped with sufficient Zn and Sn, respectively, to give carrier concentrations of about $3 \times 10^{18} \text{ cm}^{-3}$ according to published distribution data.^{9,10} The p-type InP layers were ~5 μm thick, the n-type InP layers ~2 μm thick, and the GaInAsP layers from 0.2 to 2 μm thick. The active layers were too thin for accurate electron microprobe analysis. The composition of Ga_{0.12}In_{0.88}As_{0.23}P_{0.77} was found by analyzing somewhat thicker layers grown under the same experimental conditions. (Although in principle active layers could be grown directly on the InP substrate, this procedure would yield imperfect layers because some decomposition of the substrate occurs by preferential evaporation of P during the heating period before LPE growth. Better heterostructures are obtained by first depositing an InP layer and then immediately growing the GaInAsP layer before decomposition can occur.)

After being removed from the LPE growth furnace, the wafer was ground on the substrate side to reduce its overall thickness to about 100 μm. Contacts to the p- and n-type sides were made by evaporating Au/Zn and Au/Sn, respectively, and alloying at 350°C. The wafer was then sawed and cleaved to form diodes with Fabry-Perot cavities. A preliminary evaluation of the diodes was made by using an infrared microscope to examine their spontaneous emission under forward bias. The radiation observed from properly lattice-matched structures originates mainly from the active region, but the emission is very weak or undetectable from active regions with compositions that do not give the same lattice constant as InP.

Figure III-1 is the room-temperature spectrum of a DH diode with an active region about 0.6 μm thick, measured at a current density about 10 percent above the laser threshold (J_{th}). The radiation is concentrated almost entirely in a single peak at 1.105 μm. From the spacing of the cavity modes, which extend from 1.095 to 1.113 μm, the effective refractive index is found to be about 5.1. The photon energy at the peak is 1.12 eV, about 50 meV less than the energy gap given for Ga_{0.12}In_{0.88}As_{0.23}P_{0.77} by a published empirical relationship.⁵ Such differences are generally observed for diode lasers because most of the lasing transitions involve impurity levels.

As the thickness (d) of the active region is decreased below 2 μm, the value of J_{th} decreases linearly with d, reaches a minimum at about 0.5 μm, and then increases rapidly. The lowest value of J_{th} so far obtained is 2.8 kA/cm², which was measured for a diode with d = 0.6 μm and a cavity length (L) of 475 μm. In the linear region, the J_{th} values are about 70-percent higher than those reported¹¹ for GaAs/GaAlAs DH lasers with the same values of d. The value of J_{th} for a given GaInAsP/InP diode decreases by about a factor of 20 from 300 to 77 K.

The variation of the total output power (P_o) emitted from both faces of a typical diode is plotted against input current (I_{in}) in Fig. III-2. The diode was driven by 1-μsec pulses with a duty cycle of 1 percent, and the output was measured with a calibrated Si photodiode. The threshold current is about 0.7 A. Above threshold the differential external quantum efficiency is 17.5 percent, about one-third the values for state-of-the-art GaAs/GaAlAs DH lasers,¹¹ and the differential power efficiency is 9.5 percent. At 2 J_{th} , the total output power is 135 mW and the overall power efficiency is 4.9 percent.

For lasers with d = 0.5 μm and values of L between 90 and 500 μm, J_{th} is found to vary linearly with 1/L, as shown in Fig. III-3. From the relationship $J_{th} = (\alpha/\beta) + (1/L\beta) \ln(1/R)$,

where α is the loss, β is the gain, and $R \approx 0.29$ is the reflectivity of the active layer, the experimental data give $\alpha = 68 \text{ cm}^{-1}$ and $\beta = 30 \text{ cm} (\text{kA})^{-1}$. The differential internal quantum efficiency calculated from α and β is 37 percent, about half the value for GaAs/GaAlAs DH lasers.¹¹

In conclusion, the excellent properties of the DH GaInAsP/InP diode lasers even at this early stage of development, together with their structural simplicity and consequent ease of fabrication, make them promising devices for applications in optical communications and integrated optical circuits.

J. J. Hsieh S. R. Chinn
M. C. Finn J. A. Rossi

B. PHOTOELECTROLYSIS OF WATER

Detailed measurements have been made on the photoelectrolysis of water in cells with single-crystal n-type SrTiO₃ anodes.[†] By confirming our preliminary observation of photoelectrolysis with SrTiO₃ (Ref. 12), these measurements establish that TiO₂ is not unique in its ability to catalyze the decomposition of water. The quantum efficiencies measured with SrTiO₃ in the absence of a bias voltage are about an order of magnitude higher than those obtained with TiO₂. Because the energy gap of SrTiO₃ is 3.2 eV, this increase in quantum efficiency does not result in practical solar conversion efficiencies. The increase is significant, however, because it is correlated with a decrease in electron affinity. This correlation supports the energy-level model that we have proposed for photoelectrolysis,¹² and it confirms the conclusion that both electron affinity and energy gap must be considered in the search for improved electrode materials.

Photoelectrolysis cells were prepared by immersing an SrTiO₃ anode and a platinized-Pt cathode into an aqueous electrolyte contained in a fused-quartz vessel. Each electrode was capped with an inverted buret filled with electrolyte, so that the gas evolved could be collected by liquid displacement for volumetric measurement and chemical analysis. Provision was made for flushing the electrolyte with either N₂ or Ar in order to remove dissolved O₂. [If an appreciable concentration of dissolved O₂ is present, as is the case for water in equilibrium with air at atmospheric pressure, transfer of electrons from the cathode to the electrolyte takes place by reduction of O₂ rather than by discharge of H₂ (Ref. 12).] Measurements were generally made after the solution had been purged for several hours.

In order to determine what experimental conditions would yield the highest photoelectrolytic quantum efficiencies, differential space-charge capacitance and surface photovoltage techniques¹³ were used to measure the flat-band potential $(\phi_F)_{fb}$ for SrTiO₃, relative to a saturated calomel electrode, as a function of electrolyte pH. The results of these measurements indicated that the maximum band bending is obtained at pH values above ~13. [For the same pH, the $(\phi_F)_{fb}$ value for TiO₂ is about 0.2 eV less negative than the corresponding SrTiO₃ value.] To take advantage of the increased band bending at high pH, most of the photoelectrolysis experiments with SrTiO₃ were performed with strongly alkaline electrolyte solutions ($\geq 0.1 \text{ N KOH or NaOH}$). Incidentally, the solubilities of both O₂ and H₂ are reduced in such alkaline solutions, so that the evolution of H₂ bubbles at the cathode is readily observed even without O₂ purging.

To determine whether photoelectrolysis is the only chemical reaction that takes place when SrTiO₃ cells are illuminated, the gases evolved at the electrodes of a cell were collected and analyzed. The gas evolved at the cathode was identified as H₂ because it was completely absorbed by hot CuO, while that evolved at the anode was identified as O₂ because it was completely

[†] Preliminary experiments with an anode prepared by pressing powdered SrTiO₃ gave results similar to those obtained with single-crystal anodes.

absorbed by pyrogallol. At high pH values, where the accuracy of the measurements was highest because the amounts of gas were greatest, the volumes of gas collected at the cathode and anode were found to be over 90 percent of the values calculated from the integrated electric current by assuming that the only reactions were those of photoelectrolysis; the differences can be attributed to collection losses.

The external photoelectrolytic quantum efficiency (η_q) was measured as a function of photon energy ($h\nu$) by means of experiments in which the anode of a cell was illuminated by monochromatic light from a source consisting of a 1000-W Xe lamp and a grating monochromator. The light intensity (S) incident on the cell was determined by measuring the spectral power output of the monochromator with a thermopile power meter. The value of η_q , defined as 100 times the ratio of the number of electrons flowing in the external circuit to the number of photons incident on the cell, was determined from the measured current density (J) by using the expression

$$\eta_q = 100 \frac{J}{S} h\nu \quad (\text{III-1})$$

where J is given in A/cm^2 , S in W/cm^2 , and $h\nu$ in eV.

The variation of η_q with $h\nu$ is plotted in Fig. III-4 for a cell in which the anode and cathode were shorted together. The electrolyte was a 10N NaOH solution that had been thoroughly purged to remove dissolved O_2 . The threshold energy for photoelectrolysis is 3.2 eV, the value reported¹⁴ for the direct energy gap of SrTiO_3 . The value of η_q peaks in the region between 3.7 and 3.9 eV. The maximum value is 10 percent, about an order of magnitude greater than the highest values obtained for photoelectrolysis in cells with TiO_2 anodes in the absence of a bias voltage. This increase in η_q is due to the increased band bending of SrTiO_3 (about 0.2 eV for a cell without a bias voltage), which increases the fraction of photo-generated electron-hole pairs that are separated at the anode surface.

Even with the amount of band bending in SrTiO_3 , η_q is limited because most of the photo-generated pairs still recombine without contributing to photoelectrolysis. The efficiency of pair separation and therefore the value of η_q can be greatly increased by applying a bias voltage (V_b) to make ϵ_F (anode) more positive than ϵ_F (cathode), thus increasing the band bending. This effect is shown in Fig. III-5, where η_q for $h\nu = 3.8$ eV is plotted as a function of V_b . The value of η_q increases rapidly with increasing V_b , reaching about 80 percent for $V_b \gtrsim 1$ V. If reflection and absorption losses are taken into account, the highest η_q values correspond to internal quantum efficiencies approximating 100 percent. For the same photon energy, Fig. III-5 also shows the dependence on V_b of the power conversion efficiency (η_p) defined as 100 times the ratio of the power available in the collected H_2 to the total of incident optical power (P_{opt}) and electrical power applied:

$$\eta_p = 100 \frac{1.23 I}{P_{\text{opt}} + V_b I}$$

where I is the cell current. The maximum value of η_p is 25 percent, which is obtained at $V_b \approx 0.7$ V.

Although the peak quantum efficiency of photoelectrolysis can be increased to essentially 100 percent by applying sufficient bias voltage, an ideal anode material for achieving maximum power conversion efficiency would exhibit sufficient band bending to produce effective separation of electron-hole pairs even at zero bias voltage. Therefore, the electron affinity, as well as the

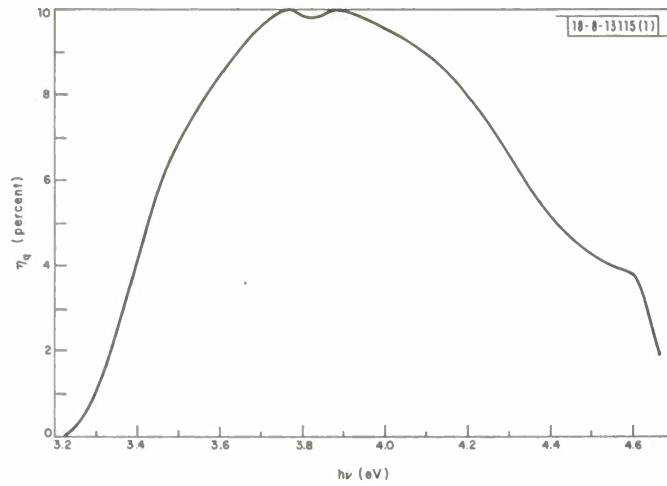


Fig. III-4. External quantum efficiency (η_q) at zero bias voltage vs photon energy ($h\nu$) for photoelectrolysis of water in cell with SrTiO_3 anode in 10N NaOH solution.

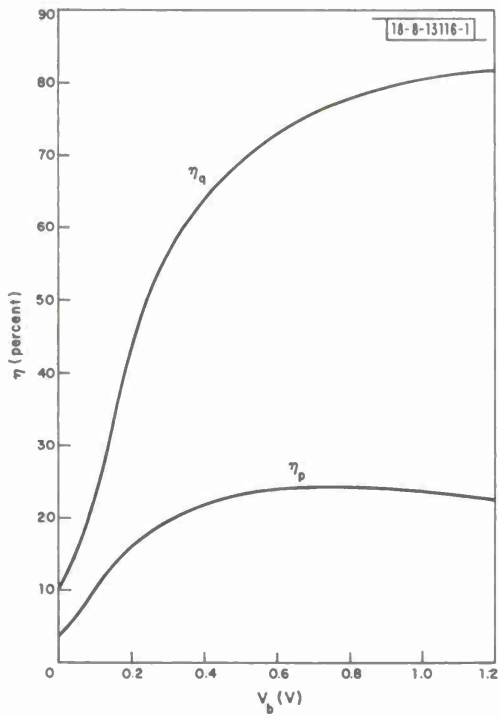


Fig. III-5. External quantum efficiency (η_q) and power conversion efficiency (η_p) vs bias voltage (V_b) for photoelectrolysis of water in cell with SrTiO_3 anode in 10N NaOH solution. Photon energy was 3.8 eV.

energy gap, should be considered in evaluating semiconductors for possible use in the conversion of solar energy by means of photoelectrolysis. The electron affinity, or more precisely the work function, is the characteristic property of a semiconductor that determines the flat-band potential when the material is immersed in an electrolyte, just as it determines the contact potential difference between the semiconductor and a metal. Thus, the difference of 0.2 eV between the values of $(\xi_F)_{fb}$ for SrTiO_3 and TiO_2 is just equal to the difference between the contact potential differences of 0.52 and 0.31 eV that we measured for these two materials with respect to Au by using the Kelvin method in air. An ideal anode material for solar energy conversion would have an electron affinity several tenths of an electron volt less than that of SrTiO_3 , as well as an energy gap about 1 eV lower.

J. G. Mavroides
J. A. Kafalas
D. F. Kolesar

C. STARK-SPLIT EXCITONIC SURFACE STATES ON MgO

With the objective of elucidating the role played by surface states in the photoelectrolysis of water in cells with TiO_2 and SrTiO_3 anodes (see Sec. III-B), we have been using reflection electron energy-loss spectroscopy (ELS) to study the surface electronic structure of these and related materials. Initial results obtained for TiO_2 and other titanium oxides were reported previously.¹⁵ As part of this investigation, ELS studies are also being made on MgO (Ref. 16), since an understanding of electron energy-loss processes in this relatively simple and well-studied oxide will aid the interpretation of loss spectra for TiO_2 and other transition-metal oxides.

By determining both the angle-of-incidence and primary-electron-energy dependence of the ELS spectra for MgO, we have been able to unambiguously separate transitions from the Mg(2p) and Mg(2s) core levels to excited states into those of bulk and surface origin. The energies of the bulk excitonic transitions are in good agreement with the optically observed excited states of the free Mg^{2+} ion.¹⁷ The surface-state transitions can be described well by a simple, one-parameter model for the Stark splitting of the bulk Mg^{2+} -like excitonic states in an electric field ξ_s at the position of a surface Mg^{2+} ion. The experimentally determined value of ξ_s is 3.0×10^8 V/cm, compared with the value of 3.7×10^8 V/cm calculated for the electric field produced by the Madelung potential gradient. This is the first quantitative identification of Stark splitting of electronic energy levels in the intense Madelung electric fields at the surface of ionic insulators.

By varying the energy and angle of incidence of the primary-electron beam, a wide range of effective depths can be sampled in ELS. The electron mean free path in a solid increases from 4 to 5 Å for energies between about 40 and 150 eV, to 20 to 30 Å for 2000-eV electrons.¹⁸ Thus, an ELS spectrum taken with a primary-electron energy $E_p \sim 2000$ eV at normal incidence will be dominated by transitions of bulk origin, whereas a normal-incidence spectrum taken with $E_p \sim 100$ eV will exhibit both bulk and surface transitions. The contribution of bulk transitions to the spectrum can be virtually eliminated by using a primary beam of ~ 100 eV at grazing incidence. We have used this approach to separate our spectra into structure of bulk and surface origin. By using a double-pass cylindrical-mirror electron spectrometer and retarding the emitted electrons to a constant energy of 50 eV, an energy-independent resolution of 0.8 eV was maintained. Modulation was applied to the gun accelerating voltage in order to eliminate

Auger peaks from the spectra. First-derivative energy-loss spectra were obtained by recording $dn(E)/dE$, where E is the electron kinetic energy in vacuum, vs energy loss E_L ; the location of peaks in $n(E)$ could be determined from these spectra to within ± 0.2 eV.

The MgO samples were (100) surfaces cleaved from a single crystal and etched in boiling H_3PO_4 (85 percent). The surfaces were then sputter-etched in an ultrahigh vacuum system with 260-eV Ar ions incident at about 70° to the surface normal. Some samples were also annealed for 5 min. at about $1200^\circ C$. Both treatments yielded very good LEED patterns and gave the same energy-loss spectra.

The experimental ELS spectra for transitions from the Mg(2p) and Mg(2s) core levels to excited states are shown in Fig. III-6(a-c). The solid curves are Mg(2p) spectra; they can be compared directly with the optically observed Mg^{2+} free-ion spectrum in Fig. III-6(d) (Ref. 17). The spectra for transitions from the Mg(2s) core level, which lies 38.4 eV below the Mg(2p) level, show similar excited-state structure; one such spectrum is shown by the dotted curve in Fig. III-6(b). The spectrum in Fig. III-6(c) is for $E_p = 2000$ eV, normal incidence, and the positions of peaks in $n(E)$ are labeled B_1 through B_8 , indicating their bulk origin. The locations of these peaks, which are given in Table III-1, are in good agreement with those for transitions

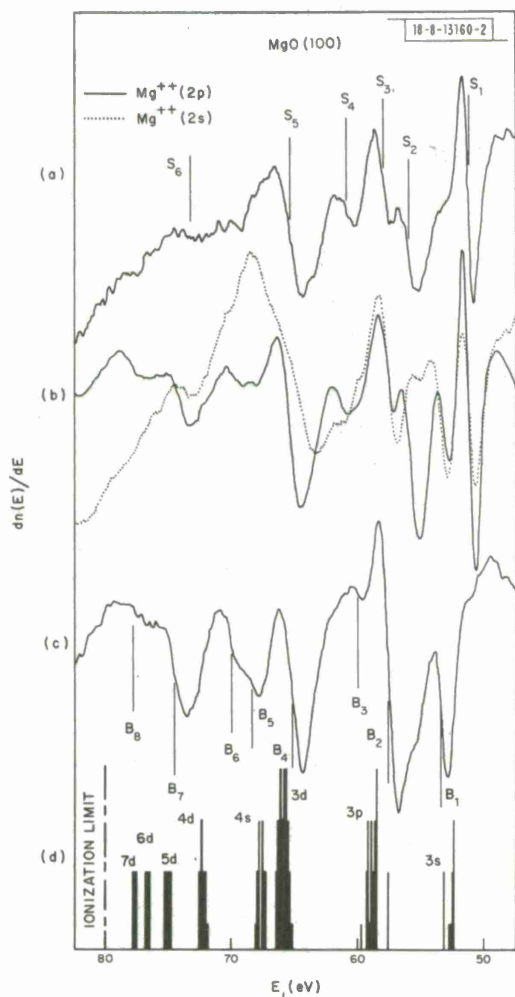


Fig. III-6. First-derivative energy-loss spectra, $dn(E)/dE$ vs energy loss E_L , for transitions from the Mg(2p) (solid lines) and Mg(2s) (dotted line) core levels in MgO(100). (a) $E_p = 120$ eV, grazing incidence; (b) $E_p = 120$ eV (solid line) and 200 eV (dotted line), normal incidence; (c) $E_p = 2000$ eV, normal incidence; (d) observed Mg^{2+} free-ion spectrum from Ref. 17. Mg(2s) spectrum has been shifted down by 38.4 eV to align it with Mg(2p) spectrum. Positions of bulk peaks B_1 through B_8 and surface peaks S_1 through S_6 are indicated in (c) and (a), respectively.

TABLE III-1
OBSERVED Mg(2p)-EXCITED STATE TRANSITIONS IN MgO

This Work (eV)		Previous Experiments (eV)		
Surface ^a	Bulk ^b	Transmission ELS ^c	X-Ray Absorption ^d	UV Reflectivity ^e
51.3	—	—	—	—
—	53.7	54	53.5	53.5
56.0	—	55.8 (vw)	—	—
58.0	57.8	57.9	57.4	57.3
—	60.1	60.5 (w)	60.5 (w)	—
60.9	—	—	—	—
65.4	65.4	65	65.0	64
—	68.6 (w)	—	68.2	—
—	70.2	69.5	70.5	—
73.2	—	—	—	—
—	74.5	74	—	—
—	77.5	—	76.5	—

a. S₁ through S₆ in Fig. III-6(a).
b. B₁ through B₆ in Fig. III-6(c).
c. From Fig. 1 of Ref. 19.
d. Ref. 20.
e. From Fig. 1 of Ref. 21.

from the Mg(2p) core level to excited states observed by high-energy transmission ELS,¹⁹ x-ray absorption spectroscopy,²⁰ and ultraviolet reflectivity,²¹ all of which are basically bulk probes. The energies of peaks B₁, B₂, B₄, and B₅ are very close to the 3s, 3p, 3d, and 4s levels, respectively, in the Mg²⁺ 2p → nℓ series in Fig. III-6(d) (Ref. 16). Additional peaks are seen up to the ionization limit of the free Mg²⁺ ion, with no further structure until the onset of the Mg(2s) spectrum at E_L ≈ 90 eV. Peak B₃, which is only present for E_p ≥ 500 eV, may be due to the excitation of both an Mg²⁺ ion and an O²⁻ ion.

As the primary-electron energy is lowered, surface-state transitions appear in the energy-loss spectrum, and at E_p = 120 eV, normal incidence [Fig. III-6(b)], the bulk and surface contributions are of comparable magnitude. The Mg(2s) spectrum in Fig. III-6(b), taken with E_p = 200 eV, normal incidence, also contains peaks arising from both bulk and surface transitions. On going to grazing incidence at E_p = 120 eV [Fig. III-6(a)], only surface-state transitions S₁ through S₆ remain in the spectrum. The locations of these surface-state peaks in n(E) are given in Table III-1. Both the bulk and surface peaks listed in the table were observed in our earlier ELS measurements on MgO (Ref. 16), but we were unable to distinguish between them either experimentally or theoretically.

The similarity between the excited-state spectrum of a free Mg^{2+} ion and the ELS spectrum of bulk transitions from the $Mg(2s)$ and $Mg(2p)$ states in MgO suggests that an ionic description is also applicable to the surface transitions. As discussed by earlier workers,²² an ion at the surface of a crystal does not experience the same Madelung potential as the same ion in the bulk. The Madelung shifts of the initial and final states of a surface ion should be essentially the same, producing no net shift in its transition energies. However, in an ionic insulator there is a large gradient of the Madelung potential at the surface, giving rise to a strong electric field that should produce a Stark mixing of ionic states. We have applied a simple model of this effect to the calculation of the Stark-split spectrum of the Mg^{2+} surface ions in MgO .

In our model, an average electric field $\vec{\epsilon}_s$ at the position of a surface Mg^{2+} ion and normal to the surface is assumed to produce a Stark interaction term $H_{\text{Stark}} = -e\vec{\epsilon}_s \cdot \vec{r}$. In evaluating the Stark effect, we consider only the contribution of the one-electron 3s, 3p, 3d, 4s, 4p, 4d, and 4f states of the excited Mg^{2+} ion. Term structure due to the interaction of the core hole and the excited electron is neglected. The Stark shifts of the 2s and 2p core holes are also neglected, since they are calculated to be less than 3 percent of the 3s Stark shift. The matrix elements of the Stark interaction for the Mg^{2+} ion are written, $\langle n'l'm_l | H_{\text{Stark}} | nlm_l \rangle = -\vec{\epsilon}' \cdot \langle n'l'm_l | \vec{r} | nlm_l \rangle$, where $\vec{\epsilon}' = e\vec{\epsilon}_s / Z_{\text{eff}}$, Z_{eff} is an effective charge seen by the electron in its excited orbit, and the $\langle n'l'm_l | \vec{r} | nlm_l \rangle$ are the matrix elements of \vec{r} for the hydrogen atom.²³ The values for the 3s, 3p, 3d, 4s, 4p, 4d, and 4f energy levels are taken from the observed bulk peaks (B_1 , B_2 , B_4 , B_5 , B_5 , B_6 , and B_7 , respectively), and each one lies roughly within the range of multiplet energies for the corresponding level of the Mg^{2+} free ion spectrum.¹⁷ The identification of the peaks beyond B_5 is not critical to the location of the surface peaks S_1 through S_5 .

The results of the Stark-effect calculation are summarized in Fig. III-7, which shows the energy levels of the Mg^{2+} excited states as a function of the parameter ϵ' expressed in atomic units (au). The levels above ~ 70 eV are not accurate because of the neglect of $n = 5$ and higher

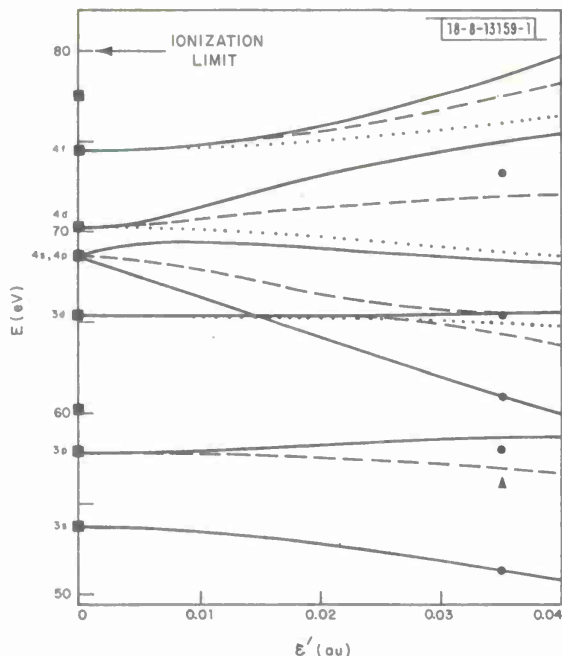


Fig. III-7. Energy of Stark-split Mg^{2+} excited states vs normalized surface electric field ϵ' (in atomic units). Full lines represent $m_l = 0$ levels, dashed lines are $m_l = \pm 1$ levels, and dotted lines are $m_l = \pm 2$ levels. The $m_l = \pm 3$ level associated with 4f is not shown. Squares are observed bulk peaks; dots and triangle are observed surface peaks. Triangular point is inferred to be an $m_l = \pm 1$ level in view of selection rule discussed in text.

states. The best overall fit to the observed surface peak energies, indicated by the dots and triangle in Fig. III-7, is obtained for $\epsilon' \cong 0.035$ au. For the Mg^{2+} free-ion spectrum, a rough fit of the energy levels for $n = 3 \rightarrow \infty$ relative to the ionization limit is given by a hydrogenic series with a screened charge of $Z_{\text{eff}} \sim 3$, as expected. For $\epsilon' = 0.035$ au, this value of Z_{eff} gives the average surface electric field seen by an excited Mg^{2+} electron as $\epsilon_s \sim 0.11$ au (3.0×10^8 V/cm). This value of ϵ_s is in satisfactory agreement with the calculated Madelung electric field at the center of a Mg^{2+} ion on the undisplaced (100) surface of MgO, $\epsilon_s = 0.136$ au (3.7×10^8 V/cm).

Additional evidence for the Stark-effect model of the surface states is provided by the very small amplitude of peak S_2 in the $2s \rightarrow nl$ surface spectrum at normal incidence [see dotted curve in Fig. III-6(b)]. Because the interaction of the Mg^{2+} surface ion with a normally incident electron beam has cylindrical symmetry, the resulting transitions should have $\Delta m_l = 0$ (assuming small angle scattering)²⁴ so that the $(2s, m_l = 0) \rightarrow (nl, m_l = \pm 1)$ transitions are forbidden. When the electron beam is tipped away from normal incidence, the symmetry selection rule breaks down. We do observe a strong increase in the relative intensity of the $(2s, m_l = 0) \rightarrow (3p, m_l = \pm 1)$ transition at grazing incidence. The $(2p, m_l = 0)$ and $(2p, m_l = \pm 1)$ states are almost degenerate; therefore, transitions from the 2p levels to final states with $m_l = 0$ or ± 1 are observed even at normal incidence.

Although the phenomenological identification of both the bulk and surface transition spectra of the Mg ion in MgO with the spectrum of the free Mg^{2+} ion is quite satisfactory, a conceptual difficulty remains. For $Z_{\text{eff}} \sim 3$, a rough hydrogenic value for the size of the Mg^{2+} , $n = 3$ orbit is $r \sim (3n^2/2Z_{\text{eff}}) a_{\text{Bohr}} \sim 2.25 \text{ \AA}$. Since the distance between the Mg^{2+} ion and the O^{2-} ion in MgO is only 2.1 \AA , there is a large overlap of the Mg^{2+} , $n = 3$ orbit with the O^{2-} charge cloud, suggesting the importance of banding. Nevertheless, as demonstrated in Ref. 16, we have found that the Mg excited states observed in MgO are in poor agreement with the conventional one-electron band picture of MgO. Additional experimental and theoretical work on the localized nature of the excitonic states in ionic crystals is necessary for a detailed understanding of this class of materials.

V. E. Henrich
G. Dresselhaus
H. J. Zeiger

D. THIN-FILM CONDUCTING MICROGRIDS AS TRANSPARENT HEAT MIRRORS

Transparent heat mirrors should have important applications in solar-energy collection and radiation insulation.²⁵ Two different types of transparent heat mirrors, both made from thin films, have been identified: a multilayer composite consisting of a metal film sandwiched between transparent dielectric layers (e.g., $\text{TiO}_2/\text{Ag}/\text{TiO}_2$, Ref. 26), and a single-layer film of a wide-bandgap semiconductor containing a high concentration of charge carriers (e.g., Sn-doped In_2O_3 , Ref. 27). In this report we describe the fabrication of a third type, a microgrid made from a conducting film by introducing openings that are large enough to transmit solar radiation but small enough for the film to retain high infrared reflectivity. Horwitz²⁸ has recently proposed the use of metal grids as selective surfaces for solar-energy collection.

To achieve efficient conversion of solar energy to thermal energy, as in a flat-plate collector, transparent heat mirrors should transmit solar radiation (with a wavelength range of $0.4 < \lambda < 2.5 \mu\text{m}$ for air mass 2) but reflect the thermal radiation from the heated absorber (with a range of $2.5 < \lambda < 100 \mu\text{m}$ for most applications). A conducting microgrid with openings about 2.5 μm

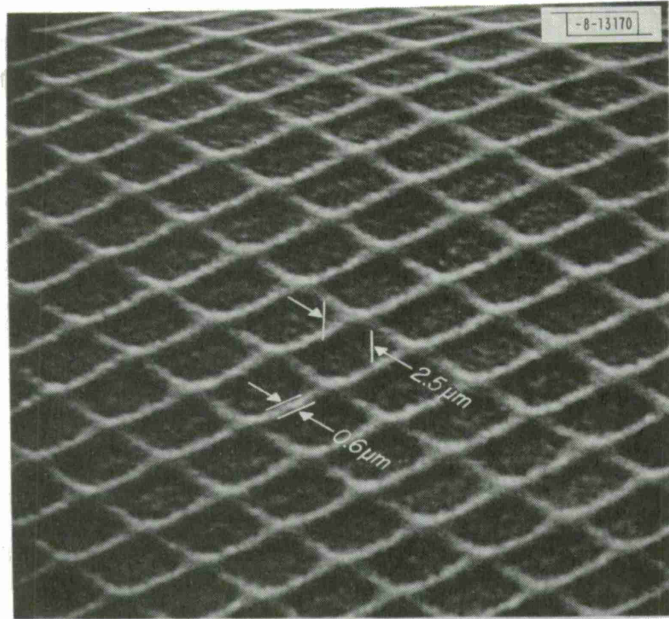


Fig. III-8. Scanning electron micrograph of microgrid fabricated from Sn-doped In_2O_3 film.

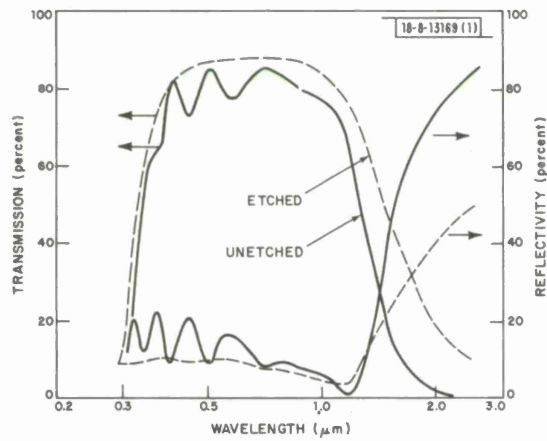


Fig. III-9. Optical transmission and reflectivity of Sn-doped In_2O_3 films on glass before etching (solid lines) and after etching to form conducting microgrid (dashed lines).

on a side can satisfy these requirements because solar radiation is transmitted through openings of this size, while the infrared reflectivity of the microgrid is much higher than the fraction of its planar area that is occupied by the conducting material forming the grid lines. An estimate of the infrared reflectivity can be obtained by using a theoretical expression for the reflectivity of a grid antenna made from two sets of perfectly conducting parallel wires of radius r that intersect at right angles to form square openings of side a and are joined at their intersections. If $a \gg r$ and the incident wavelength $\lambda \gg a$, the reflection coefficient is given by²⁹

$$\Omega = |R|e^{i\varphi} = \frac{1}{1 + \frac{\alpha k}{\cos \Theta} \left(1 - \frac{\sin^2 \Theta}{2}\right)} \quad (\text{III-2})$$

where $|R|$ = reflectivity, φ = phase angle, $\alpha = \ln(a/2\pi r)$, $k = 2\pi/\lambda$, and Θ = angle of incidence from the normal.

Application of Eq. (III-2) shows that for transparent heat mirrors there is a significant advantage in making microgrids from transparent conductors rather than opaque ones. For an opaque material, the solar transmission of a microgrid is equal to the fraction of its area that is not occupied by the grid lines: $T_s = a^2/(a+w)^2$, where w is the linewidth. For $a = 2.5 \mu\text{m}$, w must be $0.2 \mu\text{m}$ in order to achieve $T_s = 0.85$. From Eq. (III-2), taking $r = w/2$, for a perfect conductor the reflectivity at $10 \mu\text{m}$ will then be only 0.825 rather than 1. If the conductor initially has a solar transmission of 0.85, however, T_s will be increased to 0.95 for a microgrid with $w = 0.6 \mu\text{m}$, and for this linewidth Eq. (III-2) gives an infrared reflectivity of 0.99 at $10 \mu\text{m}$.

In view of the improved performance to be expected by using a transparent conductor instead of an opaque one, we have fabricated microgrids from thin films of Sn-doped In_2O_3 , the best transparent conductor now available. Films about $0.35 \mu\text{m}$ thick were deposited on Corning 7059 glass substrates by RF sputtering a commercial hot-pressed target of In_2O_3 -15 m/o SnO_2 at a forward power of 650 W. Their resistivity was about $2 \times 10^{-4} \Omega\text{-cm}$, and their initial solar transmission was about 0.8. Microgrids about $1 \times 1 \text{ cm}$ in area were produced by photolithography. A layer of photoresist (AZ 1350B) about $0.3 \mu\text{m}$ thick was first spun on the film, and the microgrid pattern was imaged onto the photoresist with a projection-alignment system using 10:1 reduction of a mask with $25\text{-}\mu\text{m}$ square holes and $6\text{-}\mu\text{m}$ lines. The photoresist was developed to open the $2.5\text{-}\mu\text{m}$ holes, and the remaining photoresist was stabilized by a 1-min. flood exposure with a collimated, high-pressure, 200-W Hg lamp followed by a postbake. The exposed Sn-doped In_2O_3 film was then etched away at the rate of approximately 700 \AA/hr with a solution prepared by diluting two parts by volume of concentrated HCl with one part by volume of distilled H_2O .

Figure III-8 is a scanning electron micrograph of a microgrid prepared by this procedure. The grid pattern is somewhat distorted because the SEM was operated with the sample tilted to minimize charging effects. Measurements made with an optical microscope at normal incidence gave the expected dimensions of about $2.5 \mu\text{m}$ for the holes and $0.6 \mu\text{m}$ for the linewidth.

Figure III-9 shows the optical transmission and reflectivity measured over the wavelength range from 0.3 to $2.5 \mu\text{m}$ for an unetched portion of an Sn-doped In_2O_3 film on glass (solid lines) and for a microgrid prepared from another portion of the same film (dashed lines). An integrating sphere coated with MgO was used for the measurements in order to avoid errors due to diffraction effects. The interference fringes observed at short wavelengths for the unetched film are not obtained for the microgrid because the grid lines are not uniform in thickness after etching.

The transmission data of Fig. III-9 have been integrated to determine the solar transmission, which is defined as

$$T_s = \frac{\int T(\lambda) A(\lambda) d\lambda}{0.91 \int A(\lambda) d\lambda}$$

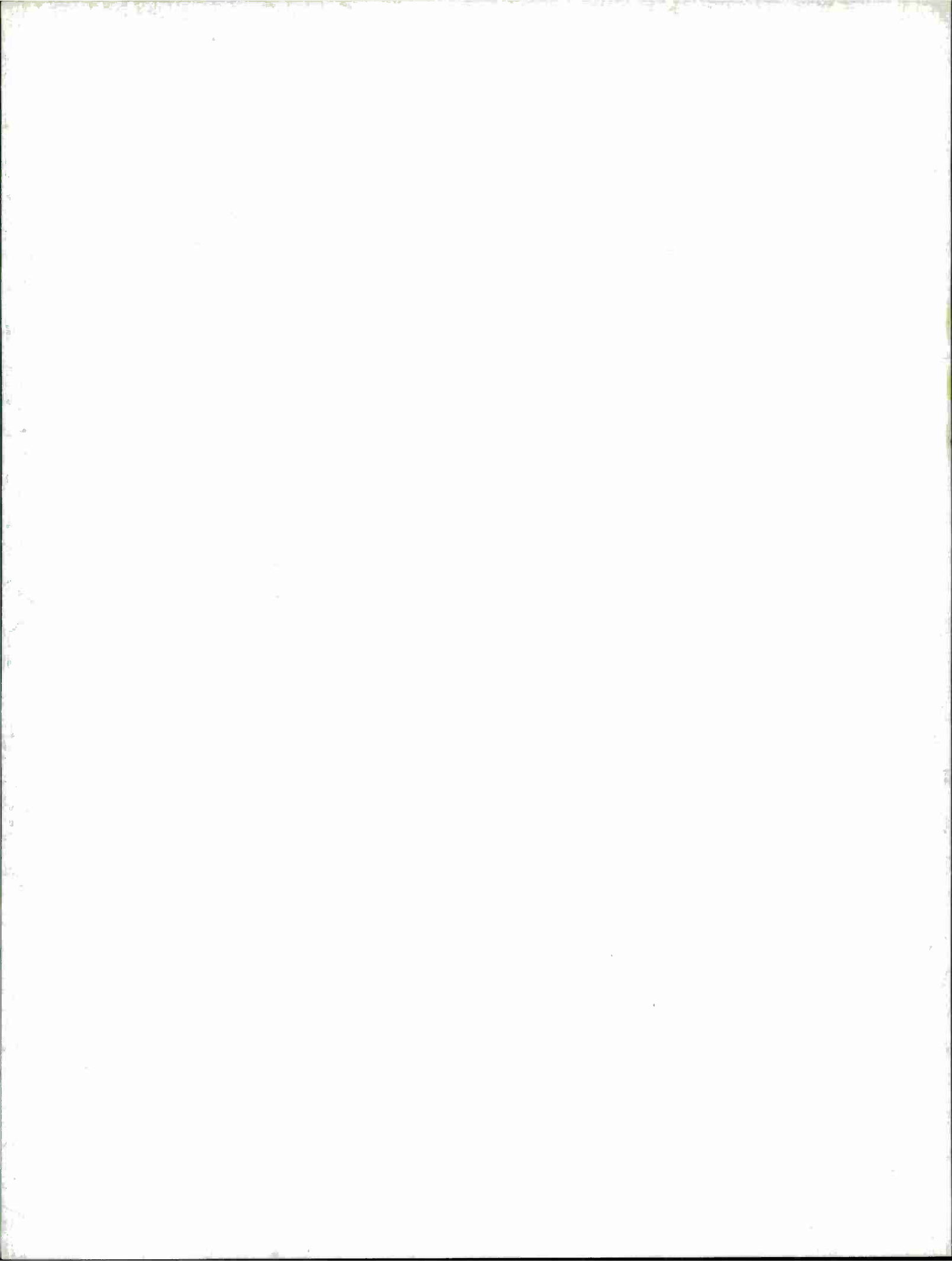
where $T(\lambda)$ = transmission of the film-glass composite, $A(\lambda)$ = intensity of solar radiation (AM2), and 0.91 is the solar transmission of the bare glass substrate. As expected, the value of T_s was increased by etching, from 0.8 for the unetched film to 0.9 for the microgrid. The spectral measurements could not be extended beyond 2.5 μm , since a spectrophotometer with an integrating sphere for longer wavelengths is not available. Therefore, a Gier-Dunkle reflectometer was used to measure the integrated reflectivity of radiation from a room-temperature blackbody, whose emission peaks at 10 μm . The measured reflectivity was reduced by etching, from 0.91 for the unetched film to 0.83 for the microgrid. This reduction is significantly larger than the decrease of 1 percent in the reflectivity at 10 μm calculated from Eq. (III-2) for a grid with the same geometry. It is not clear whether the additional decrease resulted because Sn-doped In_2O_3 does not satisfy the assumption of infinite conductivity at all frequencies made in deriving Eq. (III-2), or because in the fabrication process the grid lines became thin enough (less than 0.2 μm) to cause a decrease in reflectivity.

J. C. C. Fan
F. J. Bachner
R. A. Murphy

REFERENCES

1. L. G. Cohen, P. Kaiser, J. B. MacChesney, P. B. O'Connor, and H. M. Presby, *Appl. Phys. Lett.* **26**, 472 (1975).
2. C. J. Nuese and G. H. Olson, *Appl. Phys. Lett.* **26**, 528 (1975).
3. K. Sugiyama and H. Saito, *Japn. J. Appl. Phys.* **11**, 1057 (1972); R. E. Nahory and M. A. Pollack, *Appl. Phys. Lett.* **27**, 562 (1975).
4. A. P. Bogatov, L. M. Dolginov, L. V. Druzhinina, P. G. Eliseev, B. N. Sverdlov, and E. G. Shevchenko, *Sov. J. Quant. Electron.* **4**, 1281 (1975).
5. R. L. Moon, G. A. Antypas, and L. W. James, *J. Electron. Mater.* **3**, 635 (1974).
6. G. A. Antypas and R. L. Moon, *J. Electrochem. Soc.* **120**, 1574 (1973).
7. K. J. Bachmann and E. Buehler, *J. Electron. Mater.* **3**, 279 (1974).
8. J. J. Hsieh, *J. Cryst. Growth* **27**, 49 (1974), DDC AD-A008298/2.
9. M. G. Astles, F. G. H. Smith, and E. W. Williams, *J. Electrochem. Soc.* **120**, 1751 (1973).
10. F. G. Rosztochy, G. A. Antypas, and C. J. Casan, in *Proceedings of the Third International Symposium on GaAs and Related Compounds* (Institute of Physics, London, 1971), p. 86.
11. See review by M. B. Panish, *IEEE Trans. Microwave Theory Tech.* **MTT-23**, 20 (1975).

12. Solid State Research Report, Lincoln Laboratory, M.I.T. (1975:3), pp. 33-35, DDC AD-A019472; J. G. Mavroides, D. I. Tchernev, J. A. Kafalas, and D. F. Kolesar, Mater. Res. Bull. 10, 1023 (1975), DDC AD-A017419.
13. J. F. Dewald, "Experimental Techniques for the Study of Semiconductor Electrodes," in The Surface Chemistry of Metals and Semiconductors, H. C. Gatos, Ed. (J. Wiley and Sons, Inc., New York, 1960), p. 205.
14. F. S. Galasso, Structure, Properties, and Preparation of Perovskite-Type Compounds (Pergamon Press, London, 1969), p. 131.
15. Solid State Research Report, Lincoln Laboratory, M.I.T. (1975:1), p. 38, DDC AD-A009848/3.
16. V. E. Henrich and G. Dresselhaus, Solid State Commun. 16, 1117 (1975), DDC AD-A013951/9.
17. C. E. Moore, Atomic Energy Levels, Vol. 1, N. B. S. Circular No. 467 (U. S. Government Printing Office, Washington, 1949).
18. J. C. Tracy, Electron Emission Spectroscopy, edited by W. Dekeyser et al. (D. Reidel, Dordrecht, 1973), p. 305.
19. H. Benghaus, Opt. Commun. 2, 447 (1971).
20. V. A. Fomichev, T. M. Zimikina, and I. I. Zhukova, Soviet Phys. Solid State 10, 2421 (1969).
21. W. F. Hanson, E. T. Arakawa, and M. W. Williams, J. Appl. Phys. 43, 1661 (1972).
22. J. D. Levine and P. Mark, Phys. Rev. 44, 751 (1966).
23. E. U. Condon and G. H. Shortley, The Theory of Atomic Spectra (Cambridge University Press, Cambridge, England, 1951), p. 133.
24. N. F. Mott and H. S. W. Massey, The Theory of Atomic Collisions (Oxford University Press, Oxford, England, 1959), Chap. XI.
25. J. C. C. Fan, T. B. Reed, and J. B. Goodenough, "Heat-Mirrors for Solar Energy Collection and Radiation Insulation," in Proceedings of 9th Inter-society Energy Conversion Engineering Conference, San Francisco, 1974 (Society of Automotive Engineers, Inc., New York, 1974), p. 341.
26. J. C. C. Fan, F. J. Bachner, G. H. Foley, and P. M. Zavracky, Appl. Phys. Lett. 25, 693 (1974), DDC AD-A007892/3.
27. J. C. C. Fan and F. J. Bachner, J. Electrochem. Soc. 122, 1719 (1975).
28. C. M. Horwitz, Opt. Commun. 11, 210 (1974).
29. M. I. Kontorovich, V. Yu. Petrunin, N. A. Yesepkina, and M. I. Astrakhan, Radio Engineering and Electronic Physics 7, 222 (1962).

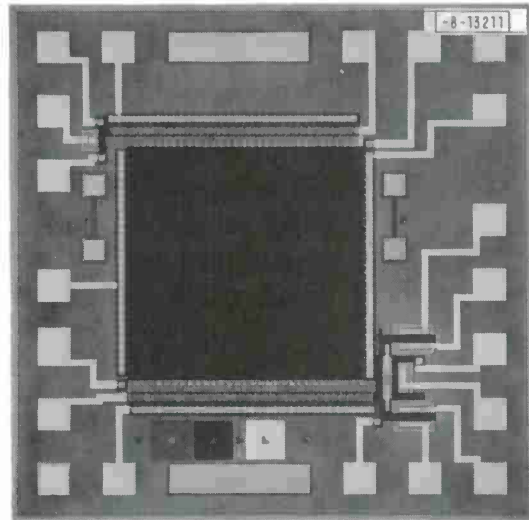


IV. MICROELECTRONICS

A. CHARGE-COUPLED IMAGING ARRAYS

A large-area, 100- × 400-element, CCD imaging array is being developed for the GEODSS (Ground Electro-Optical Deep Space Surveillance) project. The initial phase of the development program which has been reported previously¹ was a 100 × 1 linear array utilizing polysilicon gates and a buried channel. Details of the design, processing, and testing of this device have also been reported.² In addition, a prototype 30 × 30 imaging array has been fabricated and tested. Here, we describe the current state of the CCD development effort as regards the original 30 × 30 prototype and two redesigned versions of this imaging array. We will also present the current state of the design of the 100- × 400-element array.

Fig.IV-1. A 30- × 30-element, CCD imaging array showing serial input register (top) used for test purposes, and serial output register (bottom) terminating in an output diode and a MOSFET preamplifier. Device utilizes polysilicon gates and buried channel, and operates in two-phase mode.



The first prototype imaging array (Fig.IV-1) is a two-phase, implanted barrier device consisting of an array of 30 × 30 elements, each element measuring 1.2 × 1.2 mils [Ref. 2, (1975:1)]. A 32-bit serial output shift register, seen along the bottom of the array in Fig.IV-1, carries the charge packets from the array to an output diode and a MOSFET preamplifier. Adjacent to these are located a second MOSFET and a collection diode. The latter do not receive the signal charge, but do pick up various switching transients principally from the pulse which resets the potential on the collection diodes every clock period. By combining the outputs of the two MOSFETs in a differential amplifier, the reset pulse pickup can be subtracted from the signal.³

In addition to these features, a 32-bit serial register for inserting electrical input signals for test purposes has been included. The device has been tested using both electrical and optical inputs. Because the number of charge transfers is not large and because of experimental difficulties to be described, the transfer inefficiency could only be measured by optical means, and is estimated to be less than 10^{-3} per transfer (on the best arrays) at data rates of 500 kHz. The principal difficulty in evaluating the device with an electrical input appears to be the interface

between serial registers and the vertical columns of the array. In this region, it is necessary to connect the register gates to the array columns by means of a narrow channel so as to funnel charge to and from the proper gates in the serial registers. The channel width is determined by the lateral diffusion of the boron channel stop, and in the devices obtained to date this lateral diffusion has nearly pinched off the narrow channel, making the charge transfer difficult at these points. Subsequent imaging arrays have been redesigned to alleviate this problem as described below.

The device has been tested optically using a light spot which can be focused down to a size of about 1 mil. Because of high dark currents ($>500 \text{ nA/cm}^2$), all testing had to be performed with the device cooled in a Dewar. The response of the device to the light spot was satisfactory and confirmed that the transfer inefficiency was below 10^{-3} per transfer in the best cases. Difficulties in obtaining good quantitative data by this method include nonuniformity in the response of the elements to a given input light level and scattering of the light spot by dirt and scratches in the optical window on the Dewar. The Dewar is now being modified so that the windows can be readily exchanged and cleaned.

Another feature of the original 30×30 prototype which required modification on later devices is the size of the output MOSFET. At the time the device was designed, the source-drain spacing was conservatively made to be $20 \mu\text{m}$ to avoid source-drain punch-through caused by the lightly doped substrate. The dimensions of the gate were relatively large ($1.0 \times 6.4 \text{ mil}^2$), resulting in a gate capacitance of over 1 pF. This large capacitance results in relatively low output signal levels. Test MOSFETs have been fabricated with various source-drain spacings, and have been implanted simultaneously with the formation of the buried channel. These tests have shown that the implantation can eliminate the source-drain punch-through even on the shortest channel ($3\text{-}\mu\text{m}$) devices tested and still retain typical MOSFET characteristics.

As a result of the experience gained on the first 30×30 array, two redesigned versions are now being built. An initial design for the large-area, $100\text{-} \times 400$ -element array has also been developed, and the masks are currently being fabricated. These devices have output diodes and MOSFETs of reduced dimensions so as to bring the capacitance at the output diode-MOSFET gate node to less than 0.1 pF. The resulting improvement in signal level should improve the signal-to-noise ratio to the extent that signals of fewer than 100 electrons can be detected. The problem of the channel stop pinch-off at the point where the array exchanges charge with the serial registers can be alleviated by processing changes which reduce the channel stop diffusion depth. In addition, the interface between the array and the input and output registers has been redesigned to further alleviate the problem. Another new feature to be incorporated in these devices is a pair of diodes along the input and output registers to collect excess charge caused by optical overloads. The function of the diode pairs will be to control the blooming of charge from column-to-column. Details of these new structures will be described in subsequent reports.

B. E. Burke R. W. Mountain
R. A. Cohen W. H. McGonagle

B. PACKAGING FOR THE CCD SENSOR ASSEMBLY FOR THE GEODSS PROGRAM

The detector being built for use at the prime focus of a 31-inch telescope in the GEODSS Program will be a hybrid integrated circuit consisting of 16 charge-coupled-device (CCD) imaging arrays mounted on an alumina interconnect substrate. Each of the CCD imagers will be a $100\text{-} \times 400$ -element array with chip dimensions of 0.135×0.516 inch. The proposed hybridized

array is shown in Fig. IV-2. The technical requirements for this hybrid present some very challenging packaging problems. A strict requirement in fabricating the hybrid circuit is that a vertical row of elements on any one chip must align with the same row in all the chips above and below it within 0.0005 inch (0.5 mil). Also, the center lines of all the chips must be parallel to within 0.03°. The method used to attach the CCD chips to the hybrid substrate must be secure, stable, and withstand moderate cooling (approximately -60°C). This method must also provide for the possible removal of a chip and replacing it with a new chip in precisely the original position. Interconnections on the alumina substrate must provide power, ground, clocking, and output. In addition a discrete, low-noise, bipolar transistor and two resistor chips are integrated on the hybrid to buffer the output signal from each chip. The interconnections near one end of a CCD array are shown in Fig. IV-3, and illustrate the location of the discrete components.

The hybrid integrated circuit will require a stable, mechanically rigid substrate material. An alumina, multilayer interconnect board satisfies this requirement. Metalized lines in buried layers will provide for interconnections. The plane on which the CCD chips will be mounted will be precision ground to provide flatness within a fraction of a mil to meet "z" direction (depth of focus) tolerances.

The alignment of the chips as mentioned above is critical. Smaller chips for other hybrid circuits have been precisely aligned under a microscope by using alignment marks applied to the chip with the accuracy of photolithography. However, the depth of focus and field-of-view limitations of high-power microscopes preclude application of this method to these large chips. Thus, after reviewing a number of possibilities, we chose to obtain the high chip registration precision needed by adapting an x-y coordinator which is designed for the inspection of machined parts. This equipment can be accurately positioned to better than 0.2 mil in x and y and has a digital readout. A special vacuum chuck collet to hold the chips during placement has been designed and will be fitted to the coordinator stylus. The CCD chips will be prepared for this process by precisely sawing them from the wafer to within 0.1 mil. Thus we will be assured of square, accurately dimensioned device edges for placement. The x-y coordinator will permit us to accurately place and log the position of each device to facilitate proper replacement, should this become necessary. We are tooling this equipment and working out procedures to assure accurate device registration.

Registration again limits the options available for die attachment. A consideration of the requirements indicates that some form of adhesive is required, rather than eutectic or solder bonding. Present test indications are that an anerobic, fast-setting adhesive most nearly meets these requirements.

The interconnection and dimensional requirements of our substrates have been discussed with several ceramic multilayer vendors who are capable of supplying us with the special substrates. Purchase specifications are being prepared which will include an electrical schematic and an interconnection routing layout generated by the computerized graphics design system. The CCD devices will have aluminum metalization, so we will ultrasonically bond with aluminum wire to assure metallurgical compatibility.

An x-y stage with digital readout to 0.1-mil accuracy will be fitted to our profile projector to characterize the registration of the devices on the substrate for its telescope environment.

T. F. Clough B. E. Burke
L. L. Grant P. A. Beatrice

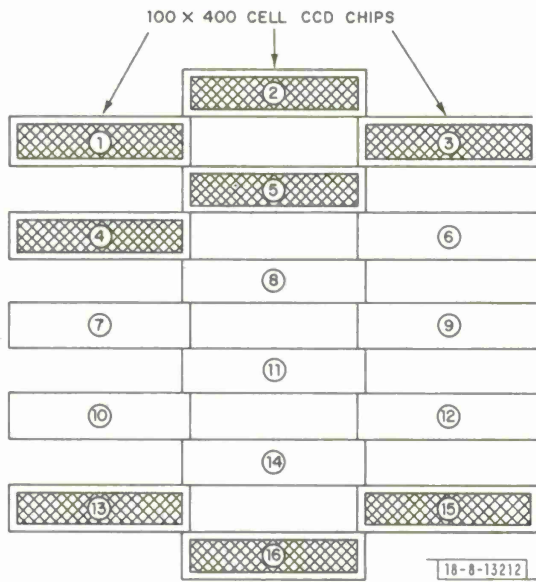


Fig. IV-2. Schematic of 16-chip hybrid detector for use with 31-inch telescope in GEODSS Program. Each chip is 100- x 400-element, CCD imaging array whose dimensions are 0.135 x 0.516 inch.

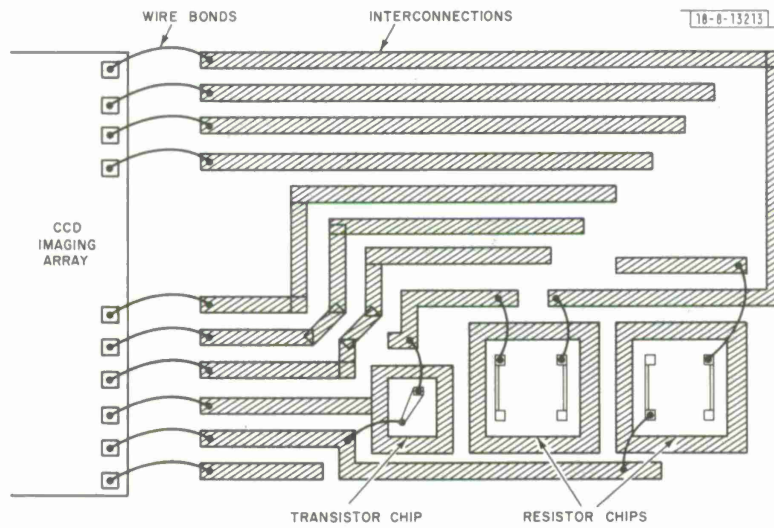


Fig. IV-3. Schematic of some interconnections on alumina substrate used to mount and interconnect 16, CCD imaging arrays. Shown is right-hand edge of one imaging array, top level interconnects on alumina substrate, bipolar transistor, and two resistor chips used to buffer output signal from imaging array, and required wire bonds.

C. PIN DIODE ATTENUATOR

The UHF receiver for the proposed LES-10 satellite requires a set of identical, electronically variable attenuators as part of the pattern-forming network for the phased array antenna. A discrete-component version of the attenuator was constructed and was found to have insufficient attenuation in the desired frequency range because of the inductance of the PIN diodes. It was therefore decided to minimize this inductance by taking advantage of the short lead lengths made possible by a chip-and-wire hybrid microcircuit. The hybrid version did indeed provide the expected improvements in maximum attenuation at ultrahigh frequencies. A summary of the results of preliminary electrical measurements on the first hybrid sample is given in Table IV-1. The following paragraphs discuss the design philosophy and fabrication details.

TABLE IV-1 VARIABLE ATTENUATOR PERFORMANCE PRELIMINARY RESULTS	
Attenuation (dB)	
Minimum	< 1
Maximum	> 25
VSWR	< 1.25
Frequency range (MHz)	30 to 400
Discrete version	18-dB maximum attenuation at 400 MHz

A simplified circuit diagram of the attenuator is shown in Fig. IV-4, where D1 and D2 are PIN diodes which function as current-controlled variable resistors. It is the parasitic reactance in series with D2 which limits the maximum attenuation in the discrete-component version, and

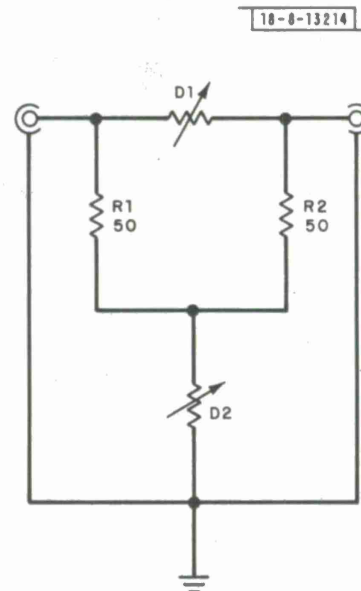
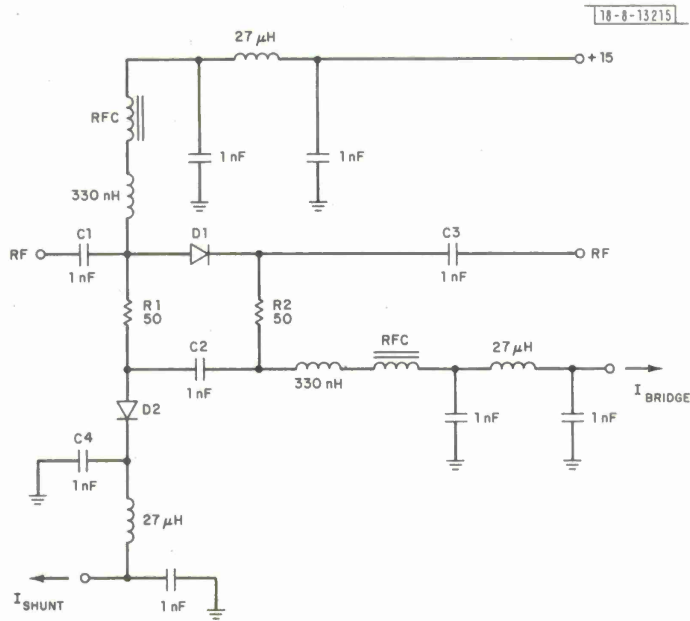
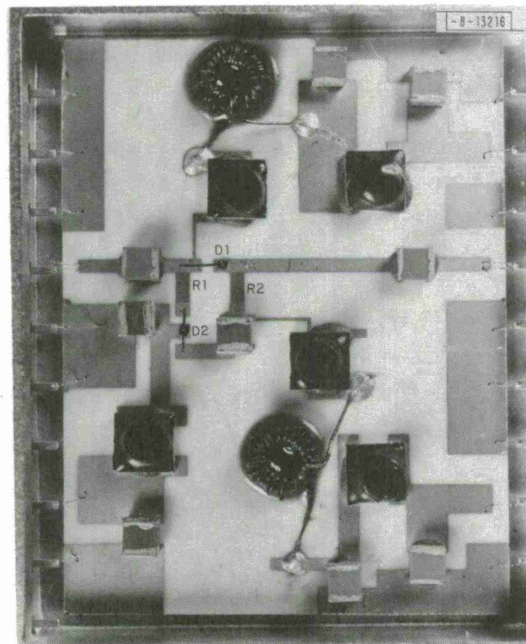


Fig. IV-4. Simplified circuit schematic of bridged-T attenuator showing two PIN diodes D1 and D2, and two Ta₂N resistors R1 and R2.



(a)



(b)

Fig. IV-5. (a) Complete schematic of current-controlled attenuator showing components included in hybrid for biasing and for providing 40 dB of isolation down to 10 MHz. (b) Photograph of completed hybrid with components arranged as in schematic. PIN diodes (D1 and D2) and Ta₂N resistors (R1 and R2) which are basic components of attenuator are labeled.

to a lesser extent in the hybrid circuit. This particular bridged-T attenuator circuit was chosen over other types, such as the pi attenuator, because the low VSWR required to minimize phase shift can be obtained with simple analog control circuitry.

In addition to the resistive components shown in Fig. IV-4, many reactive components are necessary for biasing and achieving electromagnetic compatibility with other components in the satellite. The satellite has such a high level of RF energy over a wide band of frequencies in such a small space that it is necessary to provide a minimum of 80 dB of isolation from 10 to 400 MHz on all bias lines in order to prevent one component from interfering with another. These additional components are shown in Fig. IV-5(a) where C1 through C4 and the 330-nH inductors are necessary for biasing, and the other inductors and capacitors provide 40 dB of isolation down to 10 MHz. The remaining 40 dB of isolation will be provided by external components.

The circuit in Fig. IV-5(a) was fabricated on a 0.75- × 1.0- × 0.025-inch alumina substrate by conventional Ta₂N - Ti/Pd/Au thin-film hybrid techniques using a Ta₂N sheet resistance of 25 ± 1 ohm per square. A photograph of a finished attenuator prior to cover attachment is shown in Fig. IV-5(b) where the arrangement of components is identical to the arrangement of components in the schematic of Fig. IV-5(a). The diodes are bonded with 0.005-inch-wide by 0.001-inch-thick gold ribbons, and the inductance in series with D2 is minimized by using the three-terminal connection technique shown in Fig. IV-5(b). The back side of the substrate is metalized with a gold ground plane which is connected to the ground conductors on the top of the substrate by shorting around the edge.

Although electrical evaluation of these units is not yet complete, preliminary results as shown in Table IV-1 indicate that this circuit meets the requirements of the intended application, and may be useful for other purposes such as automatic gain control in the frequency range from 30 to 400 MHz. This design could also be adapted to higher-frequency applications by using quarter-wave microstrip transmission-line sections for some of the reactive elements.

D. L. Smythe †
D. M. Hodsdon †

D. COMPUTERIZED GRAPHIC DESIGN

The mask-making facility of the Microelectronics Group provides hard-surface, emulsion, and film photomasks to many users within Lincoln Laboratory. Critical to this operation is the software used in conjunction with the IBM 370/168 time-sharing system and the Calma interactive graphic design system to provide input to a D. W. Mann Model 1600 pattern generator. This software is continuously being improved and new software is generated as needed to update our mask-making capabilities. Recent developments and the status of some of the more important computer programs are described below.

The recently acquired Calma system produces an output tape which will control the pattern generator which, in turn, exposes a pattern made up of small rectangles onto a high-resolution photographic plate. The information on the tape includes the x and y coordinates of the center of each rectangle to be exposed, the height and width of the rectangle, and the angle (A) between the w and x axes (angle of rotation of the rectangle), as shown in Fig. IV-6.

† Group 63 (RF Techniques).

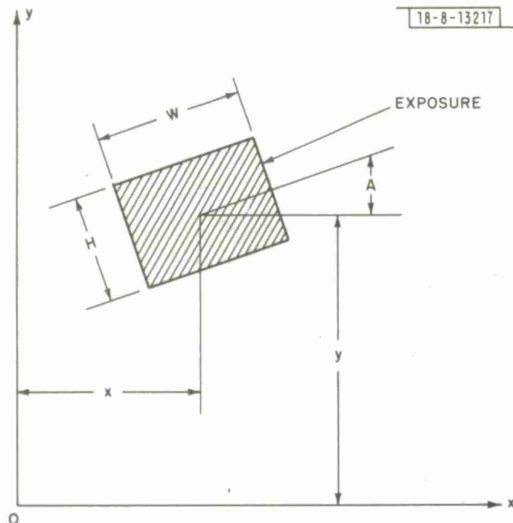


Fig. IV-6. Input data required for each rectangle to be exposed by pattern generator — x and y coordinates of center, width W , height H , and angle of rotation A .

In order to make efficient use of the pattern generator, the data must be sorted by arranging the rectangles into an order which reduces the pattern-generator running time. The Calma software does not do this. Therefore, a program was written to run on the IBM 370/168 which will take the data from the Calma system and sort the rectangles by finding the next rectangle whose coordinates can be reached in the minimum time considering the pattern generator's position. The program (called CALMASRT) writes the sorted data on tape ready to be used as input for the pattern generator. A mask requiring 18,645 exposures took 47 hours to run with data directly from the Calma system. After sorting the data with CALMASRT, the same mask with the same number of exposures was generated in 7 hr. An additional feature of this program is to add a simple "m" to the number of the file to be sorted, and the mirror image of the pattern will be created, sorted, and put on tape.

There are several other programs available on the Laboratory's IBM 370/168 time-sharing system which are designed to generate masks for integrated-circuit and thin-film work. MANNPLOT is a user-oriented program that produces the file or files needed to generate a mask on the pattern generator. The program is straightforward to use, the commands are concise and self-explanatory, numeric data are specified in a simple format with or without decimal points, and each piece of data is separated by commas.

The user is required to break his pattern up into a series of rectangles and enter the coordinates of each rectangle. Circles and annuluses may be entered by a simple "CIRCLE" or "ANNULUS" command. The circle command requires the x and y centers and diameter, and the annulus requires x and y centers and inner and outer diameters. The data files may be entered or corrected within the program, and the user may display his file on any one of the four display scopes supported: ARDS, TEKTRONIX, PDP, or TSP.

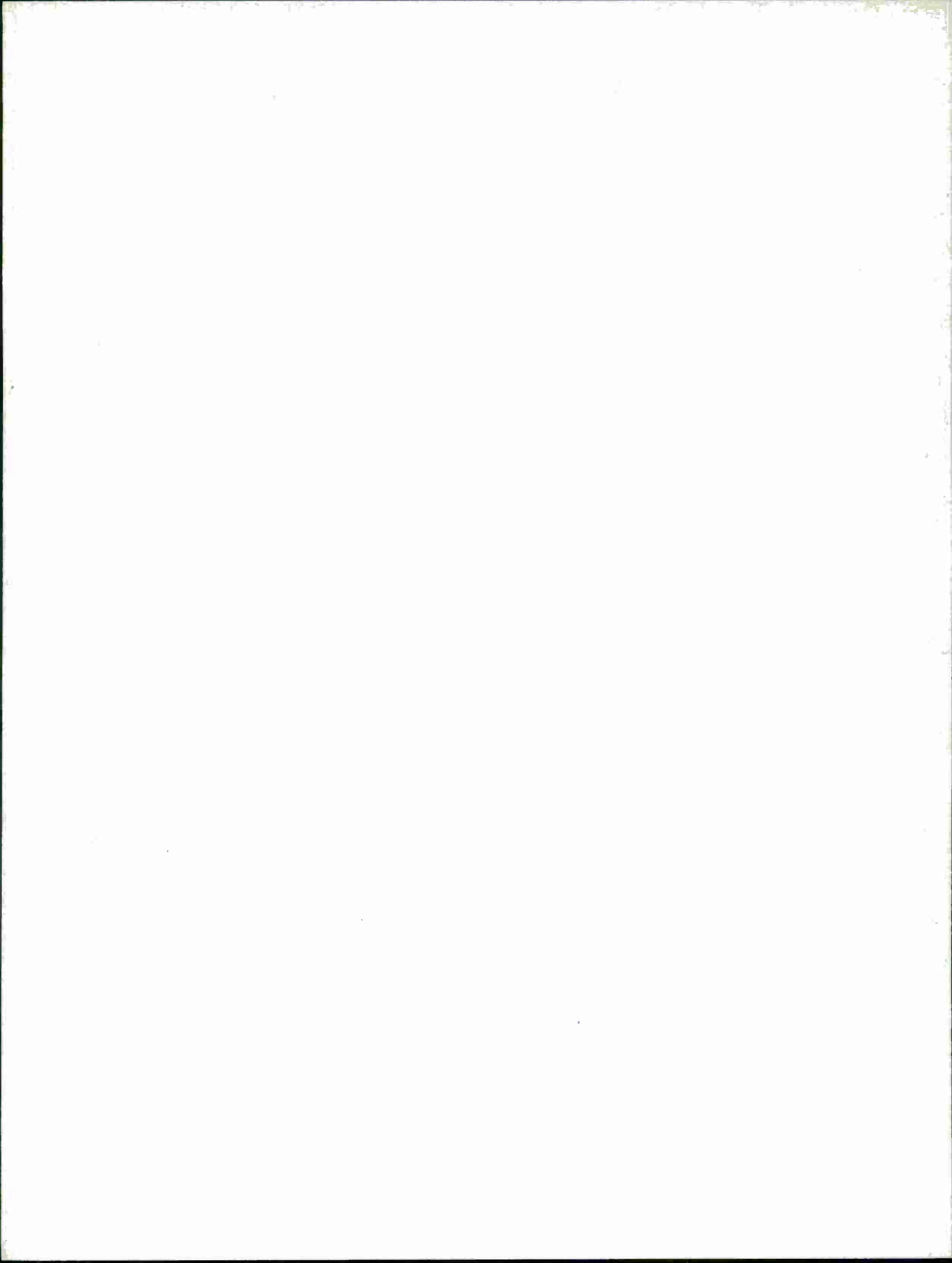
As in CALMASRT, the MANNPLOT program produces a sorted file ready to be used on the pattern generator. Sometimes it is useful to utilize this sorted file as input to MANNPLOT for display and processing. For this purpose, a program called DESORT has recently been written which converts these sorted files back to MANNPLOT files. The program writes the MANNPLOT file on the user's disk, displays the file on a scope if being used, and produces hard copy if needed.

Other programs available are "T3000," "FUDGE," and "1795." Some of the patterns required by customers within the Laboratory are beyond the capabilities of the Model 1600 pattern generator, and require the services of an outside vendor who has a newer, more powerful Model 3000 machine. However, the 3000 has a different input format from the 1600 pattern generator and, in order to supply the vendor with the correct input to his model 3000, the program "T3000" was written which converts the data file prepared by MANNPLOT to the format required by the 3000. "FUDGE" is a program that will generate a second MANNPLOT file by changing the height and width of each rectangle in the original file by adding or subtracting a specified increment. The program "1795" produces a punched paper tape which is used to control the Model 1795 photo-repeater. The tape information includes the location, stepping distance, and number of cells in each row as well as information about "drop-ins" and "drop-outs" which allows for the insertion of test cells and alignment marks.

G. L. Durant

REFERENCES

1. Solid State Research Report, Lincoln Laboratory, M.I.T. (1974:4), pp. 55-57, DDC AD-A004763/9.
2. Solid State Research Reports, Lincoln Laboratory, M.I.T. (1975:1), pp. 56-57, DDC AD-A009848/3; (1975:2), pp. 45-47, DDC AD-A013103/7; and (1975:3), p. 43, DDC AD-A019472.
3. C. K. Kim, "Two-Phase Charge Coupled Linear Imaging Devices with Self-Aligned Implanted Barrier," International Electron Device Meeting, Washington, D.C., December 1974.



V. SURFACE-WAVE TECHNOLOGY

A. REFLECTION COEFFICIENT OF A GROOVE FOR RIGHT-ANGLE REFLECTION ON Y-CUT LiNbO₃

In both reflective-array compressors¹ and filter banks,² a surface-acoustic-wave (SAW) beam is reflected from groove edges in groove arrays. The reflection is through 90° from the Z-direction to the X-direction on Y-cut LiNbO₃. A knowledge of the reflection coefficient for this geometry is important for understanding and designing these devices.

We assume that the model used for normal-incidence³ reflection applies also to the right-angle reflection. The reflection coefficient of an up-step Γ_u , the reflection coefficient of a down-step Γ_d , and the transmission coefficient τ (same for up- or down-step) are then given by

$$\Gamma_u = r - j \frac{\hat{B}}{2} \quad (V-1)$$

$$\Gamma_d = -r - j \frac{\hat{B}}{2} \quad (V-2)$$

$$\tau = 1 - \frac{r^2}{2} - j \frac{\hat{B}}{2} \quad (V-3)$$

The parameter r is the impedance mismatch contribution which is proportional to step height h ,

$$r = C \frac{h}{\lambda} \quad (V-4)$$

and \hat{B} is the stored-energy contribution which is proportional to h^2 ,

$$\frac{\hat{B}}{2} = C' \left(\frac{h}{\lambda}\right)^2 \quad (V-5)$$

where λ is the wavelength of the surface wave, and C and C' are proportionality coefficients to be determined by our experiments. The reflection coefficient Γ_g of a groove, which is a down-step followed by an up-step, is simply a combination⁴ of Γ_d , Γ_u , and τ :

$$|\Gamma_g| = 2r \sin \theta + \hat{B} \cos \theta \quad (V-6)$$

where $\theta = (kw + \hat{B})/2$, w is the width of the groove in the Z-direction, and $k = 2\pi/\lambda$. Since for shallow grooves $\hat{B} \ll kw$, r can be measured using arrays with $w = \lambda/2$ while \hat{B} can be measured using arrays with $w = \lambda$.

We have fabricated 10-groove arrays of both types in the configuration shown in Fig. V-1. The arrays had ion-etched groove depths between 0.06 and 0.5 μm . The results of our measurements of the impedance-mismatch part r and of the stored-energy part $\hat{B}/2$ are shown in Figs. V-2 and V-3, respectively. Thus, we find that $C = 0.51 \pm 0.3$ and $C' = 4.5 \pm 0.4$. A previous measurement⁵ of C yielded a value between 0.44 and 0.46.

For shallow grooves, which are usually used in reflection-grating SAW devices, r contributes the main part of the amplitude of the reflection while \hat{B} produces a phase shift. In fact, $\hat{B}/2$ is directly the phase shift on transmission past each groove edge. A detailed knowledge of

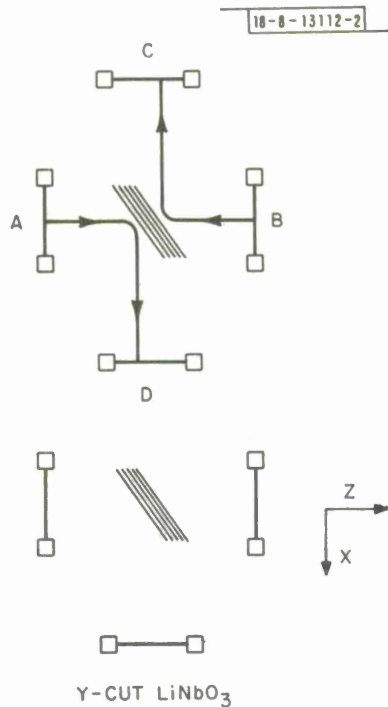


Fig.V-1. Layout of transducers and 10-groove gratings. When redundant reflection measurements A to D and B to C are combined with transmission measurements A to B and C to D, then reflection coefficient of grating can be deduced independent of transducer response.

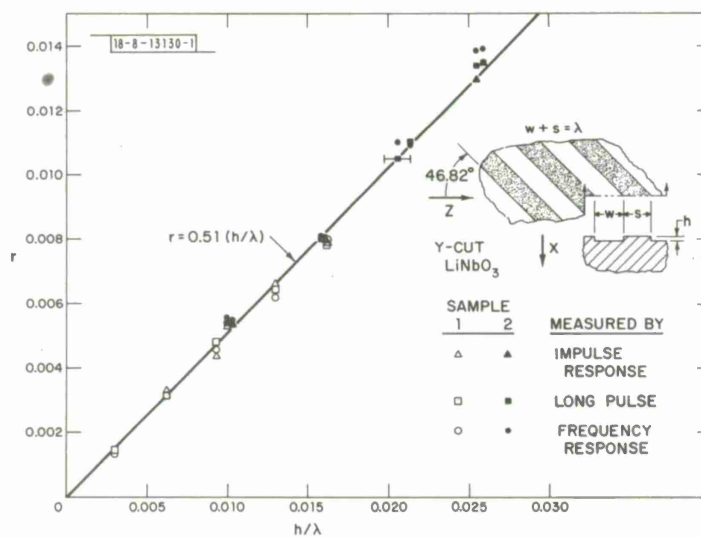


Fig.V-2. Impedance mismatch part r of reflection coefficient of step for 90° reflection from Z to X on Y -cut LiNbO_3 plotted vs normalized groove depth. Inset shows portion of grating (top view and cross section). Wavelength of $20 \mu\text{m}$ is equal to period of grating in Z -direction. Width of grooves is equal to half of wavelength. Slope of straight line drawn through points is 0.51.

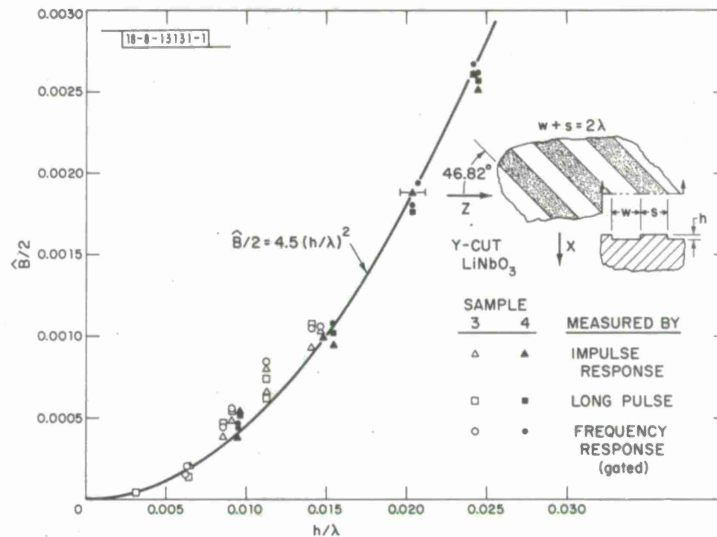


Fig. V-3. Energy storage part $\hat{B}/2$ of reflection coefficient for 90° reflection from Z to X on Y-cut LiNbO₃ plotted vs normalized groove depth. Inset shows portion of grating. Period of groove grating is two wavelengths in propagation direction. Width of grooves is equal to a wavelength, so that impedance-mismatch contributions from opposite edges of groove cancel. A parabola is fitted through points.

these reflection coefficients is particularly important in understanding and designing devices which require a careful control of phase such as the burst matched filter (see Sec. B below).

J. Melngailis
R. C. M. Li

B. BURST MATCHED FILTER

The burst matched filter is a SAW device which compresses a Doppler-sensitive radar burst waveform consisting of 16 coherent linear-FM subpulses.⁶ This device is an outgrowth of the prior development of large-time-bandwidth-product pulse compressors which use the reflective-array-compressor (RAC) configuration.^{1,7} Figure V-4 shows a schematic of the burst matched filter. It has an input and an output transducer and 16 pairs of gratings in a chevron pattern. Each section consists of an array of grooves with graded periodicity. The 16 gratings have identical groove placements and are spaced to give exactly 5 μsec of path difference between reflections from neighboring gratings. When a waveform of 16 linear-FM subpulses spaced at 5 μsec is input to the burst matched filter, each grating section will reflect a part of the signal and compress it. These compressed pulses will also add in phase if their spacing is exactly the 5-μsec path difference between the gratings. The exact spacing is altered if the waveform is reflected from a moving target. Thus, a bank of burst matched filters each with a slightly different spacing between grating sections would provide simultaneous range and Doppler discrimination.

In order to demonstrate the burst-matched-filter concept, a prototype device has been built on Y-Z LiNbO₃. The filter is designed to process a burst waveform consisting of 16 subpulses each 3 μsec long with a 60-MHz bandwidth centered at 200 MHz. Each section of the burst matched filter is Hamming weighted over the 60-MHz bandwidth for time (range)-sidelobe suppression. In addition, the overall envelope of the response of the 16 sections is also Hamming

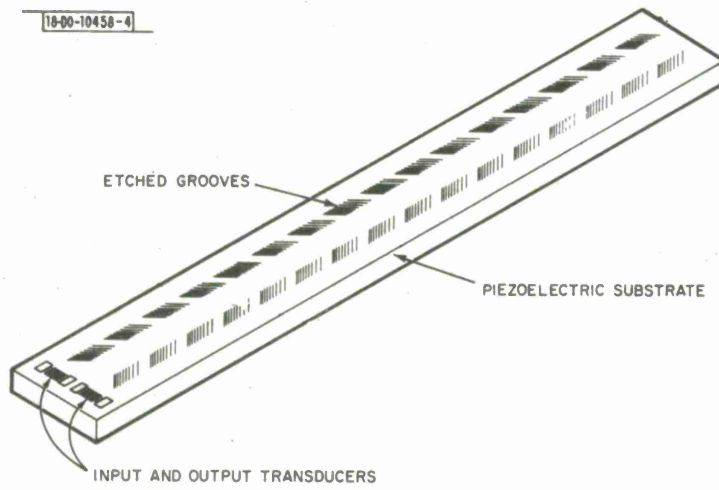


Fig. V-4. Burst matched filter consisting of 16 RACs.

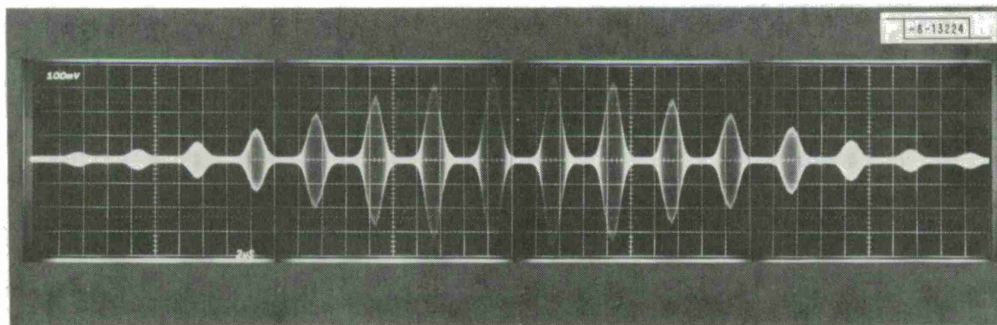


Fig. V-5. Impulse response of weighted burst matched filter. Horizontal scale is $2 \mu\text{sec}/\text{div}$. Overall length of response is $80 \mu\text{sec}$.

weighted for velocity (Doppler) sidelobe suppression. The impulse response of the burst matched filter is shown in Fig. V-5. Each subpulse is a linear-FM chirp. The weightings seen in the figure are produced by ion-beam etching the grooves in the reflective arrays so that their depth depends on position. The amplitude is within 0.5 dB of the desired value in all except the first three subpulses in which the response is about 1.5 dB too low. The delay between successive subpulses in the impulse response is the same to within ± 1.4 nsec. The small variation in delay is produced by stored energy effects at groove edges⁴ and will be corrected by the use of metal overlay films.^{7,8}

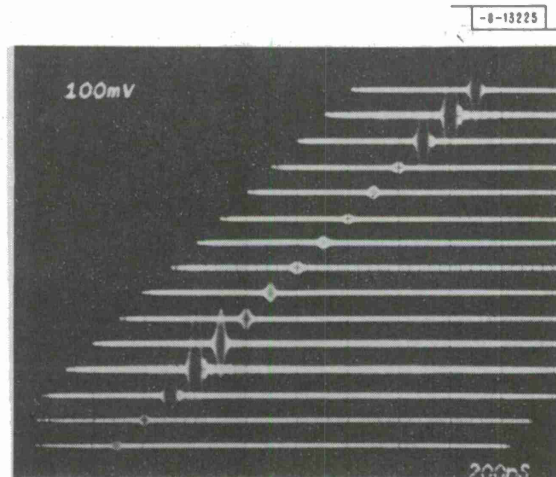


Fig. V-6. Ambiguity diagram of burst matched filter. Horizontal scale is $0.2 \mu\text{sec}/\text{div.}$ and corresponds to range. Doppler shifts at 20-kHz intervals are displayed in successive traces.

In order to test the burst matched filter, a burst-waveform signal generator was also developed. For this purpose, a subpulse expansion line in the RAC configuration was fabricated. A burst waveform consisting of 16 coherent linear chirps was produced by coherently impulsing the pulse expander 16 times at precise 5- μsec intervals. When this waveform is input to the burst matched filter, 31 compressed pulses are produced. If the filter is matched to the waveform, then the 16th compressed pulse is a maximum because all the individual compressed pulses add in phase. Doppler shifts can be simulated by changing the frequency of a master oscillator to change the subpulse spacing in the waveform. Figure V-6 shows the result of such frequency variation. The successive traces show the 16th pulse at 20-kHz intervals. The traces are displaced horizontally and vertically for clarity. If the RF burst before mixing with the local oscillator is centered at, say, 3 GHz, then the 20-kHz Doppler shift corresponds to a target approach velocity of 1000 m/sec. In each trace, the horizontal time scale corresponds to target range. The time sidelobes for the coherent burst are 30 dB down. The Doppler sidelobes are only 20 dB down due to the above-mentioned small variation in delay intervals. These initial results on this 60-MHz bandwidth burst processor show the feasibility of using surface-wave reflective-array devices for Doppler radar signal processing.

J. Melngailis
R. C. Williamson

C. BISMUTH GERMANIUM OXIDE REFLECTIVE-ARRAY COMPRESSOR WITH 125 μ sec OF DISPERSION

A compact pulse-expansion and compression subsystem was developed for MASR (Multiple Antenna Surveillance Radar), an airborne MTI surveillance radar. Sensitivity requirements dictated that the transmitted waveform be relatively long (125 μ sec). Because of its low surface-wave velocity, bismuth germanium oxide (BGO) is an attractive substrate material on which to fabricate a device for processing a waveform of this duration. Low velocity combined with foreshortening advantages of the folded reflective-array-compressor (RAC) configuration¹ yield devices which easily fit on commercially available 15-cm substrates. The use of BGO as a substrate material for RAC devices is new. It is generally considered a difficult material to use, and success in this development required that difficulties associated with material nonuniformity, metal adhesion, bonding, and ion-beam etching be solved.

System requirements set the bandwidth at 2.5 MHz. This bandwidth centered at an IF of 60 MHz yields a relatively small fractional bandwidth which, combined with large dispersion, imposes especially tight specifications on pattern accuracy, alignment, and temperature control. In addition, there exists a fundamental limit on the degree to which a RAC device can be phase compensated.^{7,8} This limitation is more severe in small-time-bandwidth devices.⁹

The devices described herein use reflection gratings whose periodicity varies quite slowly as a function of position. Because of this, a small change in reflector characteristics, such as that caused by temperature change or angular rotation, causes the effective center of reflection at any given frequency to shift by a large amount. For this reason, angular alignment and temperature must be carefully controlled.⁹

The RAC devices schematically illustrated in Fig. V-7 were fabricated on 001-110 cut BGO substrates. The basic operation of this device has been described previously.^{1,8} In order to

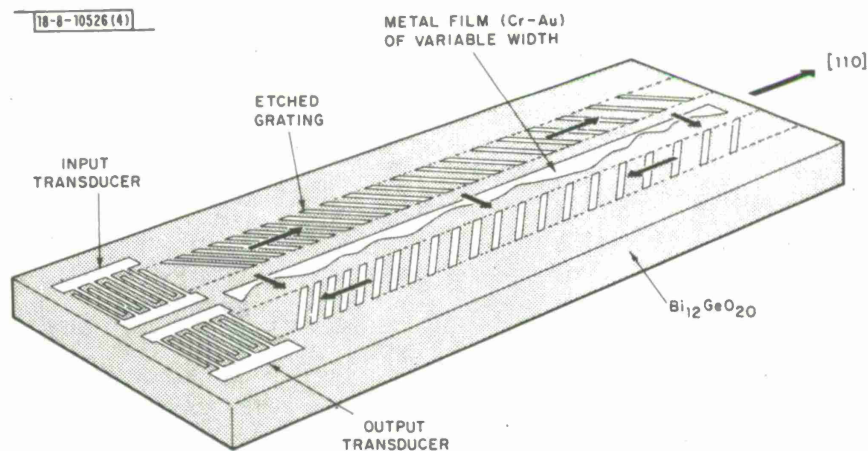


Fig. V-7. Schematic diagram of RAC operating at 60 MHz with 2.5-MHz bandwidth. Device consists of two 12-finger-pair transducers and a pair of gratings each having approximately 4500 lines. Metal film between ion-beam-etched gratings provides phase compensation by selectively slowing surface wave.

adequately stabilize the response of the RAC devices, provisions were made to thermostat the devices at 60°C, and design parameters appropriate to this temperature were employed. Measured temperature dependence of the devices indicated a value of the temperature coefficient of delay γ equal to $138 \times 10^{-6}/^{\circ}\text{C}$, which compares well with previous data.

Grooves were ion-beam etched to depths of approximately 0.1 μm or 0.35 percent of a wavelength at the center frequency for an overall reflection loss of -18 dB at center frequency. Depth weighting was employed to yield a flat amplitude response for the expansion lines and Hamming-weighted amplitude response for the compression lines.

Following the initial fabrication, the phase response of each device was tested and a phase compensation was generated and metalized in the region between the grating (Fig. V-7).⁷⁻⁹

Before internal phase compensation was added, the measured phase deviation from ideal quadratic response showed a cubic error component believed to be related to material nonuniformities. Phase distortion contributed by the transducer response is known to be negligible. In addition to this cubic component, each dispersive delay line contained a more rapidly varying periodic component reproducible from one device to the next which suggests a systematic pattern error of unknown origin. Qualitatively, the response described is characteristic of both the pulse expander and compressor devices. Separate phase-compensation patterns were required for each device since significant quantitative variations existed between the individual units.

The metal overlay pattern was also used to align the dispersion slope of all devices to the same value.⁹ Following phase compensation, a slot was cut between the transducers to provide feedthrough isolation. The finished device is mounted in a sealed package.

The CW frequency responses of the pulse expander and compressor are shown in Figs. V-8(a) and (b), respectively. In these devices, direct electromagnetic feedthrough was reduced to a level more than 100 dB below the input signals.⁹ Total midband CW insertion loss is typically 33 dB, with a 1-dB variation among devices. The Hamming-weighted compression lines exhibit a maximum deviation from an ideal Hamming function of approximately 0.5 dB.

The pulse expansion and compression lines were tested in a pulse-compression circuit. An impulse applied to the expansion line generated an expanded pulse which was gated over the center 125- μsec interval, with no limiting, before the signal was applied to the compression lines.

Typical pulse-compression performance is shown in Fig. V-9(a-b). The shape of the compressed pulse is that expected for a 2.5-MHz bandwidth device which is Hamming amplitude weighted.

The shoulder on the main lobe shown in Fig. V-9(b) is approximately -33 dB below the peak compressed pulse level. The remaining sidelobes at -35 dB and below are consistent with the measured phase and amplitude errors in the devices.

These devices indicate that BGO is a practical material for RAC devices, and is particularly useful when large dispersion is required. With proper care, problems of alignment, material nonuniformity, metal adhesion, and temperature sensitivity can be solved to yield high-performance devices.

V. S. Dolat
R. C. Williamson

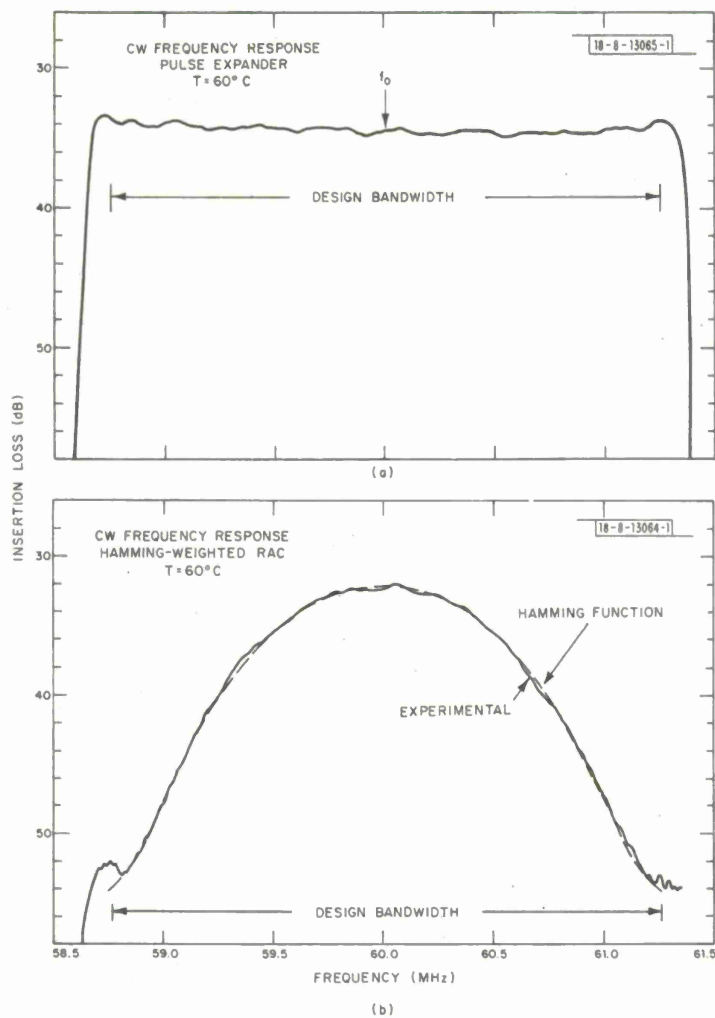
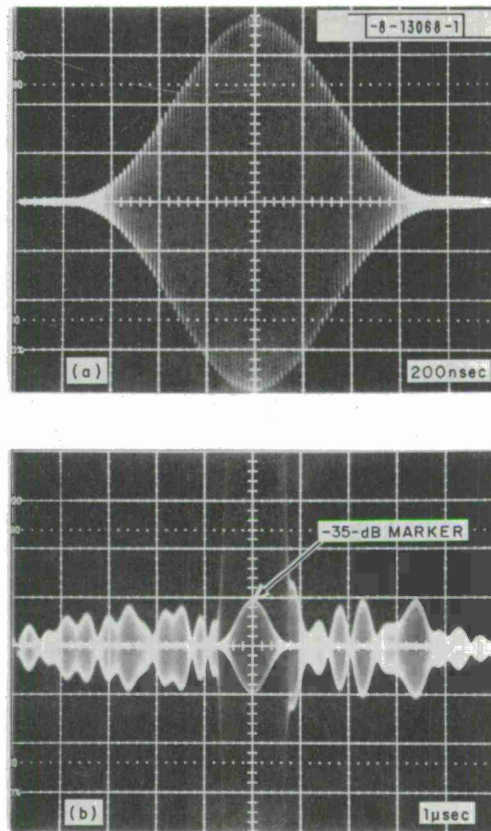


Fig. V-8. Frequency responses of (a) pulse expander, and (b) pulse compressor.

Fig. V-9. (a) Main lobe of compressed pulse. (b) Double exposure of compressed pulse showing sidelobe structure with 35-dB difference in attenuation between exposures.



D. STABLE CW OPERATION OF GAP-COUPLED $\text{Si-ON-Al}_2\text{O}_3$ TO LiNbO_3 ACOUSTOELECTRIC AMPLIFIERS

There exists a need within real-time signal-processing systems for long, wideband, non-dispersive delay lines of wide dynamic range. The ideal solution for SAW lines is to preserve signal strength by providing noise-free amplification continuously and uniformly throughout the delay period, in which case the dynamic range achievable is that of a lossless line. We report significant technological advances which have been made to improve such acoustoelectric amplifiers to the point of reproducible CW operation, thereby bringing closer to system realization very long, wideband, nondispersive delay lines of wide dynamic range.

A photograph of an assembled device is shown in Fig. V-10. Standard microelectronic techniques were used to fabricate four amplifier segments on each sapphire disk. The drift field is established through n^+ contact bars which have Cr/Au-metalized end pads to contact the Au-plated spring-loaded probes incorporated into the rectangular Plexiglas crystal-holder. Assembly is done in a filtered laminar-flow air bench, with the silicon-on-sapphire (SOS) wafer receiving a brief buffered-HF etch and water rinse prior to final packaging.

The desired gap-height is established by means of ion-beam-etched LiNbO_3 posts approximately $4\text{-}\mu\text{m}$ square in a pseudo-random array with average row spacing of about $200\ \mu\text{m}$. The novel feature of this package is the use of the SOS wafer as a pressurized diaphragm to establish uniform gaps of the order of $0.1\ \mu\text{m}$ over the $0.1 \times 2.0\text{-cm}$ interaction region. The delay line rests on a molded silicone gel which enables the top LiNbO_3 surface to become parallel to the

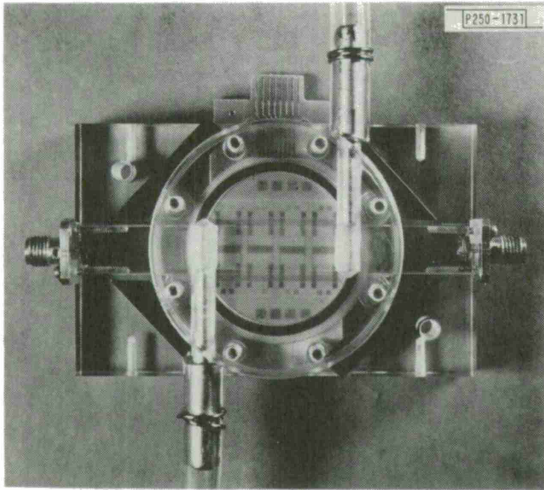
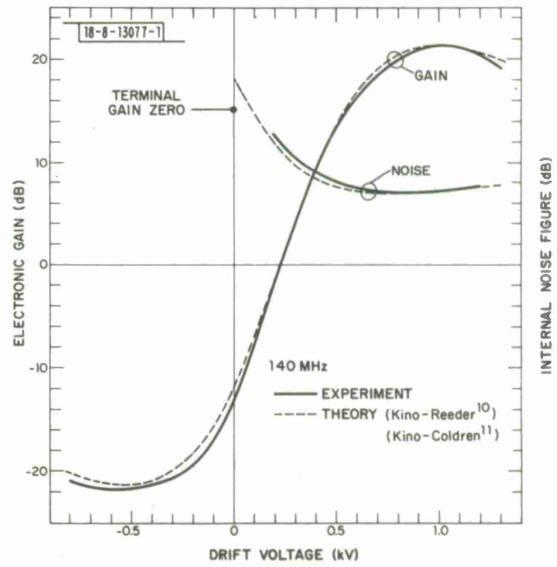


Fig. V-10. Assembled SOS/LiNbO₃ amplifier. SOS wafer is 1.5-in. diameter, 0.013-in. thick, with 1- μ m Si film patterned to form four 5-mm-long segments.

Fig. V-11. Internal gain and internal noise figure vs voltage for 5-mm-long amplifier segment. Theoretical performance is calculated for parameters: coupling gap of 0.17 μ m, mobility of 800 cm²/V sec, sheet resistance of 4×10^5 ohms/square, and 10 percent of electrons trapped.



Si film as pressure (≤ 10 psi) is applied. Both the SOS and (Y-Z) LiNbO_3 are commercially available.

A viable acoustoelectric amplifier must not only operate with DC drift field, but it must also maintain an essentially homogeneous sheet of electrons, for only then will optimum performance be realized. The achievement of maximum gain requires that the product of sheet density and drift velocity be constant; hence, in an inhomogeneous amplifier the conditions for peak gain cannot be simultaneously achieved throughout the device. All Si devices tested previously by others evidenced severe degradation at high fields due to the depletion of electrons near the anode by intense transverse fringing fields. Our new results indicate that SOS material can shield the electrons from such fringing fields. A high density (10^{18} cm^{-3}) of slow traps exists throughout the heteroepitaxial layer due to crystalline imperfection.¹⁰ In addition, many slow surface traps are formed when the Si is stripped of oxide just prior to packaging, thereby pinning the Fermi level at about one-third of the forbidden gap above the valence band and creating a depleted surface. The bulk and surface traps serve to terminate DC and low-frequency transverse electric fields and maintain amplifier homogeneity.

The experimental internal gain characteristic at 140 MHz as a function of drift voltage for a single 0.5-cm-long segment is indicated in Fig. V-11 which also shows the measured noise characteristics. Peak gain of over 21 dB is achieved at 1.05 kV. This gain exceeds the conversion loss of the transducers, and thus terminal gain is realized with a single section. The gain curve is observed to match, even at high voltage and near the gain maximum, the characteristic calculated (without adjustable parameters) from the full theoretical expressions.¹¹ Uniformity of single-segment characteristics is excellent both intra- and inter-wafer. The spread among four segments on a typical wafer was ± 0.01 dB/V in gain slope at synchronism, and ± 1.2 dB in maximum gain.

The noise behavior shown in Fig. V-11 is the first reported for DC operation, and is seen to closely match theory which attributes noise generation to fast traps.¹² A minimum noise figure of 7 dB is obtained in the region of maximum gain near 0.8 kV. In an idealized device with no fast traps, a noise figure of only 2.5 dB would be obtained at 0.8 kV. Thus, the major trade-off involved in utilizing deep traps to achieve stable DC operation is the inevitable presence of some fast traps and the consequent generation of additional, but tolerable, noise.

The dispersion of a gap-coupled structure must be minimized for a practical device. The phase characteristic of the amplifier is essentially linear, with the major deviation over the 130- to 160-MHz band contributed by the transducers. The delay line alone has less than 6° rms deviation. A worst-case condition for phase distortion occurs when all four amplifier segments are operating at synchronism. Under these conditions, the combined effect of the four amplifier segments (a 2-cm total interaction length) adds less than 0.7° rms phase error.

The dynamic range over which the amplifier transfer function is essentially linear was determined by means of a two-tone test. Complete results for a 4-segment unit operating at 1.3 times synchronism with 30-dB electronic gain are indicated in Fig. V-12. The acoustic sheet power at which 1-dB gain compression occurs is 12 dB/mm at the output. With output sheet power below 2 dBm/mm, the distortion products are more than 50 dB below the signal. An approximate efficiency of about 1 percent for a practical amplifier segment can be estimated for operation with 20-dB gain, 7-dB noise figure, and distortion products 50 dB down.

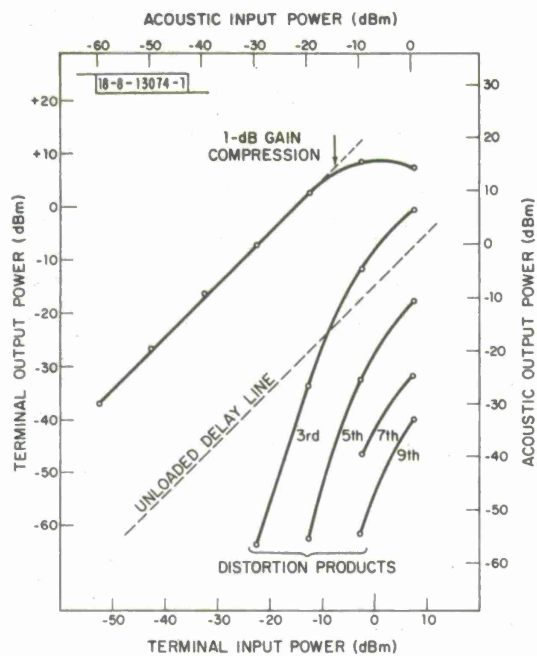


Fig. V-12. Gain-saturation and distortion-product-generation characteristics for amplifier with 30-dB total electronic gain.

Initially homogeneous amplifiers exposed to atmosphere for several weeks were observed to increase in resistance and exhibit gain characteristics indicative of carrier inhomogeneity.¹³ Degradation occurs because the Si surface slowly forms an oxide which serves to annihilate many of the surface states needed to provide shielding. Long-term alteration of the amplifiers might be prevented by sealing them in a hermetic package. This procedure is being tested. Other approaches would be to permanently pin the Si surface by creating a high density of surface states with ion implantation, or to deposit an oxidation barrier such as Si_3N_4 over the Si film.

R. W. Ralston

REFERENCES

1. R. C. Williamson and H. I. Smith, IEEE Trans. Microwave Theory Tech., MTT-21, 195 (1973), DDC AD-772211/9.
2. V. S. Dolat and J. Melngailis, "16-Channel Surface-Acoustic-Wave Filter Bank," in 1974 Ultrasonics Symposium Proceedings (IEEE, New York, 1974), pp. 756-759, DDC AD-A011323/3.
3. R. C. M. Li and J. Melngailis, IEEE Trans. Sonics Ultrason. SU-22, 189 (1975).
4. J. Melngailis and R. C. M. Li, "Measurement of Impedance Mismatch and Stored Energy in Right-Angle Reflection of Rayleigh Waves from Grooves in Y-Cut LiNbO₃," in 1975 Ultrasonics Symposium Proceedings (IEEE, New York, 1975) (in press).
5. P. C. Meyer and M. B. Schulz, "Reflective Surface Acoustic Wave Delay Line Material Parameters," in 1973 Ultrasonics Symposium Proceedings (IEEE, New York, 1973), pp. 500-502.
6. R. C. Williamson, V. S. Dolat, and J. Melngailis, "Reflective-Array Matched Filter for a 16-Pulse Radar Burst," in 1975 Ultrasonics Symposium Proceedings (IEEE, New York, 1975) (in press).
7. R. C. Williamson, V. S. Dolat, and H. I. Smith, "L-Band Reflective Array Compressor with a Compression Ratio of 5120," in 1973 Ultrasonics Symposium Proceedings (IEEE, New York, 1973), pp. 490-493.
8. R. C. Williamson, "Large-Time-Bandwidth-Product Devices Achieved Through the Use of Surface-Acoustic-Wave Reflection Gratings," in Proceedings of International Specialists Seminar on Component Performance and System Applications of Surface Acoustic Wave Devices (IEE, London, 1973), pp. 181-190.
9. V. S. Dolat and R. C. Williamson, "BGO Reflective-Array Compressor (RAC) with 125 μ s of Dispersion," in 1975 Ultrasonics Symposium Proceedings (IEEE, New York, 1975) (in press).
10. D. J. Dumin, Solid-State Electron. 13, 415 (1970).
11. G. S. Kino and T. M. Reeder, IEEE Trans. Electron Devices ED-18, 909 (1971).
12. G. S. Kino and L. A. Coldren, Appl. Phys. Lett. 22, 50 (1973).
13. B. E. Burke and A. Bers, Appl. Phys. Lett. 21, 449 (1972), DDC AD-753309.

REPORT DOCUMENTATION PAGE		READ INSTRUCTIONS BEFORE COMPLETING FORM
1. REPORT NUMBER ESD-TR-75-313	2. GOVT ACCESSION NO.	3. RECIPIENT'S CATALOG NUMBER
4. TITLE (and Subtitle) Solid State Research		5. TYPE OF REPORT & PERIOD COVERED Quarterly Technical Summary 1 August - 31 October 1975
		6. PERFORMING ORG. REPORT NUMBER
7. AUTHOR(s) Alan L. McWhorter		8. CONTRACT OR GRANT NUMBER(s) F19628-76-C-0002
9. PERFORMING ORGANIZATION NAME AND ADDRESS Lincoln Laboratory, M.I.T. P.O. Box 73 Lexington, MA 02173		10. PROGRAM ELEMENT, PROJECT, TASK AREA & WORK UNIT NUMBERS Project No. 649L
11. CONTROLLING OFFICE NAME AND ADDRESS Air Force Systems Command, USAF Andrews AFB Washington, DC 20331		12. REPORT DATE 15 November 1975
		13. NUMBER OF PAGES 82
14. MONITORING AGENCY NAME & ADDRESS (if different from Controlling Office) Electronic Systems Division Hanscom AFB Bedford, MA 01731		15. SECURITY CLASS. (of this report) Unclassified
		15a. DECLASSIFICATION DOWNGRADING SCHEDULE
16. DISTRIBUTION STATEMENT (of this Report) Approved for public release; distribution unlimited.		
17. DISTRIBUTION STATEMENT (of the abstract entered in Block 20, if different from Report)		
18. SUPPLEMENTARY NOTES None		
19. KEY WORDS (Continue on reverse side if necessary and identify by block number)		
solid state devices	surface-wave technology	imaging arrays
quantum electronics	photodiode devices	infrared imaging
materials research	lasers	surface-wave transducers
microelectronics	laser spectroscopy	
20. ABSTRACT (Continue on reverse side if necessary and identify by block number)		
<p>This report covers in detail the solid state research work of the Solid State Division at Lincoln Laboratory for the period 1 August through 31 October 1975. The topics covered are Solid State Device Research, Quantum Electronics, Materials Research, Microelectronics, and Surface-Wave Technology. Funding is primarily provided by the Air Force, with additional support provided by the Army (BMDATC), ARPA (MSO, IPTO), NSF, and ERDA.</p>		



The first part of the document discusses the importance of maintaining accurate records of all transactions. It emphasizes that every entry, no matter how small, should be recorded to ensure the integrity of the financial data. This includes not only sales and purchases but also expenses and income. The text suggests that a systematic approach to record-keeping is essential for identifying trends and making informed decisions.

In the second section, the author addresses the common challenge of reconciling accounts. It explains that discrepancies often arise due to timing differences or errors in recording. The recommended solution is to perform regular reconciliations, comparing the company's records with bank statements and other external sources. This process helps to identify and correct errors promptly, ensuring that the books are balanced and accurate.

The third part of the document focuses on budgeting and financial forecasting. It highlights the need to set realistic goals and allocate resources effectively. By creating a detailed budget, businesses can track their performance against targets and adjust their strategies as needed. The text also discusses the importance of monitoring key financial indicators, such as profit margins and cash flow, to maintain a healthy financial position.

Finally, the document concludes with a section on tax compliance. It stresses the importance of staying up-to-date with the latest tax regulations and filing returns on time. The author provides practical advice on how to organize financial records to facilitate the tax filing process and minimize the risk of penalties. It also mentions the benefits of consulting with a professional tax advisor to ensure full compliance and optimize tax outcomes.